



UNIVERSITÀ DEGLI STUDI DI TRIESTE

XXVI CICLO DEL DOTTORATO DI RICERCA IN
ENVIRONMENTAL AND INDUSTRIAL FLUID MECHANICS

Numerical Study of Turbulent Rayleigh-Bénard
Convection with Cubic Confinement

Settore scientifico-disciplinare: ICAR/01

PH.D. STUDENT: Najmeh FOROOZANI
PH.D. PROGRAM DIRECTOR: Prof. Vincenzo ARMENIO
THESIS SUPERVISORS: Prof. Joseph J. NIEMELA (ICTP)
Prof. Katepalli R. SREENIVASAN (NYU)
Prof. Vincenzo ARMENIO (UNITS)

Academic Year 2013–2014

PhD candidate: **NAJMEH FOROOZANI**

- Dipartimento di Ingneria e Architettura, Università di Trieste
Piazzale Europa 1, 34127 Trieste, Italy
najmeh.foroozani@phd.units.it
- International Centre for Theoretical Physics, ICTP
Strada Costiera, 11, 34151 Trieste ,Italy
nforooza@ictp.it

The defense date: 28th April 2015, University of Trieste

Signature from head of Ph.D. committee:
Professor Bernard Geurts

Abstract

Turbulent Rayleigh-Bénard convection (RBC) occurs when a shallow layer of fluid is heated from below. It is a challenging subject in non-linear physics, with many important applications in natural and engineering systems. Because of the complexity of the governing equations, analytical progress in understanding convection has been slow, and laboratory experiments and numerical simulations have assumed increased importance. In regard to numerical work, Large-Eddy Simulation (LES) techniques have proved to be reliable and powerful tool to understand the physics since it provides better coverage for measurements, that are not as easily obtained in physical experiments or the other numerical approaches. This thesis addresses different aspects of Rayleigh-Bénard convection in fully developed turbulent regime through Large Eddy Simulation (LES) to shed light on some important aspect of the geometrical shape of the convection cell. The layout of the thesis is as follows:

In **Chapter 1**, we first introduce Rayleigh-Bénard convection and the equations and parameters that govern it. This is followed by a discussion on different types of boundary conditions used in numerical and theoretical studies of RBC. Subsequently we present various convection states that are observed analytically and experimentally in RBC as a function of rayleigh number (Ra) and aspect ratio (Γ). To this end we present a brief survey of the analytical, experimental and numerical works on confined thermal convection. We introduce different regimes and related scaling according to Grossmann & Lohse theory. We also present the experimental and numerical results related to the Large Scale Circulation (LSC) within different geometrical shape.

In **Chapter 2**, we present the details of the numerical methods used to solve the governing non-linear equations . In the second part, we provide the details of the solver and the algorithm used to solve the RBC dynamical equations in a Cartesian geometry together with boundary conditions.

In **Chapter 3**, we demonstrate that our numerical method and solver give results consistent with the earlier numerical results. Results from the Direct Numerical Simulations (DNS) and Large Eddy Simulations (LES) with constant and dynamic subgrid-scale Prandtl number (Pr_{sgs}) are presented and compared. We observe closer agreement with Lagrangian dynamic approaches compare to references.

In the first part of **Chapter 4**, we analyse the local fluctuations of turbulent Rayleigh-Bénard convection in a cubic confinement with aspect ratio unity for a Prandtl number $Pr = 0.7$ and Rayleigh numbers (Ra) up to 10^9 by means of LES methodology on the coarse grids. Our results reveal that the scaling of the root-mean-square density and velocity fluctuations measured in the cell center are in excellent agreement with the unexpected scaling measured in the laboratory experiments of Daya and Ecke (2001) in

their square cross-section cell. Moreover we find that the *time-averaged* spatial distributions of density fluctuations show a fixed inhomogeneity that maintains its own structure when the flow switches from one diagonal to the other. The largest level of *rms* density fluctuations corresponds to the diagonal opposite that of the LSC where we observed strong counter-rotating vortex structures. In the second part we extended our simulations and Ra up to 10^{11} , in order to identify the time periods in which the orientation of LSC is constant. Surprisingly we find that the wind switches stochastically from one diagonal to the other.

In **Chapter 5**, we study the effect of 3D-roughness on scaling of $Nu(Ra)$ and consequently on the fluctuations of density. Moreover we present the effect of roughness shape when the tip has a wide angle and the other one is smooth. We study two types of elements, one of which is a pyramid and the other is a sinusoidal function spread over the bottom (heated) and top (cooled) plates, in a cubic confinement. However preliminary results suggest that the effect of roughness appears evident at high Ra numbers when the thermal boundary layer is thin enough to shape around the obstacles.

Acknowledgements

This is a great opportunity to express my gratitude to all those people who have given me the possibility to complete this dissertation in Italy.

First and most, I would like to thank to my PhD advisers, Professor Joseph J. Niemela, Professor Katepalli R. Sreenivasan and Professor Vincenzo Armenio for supporting me during these past four years in Italy. Professor Niemela is someone you will instantly love and never forget once you meet him. He is one of the most kind and one of the smartest people I ever know. I hope that I could be as lively, enthusiastic, and energetic as Joe and to someday be able to command an audience as well as he can. I deeply owe my gratitude to him. I am also very grateful to Professor Sreenivasan for his scientific advice and knowledge and many insightful discussions and suggestions. He is one of the most precise person I have ever meet and I learned many things from him. In a world I can say, he is a person who cares about his students a lot. Professor Armenio has been supportive and has given me the freedom to pursue various projects without objection. He always encouraged me to not only grow as a scientist but also as an independent thinker. His patience and support all along helped me to overcome many hard situations in work and finish this dissertation.

Indeed, Completing this work would have been all the more difficult were it not for the support by "International Centre for Theoretical Physics (ICTP)" and "United Nations Educational, Scientific and Cultural Organization (UNESCO)" from the day I came to Italy. I would like to acknowledge all the staff members of the ICTP for their kind co-operation's, support, and ever willingness to help me with my research. I learned from them to be a merciful and cooperative person. Apart from that this work would not have been possible without the computational facilities, the "ARGO CLUSTER" at ICTP. I would specially like to thank the staffs of HPC facility for their computational time and support in successfully running the code unconditionally. My special thanks are due to Dr. C. Onime and Dr. I. Girotto for allocating me some available resources at ARGO for a while when I was in a critical situation of the deadlines, and also Dr. A. Mellit for his helpful scientific mathematics discussion.

I would like to acknowledge all my colleagues and friends of Fluid Mechanics departments at University of Trieste, specially thanks Dr. F. Roman and Dr. A. Petronio.

I would like to thank all the leading experts working in this field with whom I have interacted at various scientific meets. My sincere thanks to Prof. B. Ecke, Prof. A. Domaradzki, Dr. M. Kaczorowski. I would like to acknowledge Prof. B. Geurts for his stimulating discussions and for enlightening me on the various numerical challenges in

the field of turbulence and Rayleigh-Bénard convection.

Above everything, this PhD would have not been possible without the constant support, encouragement, blessing and good wishes of my family. I will never be able to repay their unconditional support and the personal sacrifices that they have made, specially angel of my life, my mother who grown me to be an independent. And my brother, Ali, who is my best friend.

Contents

| | |
|--|-------------|
| Acknowledgements | iv |
| Contents | vi |
| List of Figures | viii |
| List of Tables | xi |
| | |
| 1 Introduction | 1 |
| 1.1 Introductory concepts | 2 |
| 1.2 Theoretical background of Rayleigh-Bénard convection | 3 |
| 1.3 Equations of motions | 4 |
| 1.3.1 The Boussinesq approximation | 4 |
| 1.3.2 Dimensionless numbers | 7 |
| 1.4 Scaling theories of turbulent transport | 10 |
| 1.4.1 Theories for $\text{Nu}(\text{Ra}, \text{Pr})$ and $\text{Re}(\text{Ra}, \text{Pr})$ | 10 |
| 1.4.2 Temperature fluctuations | 12 |
| 1.4.3 Velocity fluctuations | 13 |
| 1.5 Large Scale Circulation and its associated dynamics in confined convection cells | 14 |
| | |
| 2 Large Eddy Simulation of Rayleigh-Bénard Convection: Numerical Details | 18 |
| 2.1 Numerical methods | 19 |
| 2.2 Large Eddy Simulation techniques | 22 |
| 2.2.1 Smagorinsky subgrid-scale model | 23 |
| 2.2.2 Lagrangian Dynamic Smagorinsky model | 25 |
| 2.3 Finite-difference code for simulating convection in Cartesian geometry . . | 27 |
| 2.3.1 Computational procedure | 27 |
| 2.3.2 Discretization | 29 |
| 2.3.3 Multi-step (predictor-corrector) methods | 30 |
| 2.3.4 Solution of pressure Poisson equation | 31 |
| | |
| 3 Rayleigh-Bénard convection with periodic walls | 34 |
| 3.1 Simulation details and boundary conditions | 35 |
| 3.2 Results | 37 |

| | | |
|----------|---|-----------|
| 3.2.1 | Mean and turbulent quantities | 37 |
| 3.2.2 | Heat flux | 41 |
| 3.2.3 | Turbulent diffusivity | 42 |
| 3.2.4 | Flow field | 44 |
| 4 | Turbulent wind in a cubic confinement | 50 |
| 4.1 | Introduction | 51 |
| 4.2 | Methodology | 51 |
| 4.2.1 | Computational set up | 52 |
| 4.3 | Results and discussion | 54 |
| 4.3.1 | Local heat flux and mean wind | 54 |
| 4.3.2 | Flow structure | 55 |
| 4.3.3 | Analysis of density and velocity fluctuations | 56 |
| 4.3.4 | Wind in turbulent convection and its reversal | 59 |
| 4.3.5 | Time averaged velocity field | 61 |
| 5 | Dependence of heat transport properties on surface roughness with different shapes—a preliminary study | 68 |
| 5.1 | Introduction | 69 |
| 5.2 | Numerical set-up | 71 |
| 5.3 | Results and discussion | 74 |
| 5.3.1 | Flow visualization | 74 |
| 5.3.2 | Near-wall dynamics | 76 |
| 5.3.3 | Local density fluctuations | 78 |
| 5.3.4 | Coherent structures near the wall | 79 |
| 6 | Concluding remarks | 83 |
| | Bibliography | 85 |

List of Figures

| | | |
|------|--|----|
| 2.2 | Coordinates transformation from the physical to the computational space | 28 |
| 2.3 | Distribution of velocities (Cartesian and contravariant) for a two dimensional case in a computational cell. | 29 |
| 3.1 | (a) Grid spacing in the vertical direction of the domain stretched by hyperbolic tangent function, dash line is mean thermal boundary layer thickness at $Ra = 10^8$ and (b) its zoom grid mesh design in $x - y$ plane | 36 |
| 3.2 | Turbulence statistics in global units for different Ra numbers and dynamic approaches as a function of vertical height. (a) resolved root mean square density fluctuations $\rho_{rms}/\Delta\rho$ and (b) resolved root mean square of vertical velocity fluctuations normalized by ν/H . The results are compared with KD00. The curves are labelled as tables 3.1 and 3.2 | 38 |
| 3.3 | (a) The mean density $\langle \rho \rangle$ and (b) resolved density fluctuations ρ_{rms} as a function of y for $Ra = 6.3 \times 10^5$ (solid line), $Ra = 2.5 \times 10^6$ (dashed line), $Ra = 10^7$ (dash dot), $Ra = 10^8$ (dash dot dot) obtained by LDS method. | 40 |
| 3.4 | Resolved horizontal velocity fluctuations as a function of Ra computed by (a) DSM and, (b)(LDS) as a function of y for $Ra = 6.3 \times 10^5$ (dotted), $Ra = 2.5 \times 10^6$ (dashed dot line), $Ra = 10^7$ (dash line), $Ra = 10^8$ (dash dot dot line) | 41 |
| 3.5 | Comparison of components of the Nusselt number computed using LDS as a function of Ra (a) resolved vertical density flux and (b) resolved density gradient along vertical direction | 42 |
| 3.6 | Instantaneous eddy viscosity $\langle \nu \rangle_A/\nu$ at (a) $Ra = 10^8$ and (b) $Ra = 6.3 \times 10^5$ | 43 |
| 3.7 | Profiles of the subgrid Prandtl number as a function of Ra along vertical direction. The insert figure shows close-up near the boundary layer. | 45 |
| 3.8 | (a) 3D view of local instantaneous density $\rho/\Delta\rho_0$ distribution over top and bottom plate at $Ra = 10^7$ and (b) a vertical slice through the centre of instantaneous vertical velocity $v\nu/H$ at $Ra = 2.5 \times 10^6$ and (c) at $Ra = 10^7$ | 46 |
| 3.9 | Snapshot of turbulent Rayleigh-Bénard convection at $Pr = 1$. Plumes are clearly visible through the vertical walls at (a) $Ra = 2.5 \times 10^6$, (b) $Ra = 10^7$ and (c) $Ra = 10^8$, whereas the yellow surfaces reveal the isosurface of density ($\rho = 0.2$) | 47 |
| 3.10 | Time average streamlines of vertical velocity obtained at $Ra = 10^8$, $Pr=1$ and $\Gamma = 1$ | 48 |

| | |
|---|----|
| 4.1 Streamlines within the full convection cell, time-averaged for more than 5296 t_f . Greyscale denotes the intensity of the vertical mean velocity, normalized by the free-fall velocity scale U_f . Figure (a) shows the diagonal containing the mean wind and (b) shows the opposite diagonal, containing the strong, counter-rotating cells. $Ra = 10^6, Pr = 0.7, \Gamma = 1$ | 55 |
| 4.2 Contour plots of local heat flux Nu_w at the top and bottom plates, time-averaged over 5296 t_f . colour scale gives the magnitude of the local heat flux in units of the global Nusselt number. Velocity vectors show the diagonal direction of the LSC for clarity. $Ra = 10^6, Pr = 0.7, \Gamma = 1$ | 56 |
| 4.3 Normalized fluctuations in (a) density, given by $\sigma_\rho/\Delta\rho$ and (b) vertical velocity, given by $\sigma_v H/\nu$, measured at the cell center. The solid lines are the power law fits to the present data: $\sigma_\rho/\Delta\rho = 49.03Ra^{-0.46}$ (top) and $\sigma_v H/\nu = 0.31Ra^{0.39}$ (bottom). Dashed and dash-dotted lines are power law fits, respectively, for the near-cubic cell and cylindrical cell of DE01 for comparison. | 57 |
| 4.4 Time-averaged values of the r.m.s density fluctuations σ_ρ . Greyscale denotes the magnitude of the density fluctuations in units of $\Delta\rho$. Averaging has been performed over 5296 t_f . Figure (a) shows the vertical diagonal plane containing the large scale circulation and (b) the orthogonal plane to it containing the counter-rotating cells. We have included the velocity vectors for clarity. $Ra = 10^6, Pr = 0.7, \Gamma = 1$ | 58 |
| 4.5 instantaneous density iso-surfaces for (a) $Ra = 10^8$, and (b) $Ra = 10^{11}; Pr = 0.7, \Gamma = 1$. Colour range from blue to red for $0.05 < \rho < 0.95$ | 59 |
| 4.6 For $Ra = 10^6$ on a $64 \times 96 \times 64$ grid of $\Gamma = 1$, time series of the vertical velocity measured by the probes at $y=0.5$ (mid-plane) (Top panel) probe 1 is placed $x = z = 0.23$ and probe 3 at $x = z = 0.77$. Time is measured in the units of the free fall time H/t_f (Bottom panel) probe 2 at $x = 0.77, z = 0.23$ and probe 4 at $x = 0.77, z = 0.23$. Time is measured in the units of the free fall time H/t_f | 62 |
| 4.7 For $Ra = 10^8$ on a $64 \times 96 \times 64$ grid of $\Gamma = 1$, time series of the vertical velocity measured by the probes at $y=0.5$ (mid-plane) (Top panel) probe 1 is placed $x = z = 0.23$ and probe 3 at $x = z = 0.77$. Time is measured in the units of the free fall time H/t_f (Bottom panel) probe 2 at $x = 0.77, z = 0.23$ and probe 4 at $x = 0.77, z = 0.23$. Time is measured in the units of the free fall time H/t_f | 62 |
| 4.8 Time average of vertical velocity streamlines . Gray scale denotes the intensity of the vertical mean velocity normalized by the free fall velocity scale U_f ; $Ra = 10^8 ; Pr = 1; \Gamma = 1$. Series of data represents switching of the mean wind. | 63 |
| 4.9 Time averaged density distribution and 3D velocity vectors in the diagonal planes of the cube. The LSC observed in (a) plane and secondary flow structures in plane (b) at $Ra = 10^6$ on grid $64 \times 96 \times 64$ and $\Gamma = 1, Pr = 0.7$. We have also included the velocity vectors for clarity. | 64 |
| 4.10 Time average wall shear stress; colour range from blue to red for $2 < \tau_w < 42$ at $Ra = 10^8$; on the walls (a) is plotted for 4.8-d and (b) is plotted for 4.8-a. Note the coordinate directions. | 65 |

| | |
|---|----|
| 4.11 Time average of vertical velocity streamlines . Gray scale denotes the intensity of the vertical mean velocity normalized by the free fall velocity scale U_f ; $Ra = 10^{11}$; $Pr = 1$; $\Gamma = 1$ and its wall shear stress ranges from blue to red for $20 < \tau_w < 160$ | 65 |
| 5.1 Sketch of grids distribution in vertical direction ($x-y$) view of (a) pyramid and (b) sinusoidal geometries with details of roughness elements. | 73 |
| 5.2 Perspective sketch of convection cells with (a) pyramids and (b) sinusoidal elements distributed over upper and lower plates. All vertical walls are smooth | 73 |
| 5.3 Visualization of 3D large scale mean flow that is obtained by time averaging over $1518t_f$ at $Ra = 10^8$, $Pr = 0.7$ for (a) sinusoidal and (b) pyramid roughness. Both cells shows diagonal direction of mean wind. Gray scale denotes the intensity of the vertical mean velocity, normalized by the free fall scale U_f | 74 |
| 5.4 The time series of vertical velocity measured by probe at $y = 0.5$ (mid-plane) and $x = z = 0.2$ for pyramid cell | 75 |
| 5.5 Instantaneous density field in a vertical section; (a) sinusoidal plate (b) pyramid plate. Gray scale denotes the the magnitude of density, $Ra = 10^8$, $Pr = 0.7$, $\Gamma = 1$ | 77 |
| 5.6 Close up of the flow field near the bottom rough surfaces of figure (5.5);(a) sinusoidal and (b) pyramid elements. Several stream tracers are depicted in black arrowed lines, $Ra = 10^8$, $Pr = 0.7$, $\Gamma = 1$ | 77 |
| 5.7 Absolute (colour) τ_w and contributions of velocity movement (streamlines) of the time averaged wall shear stress on the bottom plate; (a) sinusoidal and (b) pyramid geometries at $Ra = 10^8$, $Pr = 0.7$, $\Gamma = 1$ | 78 |
| 5.8 Time averaged (colour) values of the rms density fluctuations $\sigma_\rho/\Delta\rho$ of pyramid roughness geometry in the plane of (a)The LSC and (b) orthogonal to it. We have included 3D velocity vectors for clarity, $Ra = 10^8$, $Pr = 0.7$, $\Gamma = 1$ | 79 |
| 5.9 Perspective sketch of the cell and close up of pyramid element | 80 |
| 5.10 Visualization of turbulent structure in the bottom plane of, iso-surface of Q; (a) sinusoidal and (b) pyramid geometries $Ra = 10^8$, $Pr = 0.7$, $\Gamma = 1$ | 81 |

List of Tables

| | | |
|-----|---|----|
| 1.1 | Summery of the velocity scaling exponent γ_u reported in several experimental (E), theoretical (T) and numerical (N) studies. All experiments mentioned here have been carried out in cylindrical cell | 14 |
| 3.1 | Simulation parameters for $Pr = 1, \Gamma = 6$ for Direct Numerical Simulation (DNS) and Large Eddy Simulations (D1-D4) with plane averaging over horizontal plates . The number of grid points required $N_x \times N_y \times N_z$ in i -direction $N_i(i = x, y, z)$; N_θ is number of grid points required for resolving the thermal BL; Pr_{sgs} is the sub-grid Prandtl number and Nu is computed Nusselt number. | 37 |
| 3.2 | Simulation parameters for $Pr = 1, \Gamma = 6$ with Lagrangian Dynamic model. The number of grid points $N_x \times N_y \times N_z$ in i -direction $N_i(i = x, y, z)$; Nu_θ number of grid points required in the thermal boundary layer; Nu is the Nusselt number computed on walls. | 37 |
| 4.1 | Computational parameters and heat transport data for cubic cavities and for $Pr = 0.7$ and varying Ra . The number of grid points in the i -direction is given by N_i . N_θ denotes the number of points in the thermal boundary layer; included for comparison are the DNS data on heat transport Kaczorowski <i>et. al</i> (2013) for the same values of Ra | 54 |
| 4.2 | Computational parameters of the simulations, all the computations are at $Pr = 0.7$. N_x, N_y and N_z are, respectively the number of grid points in the i direction. Δ_{min} is the minimum grid spacing and Δ_{max} is the maximum grid spacing along vertical direction; N_θ is the number of nodes set within thermal boundary layer. Nu is the computed Nusselt number compare with Kaczorowski and Xia [2013] | 60 |
| 5.1 | Simulation details of two different roughness geometries.The number of grid points $N_x \times N_y \times N_z$ in i -direction $N_i(i = x, y, z)$; Δ_{min}/H is the minimum grid spacing and Δ_{max}/H is the maximum grid spacing along vertical direction; Nu is the normalized heat flux. | 71 |

To Joe, who taught me the beauty of life ...

Chapter 1

Introduction

More than a century ago, Henry Bénard (1900) performed an interesting experiment. He heated a very thin layer of fluid from below, and the resulting convective motions took the shape of a regular pattern of hexagonal cells. The subsequent theoretical analysis of the convective instability of a layer of fluid was due to Lord Rayleigh (1916). Subsequently the term *Rayleigh-Bénard* convection (RBC) was coined for the subsequent motion of a fluid confined in a thin horizontal layer typically heated from below to maintain an adverse density gradient. The study of turbulent RBC in a cubic confinement by means of numerical simulations is the framework of my thesis. Therefore we first introduce some theoretical aspects of convecting fluids, going from the governing hydrodynamical equations formulated under the Boussinesq approximation to predictions from scaling theories, which are presented in the second part part of this chapter. Finally we will briefly summarize the spacial structure of Large Scale Circulation (LSC) within different cell shapes which is a prominent feature of the confined convection.

1.1 Introductory concepts

Heat transfer is an important scientific subject which has drawn attention of many scientists due to its relevance to many natural and engineering phenomena. One of the more interesting forms of heat transfer is known as *thermal convection*, that occurs throughout nature and technology. In the atmosphere, convection is an important factor in weather prediction at small length and time scales, and for climate prediction at large time scales. The extensive heat adjustment between the equator and the North pole leads to create convection in the ocean. Turbulent convection plays an active role in the generation of magnetic fields within the Earth's outer core, and it is connected to occasional reversals of the geomagnetic field. Convection is not only confined to natural flows, it is also manifest in various forms in industrial applications, for example in nuclear reactors, crystallization processes, solar heating devices (see figure 1.1) etc. In engineering applications, convection is commonly visualized in the formation of micro-structures during the cooling of molten metals and solar ponds. A very common industrial application of natural convection is free air cooling without the aid of fans, this can happen on small scales (computer chips) to large scale process equipments.

In engineering problems as well as natural ones, we know the underlying mathematical equations, however, these equations are generally impossible to solve without simplifying assumptions. These assumptions cause generation of errors in the results, which lead to discrepancies between real world phenomena and results from analytical treatments. For so many years, experimental studies were the only reliable methods for investigating the engineering problems. The advent of computers and their rapid advancement brought an opportunity for scientists to analyses those problems with less simplifying assumptions. The term *Numerical Method* is a very general term attributed to methods solving a set of equations numerically. In this work, however it is referred to those methods which used to solve the conservation equations for mass, momentum and energy. In many texts, the term Computational Fluid Dynamics (CFD) is used instead, which is more specific to this particular application.

The conservation equations are a system of non-linear partial differential equations for which, so far, no mathematical solutions have been found. The three major numerical approaches to solving them are known as, *Direct Numerical Simulation* or DNS, *Reynolds Averaged Navier-Stokes* or RANS, and *Large Eddy Simulation* or LES.

Numerical study of RBC flow have several advantages in comparison to physical experiments: (i) any local or global quantity can be "measured" without restriction, i.e., with probes placed at any desired position. (ii) Unconditional validity of the approximation can be chosen at will. For example one can study fluids which exactly obey the Boussinesq approximation or fluids exhibiting temperature dependence on material property. (iii) Boundary conditions can be chosen as in the idealized RB case, i.e., with exactly

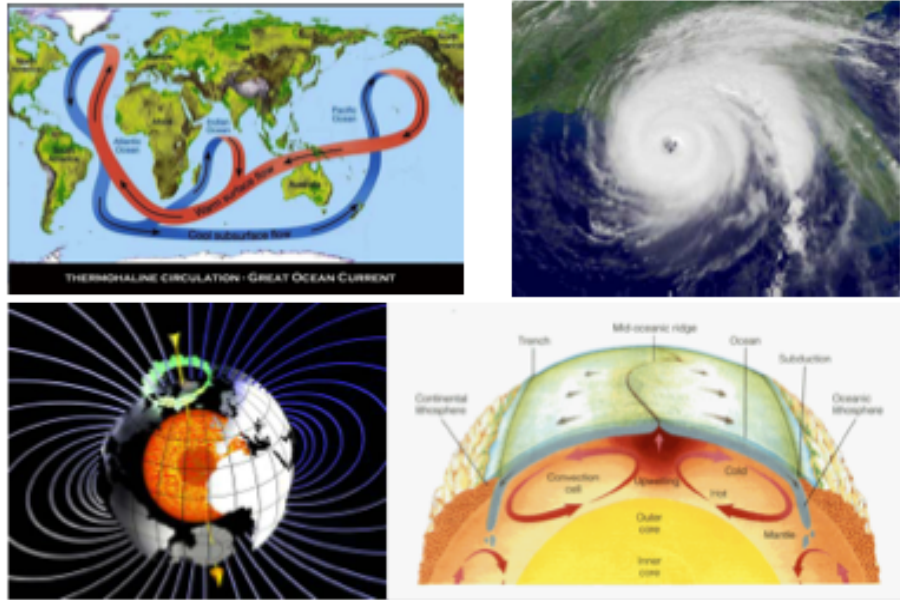


FIGURE 1.1: Examples of natural convection occurring in ocean, atmosphere, earth magnetic field and at the core of sun.

zero heat flux through the side walls. In fact, it has been suggested by [Verzicco and Sreenivasan \[2008\]](#), that boundary conditions in the case of laboratory experiments are perhaps closer to fixed-heat-flux than to fixed temperature of the plates. However there are also major advantages of experimental studies, the main one being accessibility to "ultra" high Ra numbers. Numerous experiments were performed for an increasingly large range of Ra , from $Ra = 10^5$ to 10^{13} with different size of container and fluid properties. But still the highest accessed Rayleigh number of $Ra = 10^{17}$ is in the laboratory experiments by [Niemela et al. \[2000\]](#).

1.2 Theoretical background of Rayleigh-Bénard convection

The exact equations for a heat conducting viscous fluid in presence of gravitational acceleration field can be simplified in a wide range of applications without significant influence on the final results. Boussinesq (1903) suggested that in many circumstances the density variations and compressibility effects can be neglected, apart from the gravitational term (\mathbf{g}) which must be considered. It is then also valid to keep the fluid properties constant, and independent of temperature.

Using the results of the analysis of the validity of the Boussinesq approximation (BO) carried out by [Gray and Giorgini \[1976\]](#), it can be shown that for the parameter range used in this work the approximation is valid. On the basis of this approximation for small ($\leq 10^\circ C$) temperature differences between the bottom and the top of the fluid

layer, the density ρ is:

$$\rho - \rho_0 = -\rho_0\alpha(T - T_0), \quad (1.1)$$

where ρ_0 is the density reference at the temperature reference T_0 . Let the volumetric coefficient of thermal expansion α be small and let the material characteristics of the fluid (kinematic viscosity ν , thermal diffusivity κ , and the coefficient α itself) vary little within the region considered. Then, for not too-fast processes, the density and these characteristics can be considered to be constant everywhere in the equations, with the only exception being that the density variation must be retained in the buoyancy term, where it is multiplied by the gravity acceleration \mathbf{g} .

Lets us briefly look at the origin of the instability. When a fluid parcel is displaced in the vertical direction, the sign of the buoyancy force acting on this parcel depends on the sign of the temperature difference between the parcel and the ambient fluid. Let the state of the fluid in the parcel vary adiabatically. In this case, if the temperature of the medium decreases with height less steeply than the temperature of the parcel, the parcel displaced upward becomes colder than the ambient fluid. Therefore the buoyancy force tends to return the parcel to its initial position, exerting a stabilizing action on the fluid. In contrast, if the temperature gradient in the medium is greater in absolute value than the isotropic gradient, the buoyancy force will be destabilizing.

From the basic science point of view, thermal convection is one of the few systems in which various instabilities, spatio-temporal chaos and different turbulent regimes are observed.

1.3 Equations of motions

1.3.1 The Boussinesq approximation

We start with the general equations that express conservation of momentum, energy and mass for a Newtonian fluid [Landau and Lifshitz, 1959]:

$$\rho \left(\frac{\partial u_i}{\partial t} + u_j \frac{\partial u_i}{\partial x_j} \right) = -\frac{\partial P}{\partial x_i} - \rho g \delta_{i3} + \frac{\partial \sigma'_{ij}}{\partial x_j} \quad (1.2)$$

$$\rho T \left(\frac{\partial s}{\partial t} + u_i \frac{\partial s}{\partial x_i} \right) = \frac{\partial}{\partial x_i} \left(k \frac{\partial T}{\partial x_i} \right) + \sigma'_{ij} \frac{\partial u_i}{\partial x_j} \quad (1.3)$$

$$\frac{\partial \rho}{\partial t} + \frac{\partial}{\partial x_i} (\rho u_i) = 0, \quad (1.4)$$

where viscous stress is defined as $\sigma'_{ij} \equiv \mu\left(\frac{\partial u_i}{\partial x_j} + \frac{\partial u_j}{\partial x_i}\right) - \frac{2}{3}\mu\frac{\partial u_k}{\partial x_k}\delta_{ij} + \mu_B\frac{\partial u_k}{\partial x_k}\delta_{ij}$. These equations determine the evolution of the velocity $\mathbf{u} = (u_1, u_2, u_3)$ density ρ and entropy s in time t , with P the pressure, g the gravitational acceleration (here pointing in the negative x_3 -direction which is vertically downward). Here μ , μ_B and k are the dynamic viscosity, bulk viscosity and thermal conductivity of the fluid respectively. δ_{ij} is the Kronecker delta.

We apply the BO approximation to the above equations, where density variations ρ' with temperature changes T' is approximated by linear relation:

$$\frac{\rho'}{\rho_0} = -\alpha T', \quad (1.5)$$

where T' must remain small, such that $\alpha T' \ll 1$.

Under these conditions, consider the density, pressure and temperature as having small perturbations (ρ', P', T') relative to their equilibrium values (ρ_0, P_0, T_0) : therefore $\rho = \rho_0 + \rho', P = P_0 + P'$ and $T = T_0 + T'$. Starting with equation (1.4) we get:

$$\frac{1}{\rho_0}\left(\frac{\partial \rho'}{\partial t} + u_i \frac{\partial \rho'}{\partial x_i}\right) + \left(1 + \frac{\rho'}{\rho}\right)\frac{\partial u_i}{\partial x_i} = 0. \quad (1.6)$$

By introducing a characteristic velocity and length scale, we can estimate the terms as:

$$\frac{1}{\rho_0}\left(\frac{\rho'}{L/U} + \frac{U\rho'}{L}\right) + \left(1 + \frac{\rho'}{\rho}\right)\frac{U}{L} = \frac{U}{L}(1 - 3\alpha T'), \quad (1.7)$$

where $\alpha T' \ll 1$ is much smaller than the components of the velocity divergence. Hence we arrive at the incompressibility condition:

$$\frac{\partial u_i}{\partial x_i} = 0. \quad (1.8)$$

The momentum equation (1.2) becomes much simpler, the dynamic viscosity can be taken out of the gradient, and the diffusive term reduces to Laplacian of velocity using (1.8). We also subtract the hydrostatic pressure $\partial P_0/\partial x_i = -\rho_0 g \delta_{i2}$. The resulting equation is:

$$\left(1 + \frac{\rho'}{\rho_0}\right)\left(\frac{\partial u_i}{\partial t} + u_j \frac{\partial u_i}{\partial x_j}\right) = -\frac{1}{\rho_0} \frac{\partial P'}{\partial x_i} - g \frac{\rho'}{\rho_0} \delta_{i2} + \nu \nabla^2 u_i \quad (1.9)$$

where kinematic viscosity is $\nu = \mu/\rho_0$. Moreover $\rho'/\rho_0 = -\alpha T' \ll 1$; hence we can neglect it from equation (1.9). Furthermore, the constant density factor is taken in to the pressure gradient. Remembering that pressure and temperature fluctuations must remain small, the perturbation terms but the gravitational one are dropped out and the

resulting equation is:

$$\frac{\partial u_i}{\partial t} + u_j \frac{\partial u_i}{\partial x_j} = -\frac{\partial P}{\partial x_i} + g\alpha T \delta_{i,2} + \nu \frac{\partial^2 u_i}{\partial x_j \partial x_j} \quad (1.10)$$

The entropy equation (1.3) can also be simplified. The thermal conductivity k is taken out of the derivative, which leaves the Laplacian form of temperature. The production of heat by viscous dissipation $\Phi \equiv \sigma'_{ij}(\partial u_i / \partial x_j)$ typically is of order of magnitude 10^7 when compared to the other terms in the above equation [Kundu and Cohen, 2002], so it is neglected. Specific heat at constant pressure is defined as $c_p \equiv T \left(\frac{\partial s}{\partial T} \right)_p$, the derivatives of s can be expressed as:

$$T \frac{\partial s}{\partial t} = c_p \frac{\partial T}{\partial t}, \quad T \frac{\partial s}{\partial x_i} = c_p \frac{\partial T}{\partial x_i}. \quad (1.11)$$

Therefore the equation reduces to:

$$\left(1 + \frac{\rho'}{\rho_0}\right) c_p \left(\frac{\partial T'}{\partial t} + u_i \frac{\partial T'}{\partial x_i} \right) = \frac{k}{\rho_0} \nabla^2 T \quad (1.12)$$

By neglecting the term $\rho'/\rho_0 \ll 1$ and substituting thermal diffusivity $\kappa = k/(c_p \rho_0)$ and dropping the primes, the entropy equation reduces to:

$$\frac{\partial T}{\partial t} + u_i \frac{\partial T}{\partial x_i} = \kappa \nabla^2 T \quad (1.13)$$

In vector notation the set of governing equations under Boussinesq approximation is:

$$\frac{\partial \mathbf{u}}{\partial t} + (\mathbf{u} \cdot \nabla) \mathbf{u} = -\nabla P + g\alpha T \hat{y} + \nu \nabla^2 \mathbf{u}, \quad (1.14)$$

$$\frac{\partial T}{\partial t} + (\mathbf{u} \cdot \nabla) T = \kappa \nabla^2 T, \quad (1.15)$$

$$\nabla \cdot \mathbf{u} = 0 \quad (1.16)$$

Equations (1.14)-(1.16) with specific boundary conditions for temperature and velocity are known as *classical Rayleigh-Bénard problem*. The dimensional equations of the problem contain various dynamical parameters such as thermal expansion coefficient (α), acceleration due to gravity field (\mathbf{g}), viscous diffusion coefficient (ν), thermal diffusivity (κ), etc. However, owing to self similar nature of the dynamics, this large number of dimensional parameters in the problem can be reduced to compact form by choosing a relevant time scale, velocity scale, length scale and temperature scale in the system.

Several ways of passing to non-dimensional variables in the problem are encountered in the literatures (see [Chillà and Schumacher \[2012\]](#)-). We shall employ the most common procedure used in RBC. We take the layer thickness of H as the unit of length, the characteristics temperature scale ΔT which is the temperature difference between the layer boundaries, as temperature scales ($\sim \Delta\rho$). There are three time scales so called: (i) heat diffusion time scale given by H^2/κ , (ii) viscous diffusive time scale given by H^2/ν , and (iii) free fall time scale given by H/U_f where $U_f = \sqrt{\alpha g \Delta T H}$ is defined as free fall velocity. By substituting these dimensionless variables in to equations [\(1.14\)](#) –[\(1.16\)](#) one can obtain:

$$\frac{\partial \mathbf{u}}{\partial t} + (\mathbf{u} \cdot \nabla) \mathbf{u} = -\nabla P + \frac{g\alpha\Delta TH}{U^2} T \hat{y} + \frac{\nu}{UH} \nabla^2 \mathbf{u}, \quad (1.17)$$

$$\frac{\partial T}{\partial t} + (\mathbf{u} \cdot \nabla) T = \frac{\kappa}{UH} \nabla^2 T, \quad (1.18)$$

$$\nabla \cdot \mathbf{u} = 0 \quad (1.19)$$

1.3.2 Dimensionless numbers

In the above equations two important non-dimensional numbers appear. They are defined as Rayleigh number Ra , and Prandtl number Pr :

$$Ra = \frac{\alpha g \Delta T H^3}{\nu \kappa}, \quad Pr = \frac{\nu}{\kappa}. \quad (1.20)$$

The physical interpretation of Ra can be written as:

$$\frac{\text{Buoyancy force}}{\text{Viscous force}} \sim \frac{g\rho}{\nu U_f / H^2} \sim \frac{g\alpha\Delta T}{\nu\kappa / H^3} = \frac{\alpha g \Delta T H^3}{\nu \kappa} = Ra.$$

The non-dimensional Prandtl number named after German physicist Ludwig Prandtl (1875 - 1953) is the ratio of momentum diffusivity (kinematic viscosity) to thermal diffusivity. It can be also related to the thickness of the thermal (λ_θ) and viscous boundary layers (λ_u) (see also section [1.4](#)).

Typically the values of Pr , which is the fluid property, vary from 10^{-8} for the sun's convection zone to the highest $Pr = 10^{25}$ for Earth's convective zone. For instance, some Pr are listed below:

- around 0.015 for mercury

- around $0.7 - 0.8$ for air and many other gases,
- around 7 for water (At 20 degrees Celsius)
- between 100 and 40,000 for engine oil
- around 1×10^{25} for Earth's mantle.

The third important parameter in the study of RBC is *aspect ratio* Γ which characterizes the domain size. In addition, for convective flow in bounded domains (also called "laterally restricted") it is useful to define the aspect ratio Γ more precisely. The domain size, by itself, is of course not sufficient for describing the geometry, since e.g. a cube and a cylinder, both with aspect ratio one, are still different shapes. To our best knowledge the first study, comparing the flow in different geometries in a direct way deals with cylindrical and near cubic convection cell of equal volume and height, belongs to [Daya and Ecke \[2001\]](#). In their experimental study, they measured temperature and velocity fluctuations at moderate Ra numbers up to 4×10^9 in square and cylindrical convection cells that have the same cross sectional area 345cm^2 . They observed that "... *Amazingly, the fluctuations deep in the interior feel the geometry of the container, not just in overall magnitude but in very different power-law scaling with Ra. These results demonstrate that convection in unit-aspect-ratio containers is more complicated than previously assumed and that the fluctuations result from some intricate coupling between the boundary-layer plumes, the large scale circulation, and the inhomogeneous turbulence in the cell interior. Existing scaling theories can not account for such behavior.*" Therefore the influence of the geometry is not negligible at all, for high Ra .

The aspect ratio Γ is defined as the ratio of radius to depth for cylindrical regions and as the ratio of width to depth for square/periodic regions : (see also figure 1.2)

$$\begin{aligned}\Gamma &= \frac{\text{radius}}{\text{height}} && \text{for cylindrical geometry} \\ \Gamma &= \frac{\text{width}}{\text{height}} && \text{for square geometry.}\end{aligned}\tag{1.21}$$

In response to parameters Ra , Pr and Γ , the turbulent transport of heat and momentum is quantified by the Nusselt number and Reynolds numbers, Nu and Re , respectively. They are given by:

$$Nu = \frac{\langle u_y T \rangle_{A,t} - \kappa \frac{\partial \langle T \rangle_{A,t}}{\partial y}}{\kappa \Delta T / H}, \quad Re = \frac{UH}{\nu}.\tag{1.22}$$

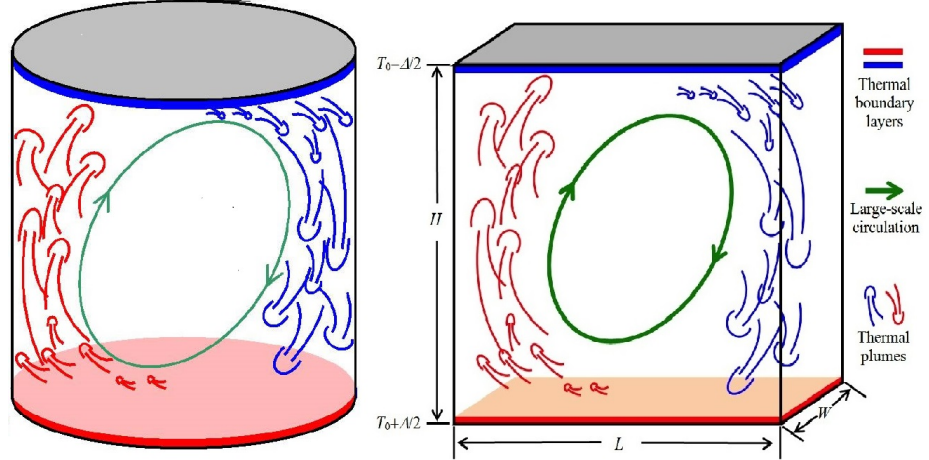


FIGURE 1.2: A diagram showing turbulent thermal convection within different geometries. Fluid at the bottom is heated, thus thermal plumes are formed to ascend while fluid at the top layer is chilled to form cold plumes that descend. The plumes are found to be responsible for the formation of LSC.

The average $\langle \dots \rangle_{A,t}$ is taken over planes at fixed y (is chosen in vertical direction) and time. Velocity U can be U_f or a root-mean-square. The two contributions in the numerator of equation (1.22) are due to the convective ($J_c(\mathbf{x}, t) = u_y T$) and diffusive heat ($J_D(\mathbf{x}, t) = -\kappa \partial_y T$) currents. In the absence of fluid motion ($Ra < Ra_{critical}$) heat can be carried by diffusion only across the fluid layer which will correspond with $Nu = 1$. Two forms of this equation are very useful for the calculation of Nu in numerical simulations. At the horizontal plates convection is zero and the entire heat flux must thus be conductive:

$$Nu = \frac{\partial \langle T \rangle_{A,t}}{\partial y} \Big|_{y=0,H}, \quad \text{because } u_y(y=0, H) = 0 \quad (1.23)$$

where averaging over the upper and bottom plates ($y = 0$ or $y = H$) and in time is adopted.

In non-rotating convection the mean temperature is constant in the well-mixed bulk and the temperature drop is found over the thermal boundary layers. Assuming that the boundary layers carry a conductive heat flux $q = Nu \kappa \Delta T / H$, a very appropriate approximation for the mean thermal boundary layer thickness λ_θ is found:

$$\lambda_\theta = \frac{H}{2Nu}, \quad (1.24)$$

which is a significant parameter in the numerical study of BRC.

1.4 Scaling theories of turbulent transport

1.4.1 Theories for $Nu(Ra, Pr)$ and $Re(Ra, Pr)$

Convective turbulence remains the subject of many studies, since it is very commonly found in nature as well as in industry. Two topics in particular have received a lot of attention in the last years. The first one concerns the scaling properties of thermal transport, that is how the Nusselt number depends on Ra and Pr numbers. The second topic of interest is represented by the effect of buoyancy forces on statistical properties of turbulent fluctuations. As mentioned already, the Nusselt number is the ratio of convective to conductive heat transfer. Despite extensive investigations to date, the dependence of Nu on Ra is still not clear, and the so-called "unifying" theory for $Nu(Ra, Pr)$ presents some discrepancies with experimental results [Ebert et al., 2008].

One of the oldest models for predicting the Nu number as a function of the Ra number goes back to Malkus marginal-stability theory of 1954 which is based on his own laboratory experiments. It assumed that the thermal boundary layer thickness adjusts itself so as the local Ra number, based on the thermal boundary layer thickness, reaches the critical value $Ra_c = O(10^3)$. He derived a scaling law of,

$$Nu \sim Ra^{1/3}. \quad (1.25)$$

The later investigations by Castaing et al. [1989] with higher accuracy in helium ($Pr = 1$ and $Ra \geq 10^6$) and by Ciliberto in (1993) ($Ra < 10^6$), show another scaling

$$Nu \sim Ra^{2/7}. \quad (1.26)$$

Several theoretical interpretations have been offered for this power law but the one that seems most consistent with its occurrence is that by Shraiman and Siggia in 1990 . This theory is based on the relevant dynamical role played by the "Large Scale Circulation" (also known as wind of turbulence in the literature) in turbulent RBC (Qiu and Xia [1998], Niemela et al. [2001], Sreenivasan et al. [2002], Brown and Ahlers [2008]). The onset of the mean flow is due to rising (hot) and falling (cold) plumes from the unstable boundary layer. Without providing a rigorous demonstration of the power law, it is enough to consider that the most important assumption in the Shraiman and Siggia theory is that all kinetic energy dissipation is constrained inside the viscous boundary layers [Benzi et al., 1998].

In the last few years, increasing precision of experimental and numerical results, it became clear that none of the theories for $Nu(Ra, Pr)$ developed in the past could offer a unifying view, accounting for all data. Therefore in the series of papers, Grossmann and Lohse

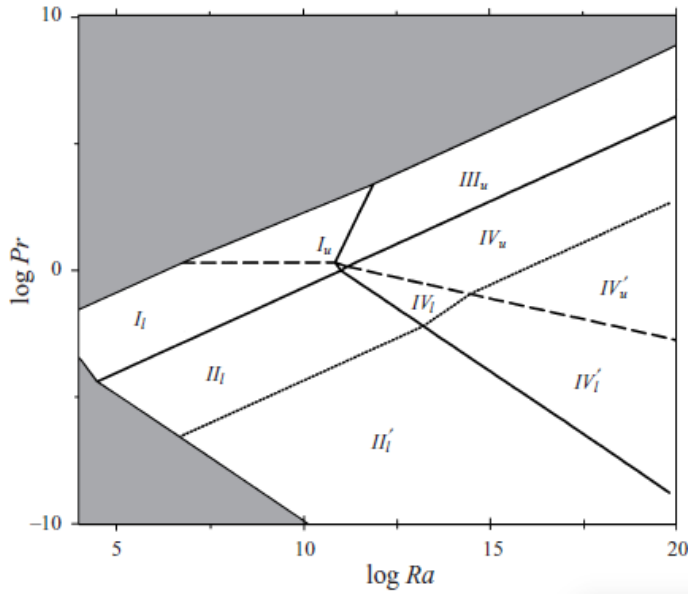


FIGURE 1.3: Phase diagram in $Ra - Pr$ plane indicating the different turbulent regimes in Grossmann and Lohse theory. The dashed line is $\lambda_u = \lambda_\theta$. The dashed regime for large Pr is where $Re \leq 50$, and the shaded regime for low Pr we have $Nu = 1$. The scaling in regime II'_l is therefore as in the bulk-dominated regime IV_l . (This figure is adapted from Grossmann and Lohse [2000], where more details can be found.)

tried to develop a unifying theory to account for both $Nu = (Ra, Pr)$ and $Re = (Ra, Pr)$ over wide ranges of parameters. The central idea of the theory is to decompose globally averaged dissipation rates into their *boundary layer* (BL) and *bulk* (bulk) contributions

$$\epsilon_u = \epsilon_{u,BL} + \epsilon_{u,bulk}, \quad (1.27)$$

$$\epsilon_\theta = \epsilon_{\theta,BL} + \epsilon_{\theta,bulk}. \quad (1.28)$$

The motivation for this decomposition is that the physics of the the bulk and the BL (or BL-like) contributions to the dissipation rates is fundamentally different and thus the corresponding dissipation rate contributions must be modelled in different ways. The term "BL-like" indicates that from a scaling point of view we consider the detaching thermal plumes as parts of the thermal BLs. Thus instead of BL and bulk we could also use the labels *pl* (*plume*) and *bg* (*background*) for the two parts of dissipation rate. A sketch of the splitting is shown in figure 1.2. Therefore one can write equation (1.28) as:

$$\epsilon_\theta = \epsilon_{\theta,pl} + \epsilon_{\theta,bg}. \quad (1.29)$$

Accepting above equations (1.28)-(1.27), the immediate consequence suggests the existence of four regimes: [Grossmann and Lohse, 2004]

- (I) both ϵ_u and ϵ_θ are dominated by their BL contributions;

- (II) in which ϵ_u is dominated by $\epsilon_{u,bulk}$ and ϵ_θ by $\epsilon_{\theta,BL}$;
- (III) in which ϵ_u is dominated by $\epsilon_{u,BL}$ and ϵ_θ by $\epsilon_{\theta,bulk}$;
- (IV) both ϵ_u and ϵ_θ are dominated by their bulk contributions.

For small Pr the viscous boundary layer is smaller than the thermal one $\lambda_u \ll \lambda_\theta$, therefore regime *I* is expected, and for large Pr , it is $\lambda_u \gg \lambda_\theta$ and we have regime *III*. More details about the scaling can be found in [Grossmann and Lohse, 2000, 2004]. Therefore depending on whether λ_u is lesser or larger than λ_θ , each regime is divided onto by two subregimes; the index *l* for lower λ_u and *u* for upper λ_u . At which line $Pr(Ra)$ in phase space $\lambda_u = \lambda_\theta$ the crossover from the $\lambda_u < \lambda_\theta$ to the $\lambda_u > \lambda_\theta$ (see figure 1.4).

For instance, for $Ra = 10^5$ and $Pr = 7$ the Nusselt number is located in the area I_l as shown in figure (1.4). Moreover the scaling proposed for this particular regime is:

$$Nu \sim Ra^{1/4} Pr^{-1/12}, \quad \& \quad Re \sim Ra^{1/2} Pr^{-5/6}. \quad (1.30)$$

It is worth mentioning that our work is ranged on low Pr numbers. Therefore our scaling $Nu(Ra)$ is placed at the sub-regimes of I_l , II_l and II'_l for Ra up to 10^{11} (see figure 1.4).

1.4.2 Temperature fluctuations

The second issue we want to address here regards the temperature (density) and velocity *fluctuations*. Based on the splitting the flow into the plume and background dominant regimes, Grossmann and Lohse [2004] defined total thermal fluctuation as the sum of *root-mean-square* of thermal background fluctuations $\sigma_{\theta,bg}$ and thermal fluctuations caused by plumes $\sigma_{\theta,pl}$:

$$(\sigma_\theta)^2 = (\sigma_{\theta,bg})^2 + (\sigma_{\theta,pl})^2. \quad (1.31)$$

Depending on where in the cell the fluctuations are measured, they will be either dominated by the plume fluctuations or by the background fluctuations. The photograph and movies of the Shang et al. [2003] group suggests that the side walls are plume dominated and the centre is background dominated, potentially leading to different scaling behavior. Indeed, that fluctuations can scale differently at different locations in the cell has been found by Daya and Ecke [2001]. They measured normalized temperature fluctuations in a cell centre of cylindrical cell filled with water and reported $\sigma_\theta/\Delta T \sim Ra^{-0.1 \pm 0.02}$. Niemela et al. [2000] observed $\sigma_\theta/\Delta T \sim Ra^{-0.145}$ with helium gas; Castaing et al. [1989] get $\sigma_\theta/\Delta T \sim Ra^{-1/7}$ in helium gas too. The numerical results of Lakhariju et al. [2012]

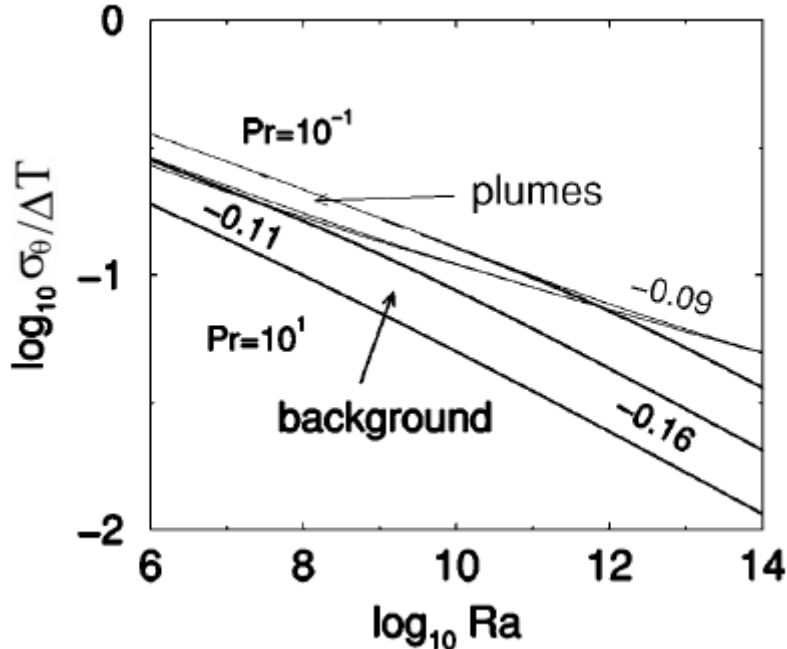


FIGURE 1.4: $\sigma_{\theta,bg}/\Delta T$ (solid black lines) and $\sigma_{\theta,pl}/\Delta T$ (gray lines) as functions of Ra for $Pr = 10^{-1}, 10^0$ and 10^1 , top to bottom. For $\sigma_{\theta,bg}/\Delta T$ the local slopes typically vary between -0.13 and -0.16 for $Pr=10$ and -0.11 and -0.16 for $Pr=10^{-1}$. For $\sigma_{\theta,pl}/\Delta T$ the local slopes typically vary between -0.11 and -0.09 for all given Pr . This figure is adapted from [Grossmann and Lohse \[2004\]](#) where more details can be found.

shows temperature scaling exponent decreases from -0.18 in the cell centre to -0.20 near the side wall for $Pr = 5.2$.

1.4.3 Velocity fluctuations

The local exponent of (bulk) velocity fluctuations $\sigma_v H/\nu \sim Ra^{\gamma_u}$ is measured at convection cell. [Daya and Ecke \[2001\]](#) also measured *rms* velocity fluctuation $\sigma_v H/\nu$ with Ra at the cell centre of the cylindrical cell and found 0.50 ± 0.05 . [Qiu et al. \[2004\]](#) also found 0.55 with $Pr = 5.4$ at cell centre. [Shang et al. \[2008\]](#) measured $\sigma_v H/\nu$ at three different locations of the cylindrical cell filled with water $Pr = 4.4$. The component γ_u decreases from 0.49 in the cell centre to 0.46 near the side wall. The numerical results of [Lakharaju et al. \[2012\]](#) shows the velocity scaling exponents increase smoothly from $\gamma_u = 0.44$ in the cell centre to $\gamma_u = 0.49$ near the side wall.

Table 1.1 summarizes the data for the scaling exponents available in the literature and mentioned above. There are some differences among the values reported. Owing to the fact that the spacial dependence of these quantity, also due to the use of different experimental techniques which measure somewhat different quantities,

| Case | | Ra | Pr | Γ | $\gamma_u(\text{centre})$ | $\gamma_u(\text{sidewall})$ |
|----------------------------|---|------------------------------------|----------|----------|---------------------------|-----------------------------|
| Castaing et al. [1989] | E | $4 \times 10^7 - 6 \times 10^{12}$ | 0.65-1.5 | 1 | 0.491 ± 0.002 | - |
| Daya and Ecke [2001] | E | $2 \times 10^8 - 4 \times 10^9$ | 5.46 | 0.79 | 0.5 ± 0.03 | - |
| Niemela et al. [2001] | E | $15 \times 10^6 - 10^{13}$ | 0.7 | 1 | - | 0.5 |
| Qiu et al. [2004] | E | $10^8 - 10^{10}$ | 5.4-5.5 | 1 | 0.55 | 0.46 |
| Grossmann and Lohse [2004] | T | $10^6 - 10^{14}$ | 0.1-10 | 1 | 0.39 | - |
| Shang et al. [2008] | E | $10^8 - 10^{10}$ | 4.4 | 1 | 0.49 ± 0.03 | 0.46 ± 0.03 |
| Lakharaju et al. [2012] | N | $2 \times 10^2 - 2 \times 10^9$ | 5.2 | 1 | 0.44 ± 0.01 | 0.49 ± 0.01 |

TABLE 1.1: Summary of the velocity scaling exponent γ_u reported in several experimental (E), theoretical (T) and numerical (N) studies. All experiments mentioned here have been carried out in cylindrical cell

1.5 Large Scale Circulation and its associated dynamics in confined convection cells

Coherent structures can be defined as patterns of motion which can be clearly distinguished from the turbulent background and occur repeatedly in time or space. This general definition enables us to treat, for example, small scale vortical structures in the boundary layers as well as one single large scale roll as coherent structures. In turbulent Rayleigh-Bénard convection the thermal plumes detach from the thermal boundary layers (cold and hot) and have a tendency to organize in a way to span over the entire cell. This single roll known as “Large Scale Circulation”(LSC) or wind of turbulence [Niemela et al., 2001, Putheveettil and Arakeri, 2005, Sun and Xia, 2005] (as shown in figure 1.2). It is a coherent structure of the flow in which the fluid particle ascends from one side of the wall and descends from the opposite side. Therefore geometrical features and dynamics of the LSC depends on the symmetry and aspect ratio of the sample. Here we focus on cubical cell with $\Gamma = 1$ to compare our results with experiments and numerical simulations.

Different patterns and dynamics of LSC have been studied experimentally, numerically and theoretically. Most studies have been done for flows occurring in cylindrical confinement, while for square cross-section the results are few.

For cylindrical containers it has been observed in laboratory experiments that the vertical plane containing LSC undergoes a diffusive motion in the azimuthal direction [Lakharaju et al., 2012]. This phenomena called reorientation of the LSC. For containers with aspect ratio one, essentially one LSC roll (single-roll mode) is expected. In case, if the aspect ratio is larger or smaller than one, two or more circulation rolls can be present next to each other or one roll may be stacked on top of the other (double-roll mode)? In cases when there is re-orientation of the wind, it is called a “reversal”. Niemela et al. [2001]

and Sreenivasan et al. [2002] performed convection experiments on helium gas confined in cylindrical container and they reported reversals of LSC using two probes near the lateral walls in the bulk of convective flow. Qiu and Xia [1998] performed an experiment with water as a working fluid and Ra vary between 10^8 to 10^{10} in cubic sample of $\Gamma = 1$ and found stable single role align diagonal direction of cube. To determine the direction of LSC, they inserted a thin stainless steel tube (diameter ~ 1 m) with a very light string attached to its end into the convection cell; near the horizontal plate. They observed the unidirectional flow in diagonal plane, while orientational oscillations was not found in their experiments . Later on, they used the same experimental set up to study spatial structure of viscous boundary layer over horizontal conducting plate, they found secondary flow that sometimes have opposite directions to the main LSC direction and these secondary flows could affect the stability of the main LSC

Sun et al. [2008] performed similar experiment in rectangular convection cell using water as convecting fluid with $10^9 \leq Ra \leq 10^{10}$ and fixed Prandtl number 4.3. They also found that the LSC align with the largest diagonal of the system and has most stable structure compare to cylindrical and cubical cell. later on, Sugiyama et al. [2010] performed experimental study on (quasi-) two dimensional (2D) rectangular geometry and Direct Numerical Simulation of two-dimensional Boussinesq approximation with water as working fluid at $28^\circ C$ (corresponding to $Pr = 5.7$). They used particle image velocimetry (PIV) method for direct visualization of the flow. Moreover for both experiments they used angular momentum which defined as:

$$L(t) = \langle -(y - H/2)u_x(\mathbf{x}, t) + (x - H/2)u_y(\mathbf{x}, t) \rangle_v \quad (1.32)$$

where $\langle \dots \rangle_t$ representing average over the full volume. The time dependent of L from simulation and experiment reveals the reversal through a sign changes. They found the corner flow play a crucial role for the large scale wind reversals, while the mail roll is diagonally oriented in the cell, smaller counter rotating rolls develop in diagonally opposing corners. They are energetically fed by detaching plumes from the boundary layers trapped in the corner flows, leading to their growth. once the two corner flow have reached a linear extension of $\approx H/2$ they destroy the main convection roll and establish another one circulating in opposite direction.

Several experiments have studied the dependence of LSC on geometrical shape and aspect ratio. Huang et al. [2013] Studied RBC by means of laboratory experiments and DNS. They performed experiments in several cells where height H and length L are fixed $\Gamma_{||} (= L/H)$ with varying width W equal to 1, 0.5, 0.25, 0.125, 0.625 giving the aspect ratios $\Gamma_{\perp} (= W/H)$ equal to $\Gamma = 1, 1/2, 1/4, 1/8, 1/16$ at fixed $Pr = 4.3$ and $Ra = 1 \times 10^9$. They found for the $\Gamma = 1/2$, cold plumes are brought down by the LSC mostly along one side of the cell so that they predominantly fall on one region of the plate, and the

spreading fluid generated by the impingement pushes the hot plumes away and mostly in one direction which also observed in their laboratory experiments. They found in the $\Gamma = 1/8$ the stable single-roll no longer exists, the cold plume brought down by the flow at random positions in the bottom plate. This is due to the drag force from the wall increases and it make the flow slow down from vertical motion. Therefore flow motion in this highly confined geometry becomes one dimensional. for the $1/16$ is qualitatively same as the $1/8$.

Chapter 2

Large Eddy Simulation of Rayleigh-Bénard Convection: Numerical Details

In this chapter, we present the details of the numerical method to investigate turbulent Rayleigh-Bénard convection. We start with the dynamic Smagorinsky model and evaluation of how well these models can reproduce the true impact of the small scales on large scale physics and how they perform in numerical simulations for Rayleigh-Bénard convection. Next, we describe the numerical algorithm to solve the governing equations in Cartesian frame of reference.

2.1 Numerical methods

In the past, due to the complexity of the system, analytical solutions of these equations (1.17)-(1.19) were restricted to very simple cases and as a result the experimental approach was the only method to tackle this problem. The experimental approach is mainly based on the similarity analysis, so that the measurements made in the laboratory, can be used to describe the universal behavior of the system. A large part of the fluid mechanics community is still involved in experimental analysis. But thanks to the rapid growth of computer power and the reduction of computer cost, experiments become more and more expensive compared to the numerical approaches.

One of the major goal in this field is to archive high Ra regime either by means of physical or numerical experiments whose heat transfer and strength of turbulence become independent of the kinematic viscosity and the thermal diffusivity. The physics of this asymptotic regime is that the thermal and kinetic boundary layers, and thus the kinematic viscosity ν and the thermal diffusivity κ , do not play an explicit role any more for the heat flux. The flow then is bulk dominated [Ahlers et al. \[2009\]](#).

Three main well-known numerical procedures are now in use for the computation of turbulent Rayleigh-Bénard convection; (i) Direct Numerical Simulations (DNS), (ii) Large-Eddy Simulations (LES), and (iii) an statistical approach based on the Reynolds Averaged Navier-Stokes (RANS) equations.

The most accurate numerical method is DNS when the equations of motion are discretized on a spatio-temporal grid and resolve all features of the turbulent flow down to the smallest physical scale which is on average the Kolmogorov length η_K for $Pr \leq 1$ or the Batchelor scale $\eta_B = \eta_K / \sqrt{Pr}$ for convection at $Pr > 1$. The results of DNS contain more detailed information about the flow at a large number of grid points. These results can be used to produce statistical information. In a DNS all the kinetic energy dissipation occurs at the smallest scales, are captured. If the mesh is fine enough to resolve even the smallest scale of motion, and the scheme is designed to minimise the numerical dispersion and dissipation errors, one can obtain an accurate three dimensional time-dependent solution of the governing equations completely free of modelling assumption. Over past decades Rayleigh-Bénard convection has been studied extensively by means of DNS see [[Kerr, 1996](#), [Amati et al., 2005](#), [Kunnen et al., 2008](#), [Kaczorowski and Xia, 2013](#), [Kunnen et al., 2009](#), [Lakharaju et al., 2012](#)]. One of the first 3D simulations carried out by DNS is belong to [Kerr \[1996\]](#). He employed lateral periodic BCs ($L_x \times L_y \times L_z = 6 : 1 : 6$, y is upward vertical) and achieved $Ra = 2 \times 10^7$ on the $288 \times 96 \times 288$ grids. For $Pr = 0.7$ he found an effective power law $Nu \sim Ra^{0.28}$. Latter, [Kerr and Herring \[2000\]](#) extended these simulations to Prandtl numbers in the range $0.07 < Pr < 7$, finding $Nu \sim Ra^{0.25}$ for the smallest Pr and effective exponents consistent with $2/7$ for $Pr \geq 0.7$.

A second class of DNS for RB convection is that of Lattice-Boltzmann (LB) simulations

[Benzi et al. \[1994\]](#). In one of the first large Lattice-Boltzmann simulations [Benzi et al. \[1998\]](#) achieved $Ra \approx 3.5 \times 10^7$ and found $Nu \sim Ra^{0.283 \pm 0.003}$ with $Pr = 1$.

The third class DNS is based on finite difference or finite volume. [Verzicco and Camussi \[1999\]](#), employed finite difference simulations for studying Nu and Re vs Ra for several Pr numbers up to 2×10^7 . The advantage of this method is that the correct no-slip BCs at the side walls can be easily implemented and that simulations can also be performed efficiently in the cylindrical geometry as used in many experiments, so that a direct comparison with the experimental results is possible. A further advantage of finite-difference or finite volume is that the spatial resolution can be easily adjusted at will. The grid spacing can be refined in the BLs and becomes coarser in the bulk. Later on, [Verzicco and Camussi \[2003\]](#) and [Stringano and Verzicco \[2006\]](#) extended their earlier simulations to the remarkably high $Ra = 2 \times 10^{11}$ for a slender cell with $\Gamma = 1/2$ and $Pr = 0.7$. Their study focused on the flow organization in the cell in this domain. They reported, beyond $Ra = 10^{10}$ and for $Pr \approx 0.7$, the single convection roll can break up into two smaller counter rotating rolls, each approximately of aspect ratio 1. [Stringano and Verzicco \[2006\]](#) in addition showed that the thermal properties of the side walls can stabilize the large scale convention roll.

At present, the largest Ra achieved by DNS is the one by [Amati et al. \[2005\]](#) and [Verzicco and Sreenivasan \[2008\]](#). They achieved up to $Ra = 2 \times 10^{14}$ for $\Gamma = 1/2$ and $Pr = 0.7$, although, as recently shown by [Stevens et al. \[2010\]](#), at the prize of under-resolving the fine structures of the flow, which leads to Nusselt numbers that are too large.

The DNS simulations of [Shishkina and Wagner \[2007, 2008\]](#) are also based on a finite volume scheme for Ra up to 2×10^9 with $Pr = 5.4$ in a cylindrical container. But at $Ra = 10^{10}$ they employed well-resolved LES. In this sub-grid modelling the length scales in the dissipative and diffusive regime are under resolved.

So far, DNS has been a very useful tool to study turbulent RBC but it has some limitations, for example to resolve all scales of motion, the computational cost is quite high. For the fixed $Pr \approx 1$ the required CPU time increases roughly as $Ra^{3/2}$ and the spacial resolution requirements increases with the cube of Reynolds number Re^3 . So, practically the method is inapplicable at high Ra numbers.

An alternative to DNS is using RANS, which is based on time-averaged of equation of motion. The idea behind the equations is the “Reynolds decomposition”, whereby an instantaneous quantity is decomposed into its time-averaged and fluctuating quantities ($u(\mathbf{x}, t) = \bar{u}(\mathbf{x}) + u'(\mathbf{x}, t)$). Doing so, one introduces a new set of unknown variables, namely the *Reynolds stresses*, $-\overline{\rho u'_i u'_j}$, so no longer the system of equations can be considered closed. While the small scales tend to depend only on viscosity and may be somewhat universal, the large ones are affected very strongly by the boundary conditions. [Kenjeres and Hanjalic \[2002\]](#) applied RANS method to RB convection for $Ra = 10^5$ and

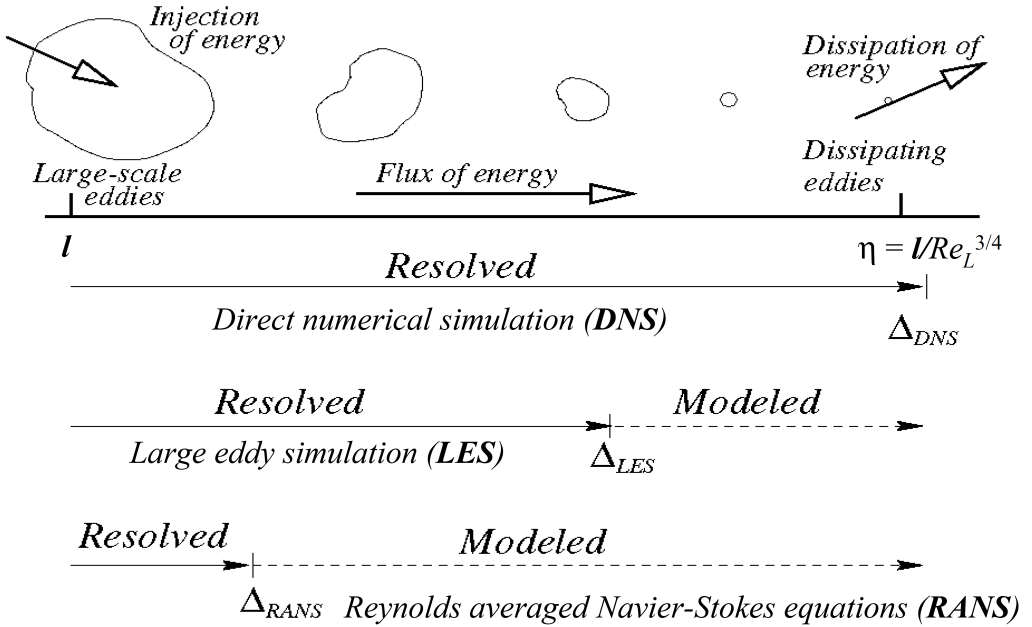


FIGURE 2.1: Schematic representation of the concept of DNS, LES and RANS models to energy cascade (see text)

$Ra = 10^{15}$. They found $Nu \sim Ra^{0.31}$ and for the last two Ra decades some reorganisation of the plumes and the slightly enhanced Nusselt number were observed, but given the progressively decreasing spatial resolution of the numerical scheme at these high Ra the implications of this finding are presently unclear and a detailed discussion of RANS of RB flow is beyond the scope of this thesis.

Large Eddy Simulation (LES) is a technique intermediate between the DNS of turbulent flows and the solutions of RANS. In LES the contribution of large, energy carrying, structures are computed exactly, and only the effect of smallest scales tend to be parametrized. Since the small scales tend to be more homogeneous and universal, and less affected by the boundary conditions than the large ones, the model is simple and require minor adjustments when applied to different flows (see figure 2.1). In this thesis we deal with Large Eddy Simulation to solve 3D time dependent NS equations for three different geometries. We use LES method in our study in order to have very long time-series of dynamic quantities. In order to capture reversal of LSC we provide very long time simulations which may be quite costly with DNS method.

The LES formulation and filtering procedure are presented in this chapter. The dynamic Smagorinsky model is used for sub-grid scale modelling. Both the classical model and the dynamic model, [Germano et al. \[1991\]](#) are available in our in-house code.

2.2 Large Eddy Simulation techniques

In LES one computes explicitly the motion of large-scale structures (or eddies), while modelling the nonlinear interactions with the small scales. This avoids the problem of the RANS method of having to model also the large-scale, energetic and boundary condition dependent motion and at the same time the problem of DNS of having to resolve small scale dissipative motion. The largest eddies extract energy from the main field directly, while the eddies that are somewhat smaller take their energy from the largest ones through a vortex stretching mechanism. On average, kinetic energy moves from large to small eddies. These smallest scale presented a universal and tend to be isotropic, therefore easier to be modelled. The large energy-containing eddies and the small dissipative scales are separated by a range of scales, called the inertial sub-range and energy is transferred when neither energy production nor energy dissipation are important. Thus the large scales are dependent on the large scale flow characteristics while the small, homogeneous react more rapidly perturbations and recover quickly to equilibrium. Therefore the time dependent governing equations for the large eddies are obtained after filtering. The filtering operation can be written in terms of convolution integral:

$$\bar{f}(x) = \int_D G(x - x') f(x') dx' \quad (2.1)$$

Where f is the flow field variable before filtering, \bar{f} is the variable after applying filter function G with $\bar{\Delta}$ as a filter width on domain D . There are various kinds of filter functions, in our study we consider a top-hat filter defined in real space as:

$$G(x) = \begin{cases} 1/\bar{\Delta} & \text{if } |x| \leq \bar{\Delta}/2 \\ 0 & \text{otherwise} \end{cases}$$

All the structures that are smaller than $\bar{\Delta} = (\Delta_x \Delta_y \Delta_z)^{1/3}$ must be modeled. When the filtering operation is applied to the governing equations the later take the following form:

$$\frac{\partial \bar{u}_j}{\partial x_j} = 0, \quad (2.2)$$

$$\frac{\partial \bar{u}_i}{\partial t} + \frac{\partial \bar{u}_j \bar{u}_i}{\partial x_j} = -\frac{1}{\rho_0} \frac{\partial \bar{P}}{\partial x_i} + \nu \frac{\partial^2 \bar{u}_i}{\partial x_j \partial x_j} - 2\Omega_i \times \bar{u}_i - \frac{\bar{\rho}}{\rho_0} g_i \delta_{i2} - \frac{\partial \tau_{ij}}{\partial x_j}, \quad (2.3)$$

$$\frac{\partial \bar{\rho}}{\partial t} + \frac{\partial \bar{u}_j \bar{\rho}}{\partial x_j} = k \frac{\partial^2 \bar{\rho}}{\partial x_j \partial x_j} - \frac{\partial \lambda_j}{\partial x_j}. \quad (2.4)$$

They are respectively the continuity and momentum and energy equations written for the density. It should be stressed we do not consider the effect of Earth's rotation in

our results ($\Omega_i = 0$) . The non-linear term $u_i u_j$ in the equation (1.10) leads to the filter quantity $\overline{u_i u_j}$ in the advective term. When this is expressed as advection of the resolved quantities $\bar{u}_i \bar{u}_j$ in the advective term, the difference

$$\tau_{ij} = \overline{u_i u_j} - \bar{u}_i \bar{u}_j \quad (2.5)$$

represents the effect of the unresolved fluctuations on the resolved motion, acting like stresses which are therefore called subgrid-scale stresses. These stresses must be model by subgrid-scale (SGS) model which represents the effect of the subgrid-scales on the resolved motion. Similarly, in the filtered scalar transport equation (2.4)a term

$$\lambda_j = \overline{u_j \rho} - \bar{u}_j \bar{\rho} \quad (2.6)$$

appears which is the subgrid- -scale turbulent flux and represents the effect of the unresolved small scale motion on the resolved scalar field. Indeed the summation of both unresolved and SGS quantity represents the total turbulent quantities.

2.2.1 Smagorinsky subgrid-scale model

The most popular eddy-viscosity SGS model is the Smagorinsky model [Smagorinsky, 1963]. In analogy to viscous stress in laminar flows, the anisotropic stress tensor τ_{ij} is approximated by relating it to resolved rate of strain, \bar{S}_{ij} , which involves velocity gradients, via an artificial eddy (or turbulent) viscosity ν_{sgs} as:

$$\tau_{ij} - \frac{\delta_{ij}}{3} \tau_{kk} \approx -2(C_s \bar{\Delta})^2 | \bar{S} | \bar{S}_{ij} \quad (2.7)$$

with the resolved strain rate tensor:

$$\bar{S}_{ij} = \frac{1}{2} \left(\frac{\partial \bar{u}_i}{\partial x_j} + \frac{\partial \bar{u}_j}{\partial x_i} \right) \quad (2.8)$$

having contraction $| \bar{S} | = (2\bar{S}_{ij}\bar{S}_{ij})^{1/2}$ and $\nu_{sgs} = (C_s \bar{\Delta})^2 | \bar{S} |$ is eddy viscosity.

In the original Smagorinsky model , the coefficient C_s is assumed to be a global adjustable parameter. The dynamic Smagorinsky model (DSM) removes the limitation by dynamically computing the model coefficient from the resolved field and allowing to vary it in space and time $C_s(\mathbf{x}, t)$.

Formally the dynamic procedure is based on Germano identity [Germano et al., 1991], written as:

$$L_{ij}(\mathbf{x}, t) = \tau_{ij}^{\alpha \Delta}(\mathbf{x}, t) - \widehat{\tau_{ij}^{\Delta}(\mathbf{x}, t)}, \quad (2.9)$$

where $L_{ij} = \widehat{\bar{u}_i \bar{u}_j} - \widehat{\bar{u}_i} \widehat{\bar{u}_j}$ denotes the *resolved turbulent stress*, and $\tau_{ij}^{\alpha\Delta} = \widehat{\bar{u}_i \bar{u}_j} - \widehat{\bar{u}_i} \widehat{\bar{u}_j}$ is the SGS stress on the test filter level, where $\widehat{\cdot}$ denotes test filtering with a filter width twice than grid filter $\widehat{\Delta} = \alpha\Delta$. Substitution of these expressions into the 2.9, the error can be defined as:

$$e_{ij} = L_{ij} - 2\Delta^2 [C_s^2 \widehat{|\bar{S}| \bar{S}}_{ij} - 4C_s^2 \widehat{|\bar{S}|} \widehat{\bar{S}}_{ij}] \quad (2.10)$$

Here we follow [Lilly \[1992\]](#) in minimizing this error in a least square sense where C_s^2 is constrained to have no variation over homogeneous spatial directions to yield:

$$C_s^2 = \frac{\langle L_{ij} M_{ij} \rangle}{\langle M_{ij} M_{ij} \rangle}, \quad (2.11)$$

where,

$$M_{ij} = 2\Delta^2 [\widehat{|\bar{S}| \bar{S}}_{ij} - 4\widehat{|\bar{S}|} \widehat{\bar{S}}_{ij}] \quad (2.12)$$

and where the angled brackets $\langle \dots \rangle$ represent an average over homogeneous direction(s). However the dynamic model coefficient offers several advantages compared to the constant coefficient model C_s but still it is not a particularly good representation of small scale turbulence. This point has been reinforced by simulation results near solid boundaries that show significant errors. The value of C_s in equation (2.11) can exhibit two undesirable properties. First it is possible for C_s to get negative values ($C_s < 0$) and in the context of Smagorinsky model this implies a negative SGS eddy viscosity. Since this is employed in the Boussinesq hypothesis, we see that the result is equivalent to a “backward heat equation” a mathematically ill-posed formulation. But because this typically occurs at only a limited number of points on a computational grid it can be remedied by averaging, typically in directions in which the flow exhibits homogeneity if any. The second difficulties with C_s is that it can not become unbounded, since in principle the denominator can be zero. But [Sagaut \[2001\]](#) argues that this is more an implementation problem than a theoretical one because the numerator of this expression also goes to zero at the same time, and at the same rate, as does the denominator. So we conclude this brief treatment of dynamic models by emphasising that in the end they are still eddy viscosity models, and hence based on the Boussinesq hypothesis, which has no physical basis and moreover presents poor mathematics. But in addition , for the specific case of dynamic models tend to reproduce physics better than do simple Smagorinsky models especially for wall-bounded shear flows. The underlying reasons for the are not well founded in either mathematics or physics leaving open the question of whether such models, or any others based on eddy viscosity, could be ever truly predictive.

2.2.2 Lagrangian Dynamic Smagorinsky model

Difficulties in applying equation (2.11) arises in flows that do not possess direction of statistical homogeneity. [Carati et al. \[1995\]](#) propose ensemble averaging of many simulations that do not require homogeneous directions.

Another option is time averaging. To comply with Galilean invariance, time averaging should be formulated in Lagrangian frame of reference. The Lagrangian dynamic model ([Meneveau et al. \[1996\]](#)) accumulates the required averages over flow path-lines by backwards time integration, with a weighting function that gives decreasing weights to past events. An exponential weighting function allows one to write the required averages as the solutions to pair of forward relaxation transport equations. The chosen relaxation time scale increases when $L_{ij}M_{ij} < 0$, to prevent the coefficient from becoming negative. This formulation has been applied successfully to force and decaying isotropic turbulence and in fully developed transitional channel flow ([Meneveau et al. \[1996\]](#)), in particle-laden flows, in reacting flows in non-equilibrium flows and in simulations on unstructured deforming meshes. Owing to the relatively short time scale, the model is capable of responding quickly to unsteadiness in the mean flow.

Therefore Lagrangian averaging is physically appealing considering the Lagrangian nature of the turbulence energy cascade. In essence, Lagrangian Dynamic Smagorinsky attempt to minimize the path-line average of the local Germano-identity error (GIE) squared. The fluid trajectory in earlier time ($t' < t$) is given by:

$$\mathbf{z}(t') = \mathbf{x} - \int_{t'}^t \bar{u}_i[\mathbf{z}(t''), t''] dt''. \quad (2.13)$$

In terms of the Lagrangian description the error to be minimized, equation (2.10), is:

$$e_{ij}(\mathbf{z}, t') = L_{ij}(\mathbf{z}, t') - C_s^2(\mathbf{x}, t) M_{ij}(\mathbf{z}, t') \quad (2.14)$$

where M_{ij} is defined in equation (2.12). The model coefficient to be used at time t and position $\mathbf{x}(C_s^2)(\mathbf{x}, t)$ is determined by minimizing the error over the trajectory of the fluid particle. In other worlds, previous information along the path line is employed in order to determine the current value of the coefficient. Therefore the total error to be minimized is defined as the path-line accumulation of the local error squared:

$$E = \int_{pathline} e_{ij}(\mathbf{z}) e_{ij}(\mathbf{z}) d\mathbf{z} = \int_{-\infty}^t e_{ij}(\mathbf{z}(t'), t') e_{ij}(\mathbf{z}(t'), t') W(t - t') dt', \quad (2.15)$$

where \mathbf{z} is the trajectory of a fluid particle for earlier times $t' < t$ and W is a weighting function to control the relative importance of events near time t , with those at earlier

times. The total error then is minimized with respect to C_s^2 by enforcing:

$$\frac{\partial E}{\partial C_s^2} = \int_{-\infty}^t 2e_{ij} \frac{\partial e_{ij}}{\partial C_s^2} W(t-t') = 0. \quad (2.16)$$

Making use of above equations and solving for C_s^2 one obtains:

$$C_s^2(\mathbf{x}, t) = \frac{\mathfrak{I}_{LM}}{\mathfrak{I}_{MM}}, \quad (2.17)$$

where,

$$\mathfrak{I}_{LM}(\mathbf{x}, t) = \int_{-\infty}^t L_{ij} M_{ij}(z(t'), t') W(t-t'), \quad (2.18a)$$

$$\mathfrak{I}_{MM}(\mathbf{x}, t) = \int_{-\infty}^t M_{ij} M_{ij}(z(t'), t') W(t-t'). \quad (2.18b)$$

Choosing the time weighting function of the form $W(t-t') = T^{-1}e^{-(t-t')/T}$ yields two transport equations for the Lagrangian average of the tensor products $L_{ij}M_{ij}$ and $M_{ij}M_{ij}$ as \mathfrak{I}_{LM} and \mathfrak{I}_{MM} , respectively:

$$\frac{D\mathfrak{I}_{LM}}{Dt} \equiv \frac{\partial \mathfrak{I}_{LM}}{\partial t} + \bar{u}_i \cdot \nabla \mathfrak{I}_{LM} = \frac{1}{T} (L_{ij} M_{ij} - \mathfrak{I}_{LM}), \quad (2.19a)$$

$$\frac{D\mathfrak{I}_{MM}}{Dt} \equiv \frac{\partial \mathfrak{I}_{MM}}{\partial t} + \bar{u}_i \cdot \nabla \mathfrak{I}_{MM} = \frac{1}{T} (M_{ij} M_{ij} - \mathfrak{I}_{MM}) \quad (2.19b)$$

Here T is a time scale which represents the “memory” of the Lagrangian averaging. [Meneveau et al. \[1996\]](#) proposed the following time scale

$$T = \theta \Delta (\mathfrak{I}_{LM} \mathfrak{I}_{MM})^{(-1/8)} \quad (2.20)$$

This procedure for Lagrangian averaging has also been extended to the scale similar model by [Anderson and Meneveau \[1999\]](#) and the scale dependent dynamic model by [Stoll and Porte-Agel \[2006\]](#). Note that the time scale for Lagrangian averaging in equation (2.20) contains an adjustable parameter which is typically chosen to be $\theta = 1.5$. A dynamic eddy diffusivity model for the sub-grid density flux is defined as:

$$\lambda_j = -C_\rho \overline{\Delta}^2 |\bar{S}| \frac{\partial \bar{\rho}}{\partial x_j} \quad (2.21)$$

in a similar way, where $\kappa_{sgs} = C_\rho \overline{\Delta}^2 |\bar{S}|$ the constant C_ρ is evaluated dynamically as a function of time and space using both test filter and grid filter, Where C_ρ is defined as:

$$C_\rho = -\frac{1}{2} \frac{\langle \mathcal{L}_i \mathcal{M}_i \rangle}{\langle \mathcal{M}_k \mathcal{M}_k \rangle}, \quad (2.22)$$

with $\mathcal{M}_i = \widehat{\Delta}^2 |\widehat{S}| \widehat{\partial \bar{\rho}} / \widehat{\partial x_i} - \overline{\Delta}^2 |\overline{S}| \widehat{\partial \bar{\rho}} / \widehat{\partial x_i}$ and $\mathcal{L}_i = \widehat{\rho \bar{u}_i} - \widehat{\bar{\rho} \bar{u}_i}$ according to [Armenio and Piomelli \[2000\]](#). Moreover in case of instantaneous back scattering of energy from small scale to large scale the coefficients are set to zero. A detailed description of the model can be found at [Armenio and Sarkar \[2002\]](#).

We first explain the algorithm and techniques used to solve above equations. To this end, time advancement and space discretization of different terms are discussed in details. We present the numerical procedure by in a Cartesian geometry. At the end, we validate the method in case of unbounded domains with earlier numerical results by calculating first and second order statistics, as well as the Nu for range of $6.3 \times 10^8 \leq Ra \leq 10^8$ and find the good agreement between our results and reference.

2.3 Finite-difference code for simulating convection in Cartesian geometry

2.3.1 Computational procedure

We use the research code available at the Laboratory of Environmental and Industrial Fluid Mechanics of the University of Trieste, for simulating a RBC in three different geometries. It solves three dimensional, Navier-Stokes equations under Boussinesq approximation for buoyancy effects related to density variation. The code solves the curvilinear form of the governing equations (2.2)-(2.4), in particular using non-staggered grid mesh, where the pressure and Cartesian velocity components are defined at the center of the grid whereas the volume fluxes are defined at the mid point of their corresponding faces of the cell based on [Zang et al. \[1994\]](#) algorithm. For difficulties of complex geometries we use mapping or transformation from physical space (x, y, z) to a generalized curvilinear coordinate (ξ, η, ζ) space. The generalized coordinates implies that a distorted region in physical space is mapped onto a rectangular region in the generalized coordinate space as shown in figure (2.2) The governing equations are expressed in terms of the generalized coordinates as independent variables and the discretization is undertaken in the generalized coordinate space. Thus the computation is performed in this coordinate space, effectively as:

$$\frac{\partial u_i}{\partial x_j} = \frac{\partial u_i}{\partial \xi_k} \frac{\partial \xi_k}{\partial x_j} \quad (2.23)$$

$$\frac{\partial U_m}{\partial \xi_m} = 0 \quad (2.24)$$

$$\frac{\partial J^{-1} u_i}{\partial t} + \frac{\partial F_{im}}{\partial \xi_m} = J^{-1} B_i \quad (2.25)$$

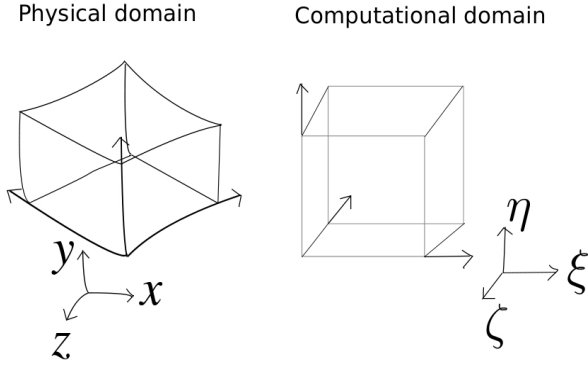


FIGURE 2.2: Coordinates transformation from the physical to the computational space

where also the gravitational term has been included in B and F_{im} is:

$$F_{im} = U_m u_i + J^{-1} \frac{\partial \xi_m}{\partial x_i} p - \nu G^{mn} \frac{\partial u_i}{\partial \xi_n} \quad (2.26)$$

where ξ_m , ($m = 1, 2, 3$) are the coordinates in transformed (rectangular and regular) computational space ($\xi = (x, y, z), \eta = (x, y, z), \zeta(x, y, z)$), with J^{-1} is the inverse of Jacobian or the volume of the cell; U_m is the product between the contravariant velocity and the inverse of the Jacobian and represents the volumetric flux normal to the surface $\xi_m = \text{constant}$. The transformed pressure term represents the flux of the pressure gradient through the faces of the cell in the physical domain, while the third term on the right hand side of equation (2.26) is the transformed diffusive term, which represents the fluxes of the viscous stresses through the cell faces of the cell. The term G^{mn} is called the “mesh skewness tensor”. The quantities in equation (2.23)-(2.25) are:

$$U_m = J^{-1} \frac{\partial \xi_m}{\partial x_j} u_j \quad (2.27)$$

$$J^{-1} = \det\left(\frac{\partial x_i}{\partial \xi_j}\right) \quad (2.28)$$

$$G^{mn} = J^{-1} \frac{\partial \xi_m}{\partial x_j} \frac{\partial \xi_n}{\partial x_j} \quad (2.29)$$

Therefore the equation for the advection and diffusion of a scalar can be written as:

$$\frac{\partial J^{-1} C}{\partial t} + \frac{\partial U_m C}{\partial \xi_m} = \frac{\partial}{\partial \xi_m} (k G^{mn} \frac{\partial C}{\partial \xi_n}) \quad (2.30)$$

where in our study C is density.

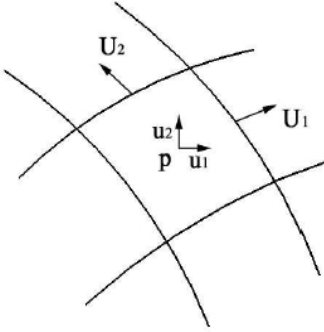


FIGURE 2.3: Distribution of velocities (Cartesian and contravariant) for a two dimensional case in a computational cell.

2.3.2 Discretization

The equations (2.23)-(2.25) are solved following the fractional step formulation of Zang et al. [1994]. Second order central finite differences are used for the spatial discretization in the computational space ξ, η, ζ where as the time integration is carried out using the second order accurate Adams-Bashforth scheme for the convective terms and the implicit Crank-Nicolson scheme for the diagonal viscous terms. Therefore the discretized equations become:

Continuity equation:

$$\frac{\partial U_m}{\partial \xi_m} = 0, \quad (2.31)$$

and momentum equation:

$$J^{-1} \frac{u_i^{n+1} - u_i^n}{\Delta t} = \frac{3}{2}(C(u_i^n) + D_E(u_i^n) + B_i^n) - \frac{1}{2}(C(u_i^{n-1}) + D_E(u_i^{n-1}) + B_i^{n-1}) + R_i(p^n + 1) + \frac{1}{2}(D_I(u_i^{n+1}) + D_I(u_i^n)) \quad (2.32)$$

where $\delta/\delta\xi_m$ represents discrete finite difference operators in the computational space; superscripts represent the time step; C represents the convective term; R_i is the discrete operator for the pressure gradient terms; and D_E and D_I are discrete operators respectively representing respectively the off-diagonal viscous terms (treated explicitly) and the diagonal viscous terms (treated implicitly).

Following Zang et al. [1994], The model solves numerically the above equations by applying the fractional step method which, for each iteration, is split into two steps. In the first step known as *predictor* step, an intermediate velocity is computed. In the second step, known as *corrector* the pressure is used to project the intermediate the velocity onto a space of divergence free velocity field to get the next update of velocity and pressure.

The latter is called the projection step and schemes that use this approach are often called projection methods. The projection method requires the solution of the Poisson equation for the pressure term which appears only in the momentum equation in form of a partial derivative of first order, $R_i(P^{n+1})$. The algorithm involves the computation of the partial derivative such that it yields a divergence of flow field. Therefore an adequate iterative method solves the Poisson equation iteratively until the conservation of mass and momentum is obtained.

2.3.3 Multi-step (predictor-corrector) methods

The *predictor* step is concerned with the time advancement of the advective and diffusive transport of momentum, written as:

1. Predictor

$$\left(I - \frac{\Delta t}{2J^{-1}} D_1 \right) (u_i^* - u_i^n) = \frac{\Delta t}{J^{-1}} \left[\frac{3}{2} (C(u_i^n) + D_E(u_i^n) + B_i^n) - \frac{1}{2} (C(u_i^{n-1}) + D_E(u_i^{n-1}) + B_i^{n-1} - D_I(u_i^n)) \right] \quad (2.33)$$

2. Corrector

$$u_i^{n+1} - u_i^* = \frac{\Delta t}{J^{-1}} [R_i(\psi^{n+1})], \quad (2.34)$$

where I is the identity matrix and variable ϕ is related to pressure p by:

$$R_i(p) = \left(J^{-1} - \frac{\Delta t}{2} D_I \right) \left(\frac{R_i(\phi)}{J^{-1}} \right) \quad (2.35)$$

To invert the matrix on the LHS of equation (2.33) we apply an approximate factorization technique, in which (2.33) is written as:

$$\begin{aligned} & \left(I - \frac{\Delta t}{2J^{-1}} D_1 \right) \left(I - \frac{\Delta t}{2J^{-1}} D_2 \right) \left(I - \frac{\Delta t}{2J^{-1}} D_3 \right) (u_i^* - u_i^n) \\ &= \frac{\Delta t}{J^{-1}} \left[\frac{3}{2} (C_i^n + D_E(u_i^n)) - \frac{1}{2} (C_i^{n-1} + D_E(u_i^{n-1})) + D_I(u_i^n) \right], \end{aligned} \quad (2.36)$$

where

$$D_k = \frac{\partial}{\partial \xi_k} \left(\nu G^{kk} \frac{\partial}{\partial \xi_k} \right), \quad k = 1, 2, 3. \quad (2.37)$$

2.3.4 Solution of pressure Poisson equation

The variable ϕ^{n+1} is obtained by solving the pressure Poisson equation derived by the following procedure. Following Zang et al. [1994], first we derive the equation for the volume flux U_m^{n+1} . If we imagine that we apply the corrector step of the fractional step method (2.34) to the Cartesian velocity components defined on a certain face of the control volume, we have:

$$(u_i^{n+1})_{face} = (u_i^*)_{face} - \Delta t \left(\frac{\delta \xi_m}{\delta x_i} \frac{\delta \phi^{n+1}}{\delta \xi_m} \right)_{face}. \quad (2.38)$$

Combining above equation with volume flux U_m , one obtains

$$U_m^{n+1} = U_m^* - \Delta t \left(G^{mn} \frac{\delta \phi^{n+1}}{\delta \xi_n} \right), \quad (2.39)$$

where $U_m^{n+1} = J^{-1}(\delta \xi_m / \delta x_j) u_j^*$ is called the intermediate volume flux. Since the intermediate velocity u_j^* is defined at the cell center, while the fluxes U_m^* and U_m^{n+1} are defined on the cell faces, u_j^* has to be interpolated into the cell faces in order to compute U_m^* . By substituting above in to equation (2.31), we can obtain the pressure Poisson equation for ϕ^{n+1} as:

$$\frac{\delta}{\delta \xi_m} \left(G^{mn} \frac{\delta \phi^{n+1}}{\delta \xi_n} \right) = \frac{1}{\Delta t} \frac{\delta U_m^*}{\delta \xi_m} \quad (2.40)$$

The Poisson equation is solved using SLOR iterative technique with unstructured multigrid method in order to accelerate the convergence of iterative solvers. The fast convergence rate of the multigrid method enables the convergence of the Poisson equation to machine zero, satisfying the mass conservation.

In the following we describe briefly the solution procedure:

1. Solve for the intermediate velocity u_i^* at the cell centers using equation (2.36)
2. Interpolate u_i^* onto the cell faces and compute the RHS of equation (2.40)
3. Solve equation (2.40) by the (structured/unstructured) multigrid method to obtain a converged ϕ^{n+1}
4. Obtain u_i^{n+1} from equation (2.34) and U_m^{n+1} from equation (2.39) to finish one time step.

After this procedure the flow quantities at time step $n + 1$ is obtained and the next temporal step advanced. Since the diagonal diffusive terms are resolved by using the Crank-Nicholson method for the implicit terms, the viscous stability limit for the time step is removed. Therefore, the stability of the overall numerical method is limited by

the Courant-Friedrichs-Lowy (CFL) condition. The local CFL number is defined as:

$$\begin{aligned} CFL &= \left(\frac{|u_1|}{\Delta x} + \frac{|u_2|}{\Delta y} + \frac{|u_3|}{\Delta z} \right) \Delta t \\ &= (|U_1| + |U_2| + |U_3|) \frac{\Delta t}{J^{-1}}, \end{aligned} \quad (2.41)$$

where $\Delta x, \Delta y, \Delta z$ are the grid spacing of the three Cartesian coordinates. In the above fractional step, the stability condition requires that the maximum value obtained from (2.41) in the computational domain is:

$$CFL_{max} < \bar{C} \sim 1,$$

where CFL_{max} is the maximum value obtained from equation (2.41). The \bar{C} is a function of Reynolds number and as mentioned by [Zang et al. \[1994\]](#) it may become smaller than one for highly skewed grid mesh. In the present code, we use multiprocessors system in z direction, where y is upward direction against gravity. We note that the time step is not reported in all simulations of this thesis because it is adaptive, which means that it is periodically updated to fulfil the minimum CFL condition. The constant Courant number is set to 0.6 in all simulations.

Chapter 3

Rayleigh-Bénard convection with periodic walls

In this chapter we present numerical results on Rayleigh-Bénard convection in a periodic domain. In the first part we validate results of LES and DNS against earlier numerical simulations, in which flow is periodic in horizontal directions. Then we examine Lagrangian ensemble approaches before applying them to a complex-bounded domain. We find that the Lagrangian approach reproduces data more accurately than the planar-averaged formulation commonly used in numerical simulations.

3.1 Simulation details and boundary conditions

We validate our numerical code with the earlier results of [Kimmel and Domaradzki \[2000\]](#)-henceforth KD00- by calculating the Nusselt numbers and first and second order statistics for 3D simulations in the periodic rectangular box $\Gamma = 6$.

As mentioned before, simulation methodologies can generally be classified, based on the level of representation of the physics and the accuracy into Reynold-Averaged Navier-Stokes (RANS), Large Eddy Simulation (LES) and Direct Numerical Simulation(DNS). In order to validate our numerical method, all simulation parameters are the same as KD00. DNS and LES with static and dynamic Pr_{sgs} were performed in a three-dimensional rectangular domain with periodic boundary conditions on the side walls (x, z). The code is based on finite difference and has the equations (2.31)-(2.32) discretized and implemented on a non-staggered grid. Central differences are used for the spacial derivatives and time integration is by a second order Adams-Bashforth scheme. The code is fully parallelized and supports grid clustering in horizontal direction z . Further details of the code can be found elsewhere [[Roman et al., 2009, 2010](#), [Petronio et al., 2013](#)].

Resolving all the length-scales makes DNS a powerful research tool, as one has the complete four-dimensional solution of the Navier-Stokes equations at hand, but it is limited to relatively low Re as the computational demands quickly become prohibitive, scaling approximately as Re^3 . Furthermore, both the thermal λ_θ and kinematic λ_u boundary layer, should be fully resolved as under sampling will lead to overestimation of Nu [[Kerr, 1996](#)]. Therefore in addition to DNS we also have pursued LES methodologies, partly in order to have the lower cost of simulation for higher Ra numbers within complex/bounded geometries.

Simulations have been performed at $Pr = 1$ and $Ra = 6.3 \times 10^5, 2.5 \times 10^6, 10^7, 10^8$ for an aspect ratio $\Gamma = 6$. At the top and bottom plate we use no-slip velocity boundary conditions (BC) and in horizontal directions, x and z , periodicity BC is applied,

$$y = 0 : \rho = 0, \mathbf{v} = 0; \quad y = 1 : \rho = 1, \mathbf{v} = 0, \quad (3.1)$$

$$\begin{aligned} \mathbf{u}(x + dx, z) &= \mathbf{u}(x, z), & \rho(x + dx, z) &= \rho(x, z), \\ \mathbf{u}(x, z + dz) &= \mathbf{u}(x, z), & \rho(x, z + dz) &= \rho(x, z), \end{aligned} \quad (3.2)$$

so that the unstable density gradient $\Delta\rho/\rho_0 = 1$ is applied in the wall-normal direction. Moreover for the sake of simplicity the pressure gradient is considered to be zero in all directions in our study ($\partial P/\partial x_i = 0$).

Since there is a density gradient between top and bottom plate, the gravitational field

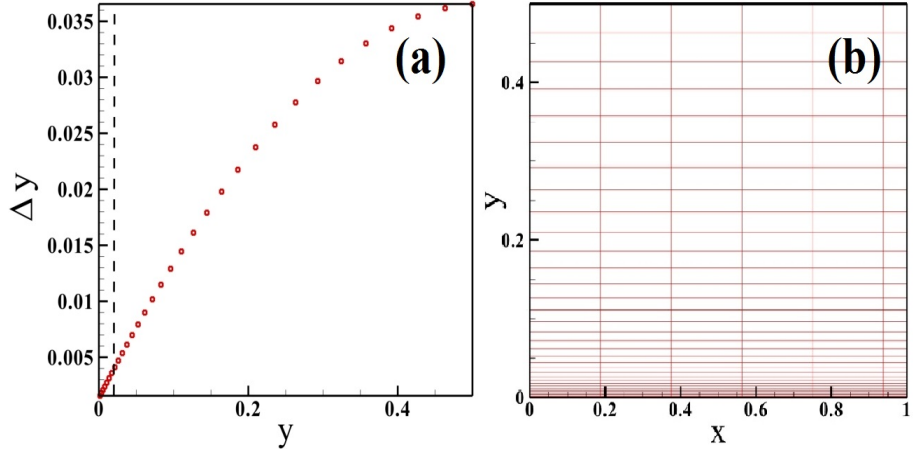


FIGURE 3.1: (a) Grid spacing in the vertical direction of the domain stretched by hyperbolic tangent function, dash line is mean thermal boundary layer thickness at $Ra = 10^8$ and (b) its zoom grid mesh design in $x - y$ plane

leads to buoyant forces which act to pull down denser and cooler fluid from the top plate to the bottom one and vice versa. This force due to gravitational acceleration ($g = 9.81 \text{ m/s}^2$) is opposed by the viscous damping and thermal dissipation in the fluid and their interplay is expressed in the Rayleigh number Ra , as explained earlier.

Due to the presence of both thermal and velocity boundary layers near the solid heated bounding plates (top and bottom), we design a non-uniform grid mesh in the wall-normal direction (see figure (3.1-b)) and uniform in horizontal directions. In order to resolve boundary layers properly, the grid spacing is sufficiently finer close to the top and bottom walls. We use a hyperbolic tangent function to create stretching in all directions [Vinokur \[1980\]](#) if needed as can be seen from figure (3.1-a). We follow the prescription given by [Verzicco and Camussi \[2003\]](#) concerning the number of grid points needed in the thermal boundary layer in order to have a fully developed simulation.

Parameters for low Ra with constant Pr_{sgs} (meaning that sub-grid scale eddy viscosity is computed dynamically in the equations) are listed in table (3.1) in which dynamic model (DSM) averaged parameters over the homogeneous $x - z$ directions.

In numerical simulations, a good initial guess of the field helps in optimizing the simulation time for both the instability and the turbulence calculations. The patterns and instabilities near the onset depend critically on the initial conditions. Furthermore, to save computational time, the turbulent state is reached by performing the numerical experiment in several steps. For example, a simulation may be first performed on a coarse grid mesh ($32 \times 64 \times 32$) and then the output of this run can be interpolated to further runs using a finer grid ($128 \times 64 \times 128$). Our simulations for $6.3 \times 10^6 \leq Ra \leq 10^8$ with coarse (L0) and finer grids (L1-L4), and applying the Lagrangian Dynamic Smagorinsky method (LDS), whose both sub-grid scale fluxes of momentum and heat were parametrized dynamically in the system, show better results compared to standard dynamic models

| Case | Model | Ra | $N_x \times N_y \times N_z$ | N_θ | Pr_{sgs} | Nu |
|------|-------|-------------------|-----------------------------|------------|------------|-------|
| DNS | DNS | 6.3×10^5 | $128 \times 64 \times 128$ | 5 | — | 6.80 |
| D1a | LES | 6.3×10^5 | $32 \times 64 \times 32$ | 13 | 0.4 | 8.52 |
| D1b | LES | 6.3×10^5 | $32 \times 64 \times 32$ | 13 | 0.8 | 7.56 |
| D1c | LES | 6.3×10^5 | $32 \times 64 \times 32$ | 13 | 1.0 | 6.91 |
| D1d | LES | 6.3×10^5 | $32 \times 64 \times 32$ | 13 | 1.4 | 6.19 |
| D2 | LES | 2.5×10^6 | $128 \times 64 \times 128$ | 10 | 0.4 | 12.63 |
| D3 | LES | 1.0×10^7 | $128 \times 64 \times 128$ | 10 | 0.4 | 17.45 |
| D4 | LES | 1.0×10^8 | $128 \times 64 \times 128$ | 5 | 0.4 | 33.84 |

TABLE 3.1: Simulation parameters for $Pr = 1$, $\Gamma = 6$ for Direct Numerical Simulation (DNS) and Large Eddy Simulations (D1-D4) with plane averaging over horizontal plates . The number of grid points required $N_x \times N_y \times N_z$ in i -direction $N_i(i = x, y, z)$; N_θ is number of grid points required for resolving the thermal BL; Pr_{sgs} is the sub-grid Prandtl number and Nu is computed Nusselt number.

| Case | Model | Ra | $N_x \times N_y \times N_z$ | N_θ | Nu |
|------|-------|-------------------|-----------------------------|------------|-------|
| L0 | LES | 6.3×10^5 | $32 \times 64 \times 32$ | 13 | 6.85 |
| L1 | LES | 6.3×10^5 | $128 \times 64 \times 128$ | 13 | 7.08 |
| L2 | LES | 2.5×10^6 | $128 \times 64 \times 128$ | 10 | 10.59 |
| L3 | LES | 1.0×10^7 | $128 \times 64 \times 128$ | 10 | 16.09 |
| L4 | LES | 1.0×10^8 | $128 \times 64 \times 128$ | 5 | 31.16 |

TABLE 3.2: Simulation parameters for $Pr = 1$, $\Gamma = 6$ with Lagrangian Dynamic model. The number of grid points $N_x \times N_y \times N_z$ in i -direction $N_i(i = x, y, z)$; Nu_θ number of grid points required in the thermal boundary layer; Nu is the Nusselt number computed on walls.

(DSM). The parameters for LDS are listed in table (3.2).

In the next part we will present and compare the results obtained from our numerical simulation.

3.2 Results

3.2.1 Mean and turbulent quantities

A first statistical approach to the study of turbulent Rayleigh-Bénard convection is the analysis of one point statistics. The simplest statistical properties are the mean, or first moment, and the variance , or second moment, which allow a rough characterization of the flow. We start by the introducing the decomposition of the velocity $u_i(x, y, z, t)$ and

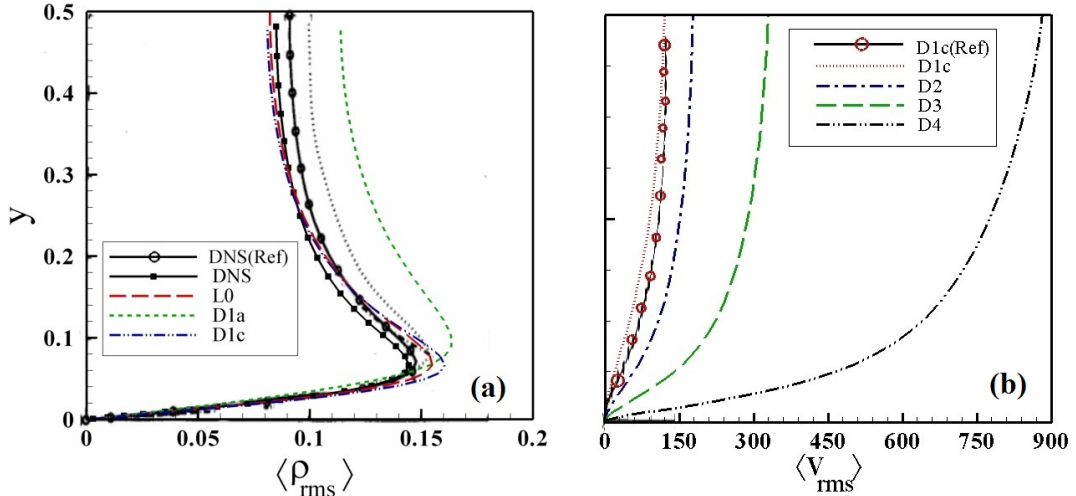


FIGURE 3.2: Turbulence statistics in global units for different Ra numbers and dynamic approaches as a function of vertical height. (a) resolved root mean square density fluctuations $\rho_{rms}/\Delta\rho$ and (b) resolved root mean square of vertical velocity fluctuations normalized by ν/H . The results are compared with KD00. The curves are labelled as tables 3.1 and 3.2

the density $\rho(x, y, z, t)$ fields into mean components – $\langle u_i(x, y, z, t) \rangle$ and $\langle \rho(x, y, z, t) \rangle$ respectively– and fluctuations. Subsequent simulations are validated against KD00 as listed in tables (3.1) and (3.2). Thermal gradients are the driving factor of Rayleigh-Bénard convection; therefore a good starting point for providing a topological characterization of the flow is to analyse one-point statistics of a temperature field.

Figure (3.2) presents some results using the homogeneous plane-averaged Dynamic Smagorinsky (DSM) method, the Lagrangian dynamic approach (L0) and DNS. In order to be able to draw comparisons with KD00 quantities are non-dimentionalized using combinations of H and ν . The second order statistic of rms density fluctuations ρ_{rms} in the case of the LDS compares well with KD00 (DNS). Figure (3.2)-(a) shows the rms of resolved density fluctuations of our DSM with $Pr_{sgs} = 0.4$ and $Pr_{sgs} = 1$. As explained before, in LES, the filtering procedure removes the SGS contribution from the total turbulent fluctuating flow field defined as $X' = \bar{X}_i - \langle X_i \rangle$ where $\langle .. \rangle$ denotes averaging over time and horizontal plane(s). Therefore the total fluctuations is the contribution from the resolved part and the SGS part; in general, the total fluctuations is the sum of *resolved* parts and *sgs* parts ($X'(x_i, t) = X'_{res}(x_i, t) + X'_{sgs}(x_i, t)$). In our study here we present the resolved parts of all quantities, noting that the *sgs* part is very small and does not have significant influence. We compute the root-mean-square fluctuations of density (σ_ρ) and velocity (σ_v) as

$$\rho_{rms} = \sigma_\rho(\mathbf{x}) = [\langle \rho(\mathbf{x})\rho(\mathbf{x}) \rangle_t - \langle \rho(\mathbf{x}) \rangle_t \langle \rho(\mathbf{x}) \rangle_t]^{1/2} \quad (3.3)$$

$$v_{rms} = \sigma_v(\mathbf{x}) = [\langle v(\mathbf{x})v(\mathbf{x}) \rangle_t - \langle v(\mathbf{x}) \rangle_t \langle v(\mathbf{x}) \rangle_t]^{1/2}, \quad (3.4)$$

normalized by $\Delta\rho$ and ν/H . In figures (3.2)-(a) and (3.3)-(b) the highest values of ρ_{rms} occur near the walls where thermal plumes erupt from the boundary. The profile obtained is very similar to that found by Kerr [1996]. It is interesting to note that the maximum value of the density fluctuations is found to be close to the bottom and top walls, as in the case of rotating Rayleigh-Bénard convection (and decreases with increasing Rossby number Ro —see the discussion in Kunnen et al. [2009]).

By recalling the Nusselt number defined in chapter 1, we can state that the heat transport is mostly conductive close to the walls and mostly convective in the core region. The conductive layer, made of quiescent fluid, it is called the *thermal boundary layer* (λ_θ). This region is defined in terms of its thickness as:

$$\lambda_\theta = \frac{H}{2Nu} = -\frac{\Delta\rho}{2} \frac{d\langle\rho\rangle}{dy} |_{wall}, \quad (3.5)$$

and is distance from the horizontal walls supporting the majority of the temperature difference. The peak distance of the root mean square (rms) density from the horizontal plates is another definition of the thermal boundary layer thickness, hereafter referred to as λ_θ^{rms} .

Within the thermal boundary layer our dynamic model compares well to KD00 but under-predicts in the convection core. The Smagorinsky model with $Pr_{sgs} = 0.4$ is found to significantly over-predict the DNS results in the peak region and in the convection core, but the Lagrangian approach (L0) gives reasonable agreement with the DNS method and dynamic model with sub-grid Prandtl number 1. KD00 did not observe significant differences between $Pr_{sgs} = 0.4$ and $Pr_{sgs} = 1$. We find that by setting a turbulent Prandtl number to either 1 or 0.4 makes a significant difference, with the value 1 giving better results. For the rms vertical velocity our dynamic model with $Pr_{sgs} = 1$ gives very good agreement with KD00. We clearly see that the vertical velocity fluctuations increases as a function of Ra with constant $Pr_{sgs} = 0.4$. Over all our code gives better agreement with DNS (KD00) by using a dynamic Pr_{sgs} (we mean that both ν_{sgs} and κ_{sgs} computed dynamically as a function of time and space) rather than keep it as a constant ratio $\kappa_{sgs} = \nu_{sgs}/Pr_{sgs}$.

Figure (3.3) shows mean and r.m.s density fluctuations by means of a Lagrangian approach. A comparison between (3.3)-(a) and (b) clearly indicates that the average λ_θ^{rms} is nearly equal to the average λ_θ . We have separated the thermal boundary layer from the core by defining its thickness, and computing it by equation (3.5). Nevertheless it is still not clear what mechanisms regulate the characteristic dimensions of this layer (detailed studies of the thermal boundary layer and its features will not be addressed in the present work).

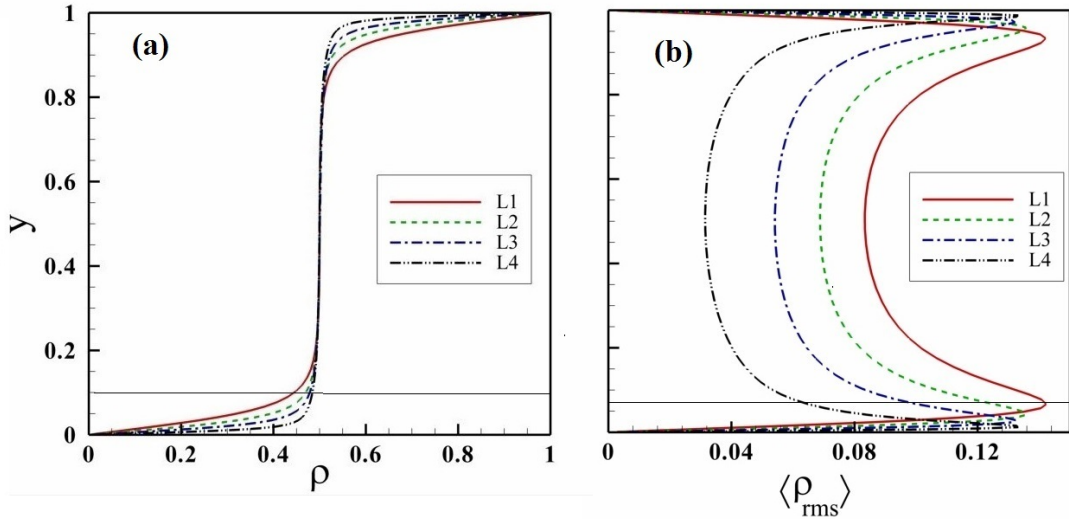


FIGURE 3.3: (a) The mean density $\langle \rho \rangle$ and (b) resolved density fluctuations ρ_{rms} as a function of y for $Ra = 6.3 \times 10^5$ (solid line), $Ra = 2.5 \times 10^6$ (dashed line), $Ra = 10^7$ (dash dot), $Ra = 10^8$ (dash dot dot) obtained by LDS method.

The presence of large-scale structures of the velocity field, which develop both for confined and unconfined (i.e for periodic side wall boundary conditions) domains, generates viscous boundary layers just below the top and just above the bottom plate. The thickness of viscous boundary layer strictly depends on fluid properties. When molecular $Pr = 1$ the thickness of the thermal BL is equal to that of the viscous BL. The viscous boundary layer thickness λ_u is commonly defined as the peak position of u_{rms} or w_{rms} , the r.m.s horizontal components of velocity. As can be seen in figure (3.4), λ_u shows a clear dependence on the Ra number. This result agrees with GL theory [Grossmann and Lohse, 2004] in which a viscous Blasius-type boundary layer is assumed, with a thickness

$$\lambda_u \sim \frac{H}{Re}, \quad (3.6)$$

where the characteristic velocity contained within the Reynolds number is the *rms* horizontal velocity. By recalling equation (3.5) one can obtain the ratio of λ_u to λ_θ predicted by GL theory

$$\frac{\lambda_u}{\lambda_\theta} \sim \frac{Nu}{2\sqrt{Re}} \quad (3.7)$$

Figure (3.4) shows rms horizontal velocity as a function of Ra numbers. This result illustrates the difference between the two dynamic models: at higher Ra , LDS has greater variation compared to DSM and consequently the actual sub-grid density flux λ_j^{SGS} can be different for fixed, constant values of this ratio.

As explained in the first chapter, spatial filtering/averaging introduces Subgrid-scale (SGS) stresses τ_{ij}^{sgs} and scalar fluxes q_i^{sgs} in the equations for the resolved quantities used

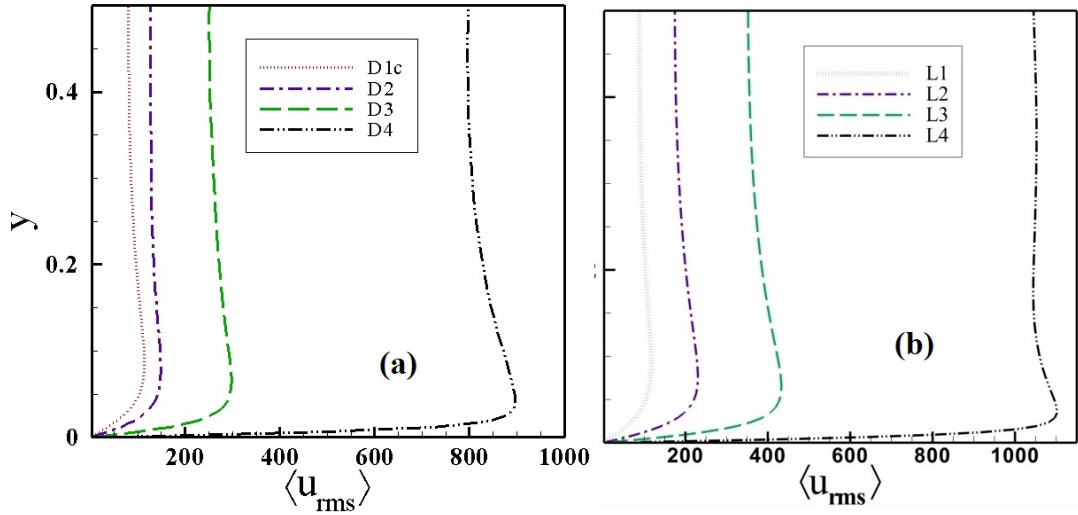


FIGURE 3.4: Resolved horizontal velocity fluctuations as a function of Ra computed by (a) DSM and, (b)(LDS) as a function of y for $Ra = 6.3 \times 10^5$ (dotted), $Ra = 2.5 \times 10^6$ (dashed dot line), $Ra = 10^7$ (dash line), $Ra = 10^8$ (dash dot dot line)

in LES, representing the effect of the unresolved, small scale turbulence on the resolved filtered motion. In the eddy viscosity SGS model it has been recognized that the dynamic approach may, in general, improve predictions as compared with a base model in which the model coefficient is set to be constant. This approach dynamically determines the model coefficient as a function of time and space in terms of the smallest resolved scales. Additionally, the dynamic approach helps to relax the *sharp* requirement imposed on the adjustment of large scales as in an eddy viscosity based SGS model that uses constant model coefficients to represent the interaction between the resolved scales and SGSs.

3.2.2 Heat flux

As mentioned previously, one goal of the study of turbulent Rayleigh-Bénard convection is to understand how heat is transported across the fluid layer. One of the key questions in our study is how the Nusselt number, Nu , depends on both Ra and cross-sectional geometry (the dependence of aspect ratio and Pr is not considered here). In particular, in the next two chapters we study local distribution of heat flux over enclosed smooth and non-smooth surfaces with bounding, adiabatic vertical walls. Following GL theory the global heat flux can be considered as the sum of plume and turbulent background contributions. In local measurements of the vertical velocity and density gradient it is possible to disentangle plume and turbulent background contribution within simulations; for example, in the paper by Ching et al. [2004], an algorithm is proposed to detect

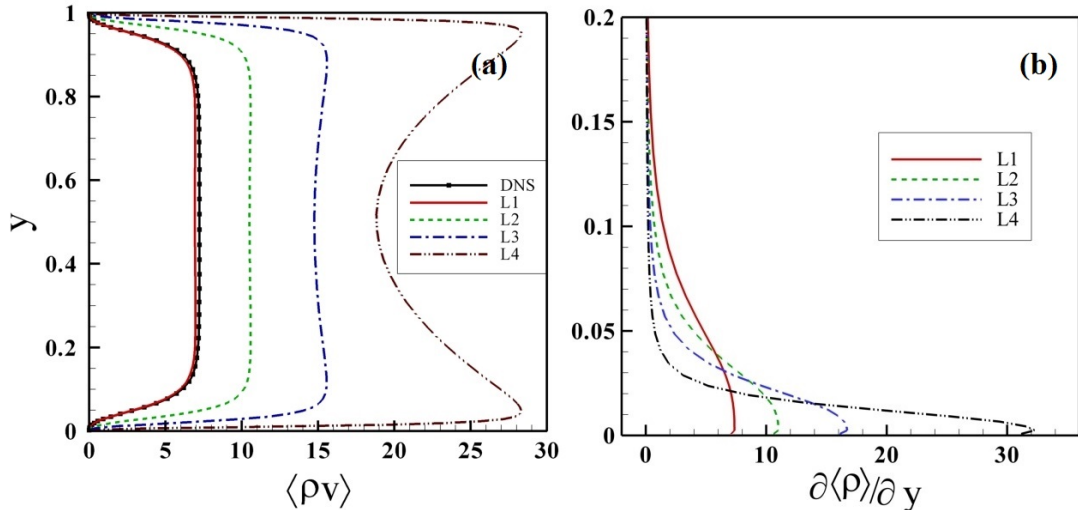


FIGURE 3.5: Comparison of components of the Nusselt number computed using LDS as a function of Ra (a) resolved vertical density flux and (b) resolved density gradient along vertical direction

plumes in time series of the vertical velocity and density.

We compute global Nu number by equation (1.22) which consists of a diffusive contribution only. Figure (3.5)-(b) compares the density gradient along y direction as a function of Ra . Conductive heat transfer has its maximum value close to the wall and goes to zero away from the wall. In contrast the convective contribution to the heat flux has zero value on the walls because of the no-slip condition imposed. KD00 computed total Nusselt number in an LES model by adding a third term $\langle \tau_{\theta 2} \rangle / \kappa \Delta T H^{-1}$ which is the contribution to the heat flux from the subgrid-scales. They found that even though this term is much smaller than the other two terms it is still significant. In the range of Ra from 6.3×10^5 to 1×10^7 they found $Nu = 0.21 Ra^{0.28}$. We found scaling of $Nu(Ra)$ is $Nu = 0.142 Ra^{0.293}$ in the same range with LDS results.

Fig (3.5)-(a) shows the resolved turbulent density fluxes as a function of Ra number for case LDS. The variation of turbulent density flux is maximum within the thermal boundary layer and it is almost constant within the core region. It means the correlation between density fluctuations and velocity is maximum within the thermal boundary layer, where there is the maximum probability of finding a plume.

3.2.3 Turbulent diffusivity

Turbulence schemes in numerical models make use of a turbulent Prandtl number $Pr_t = \nu_t / \kappa_t$ to link the vertical momentum and scalar fluxes, where ν_t and κ_t are the momentum and scalar diffusivities respectively [Armenio and Sarkar \[2002\]](#). For multi-directional shear flows κ_t and ν_t are defined using the gradient transport hypothesis. We compute

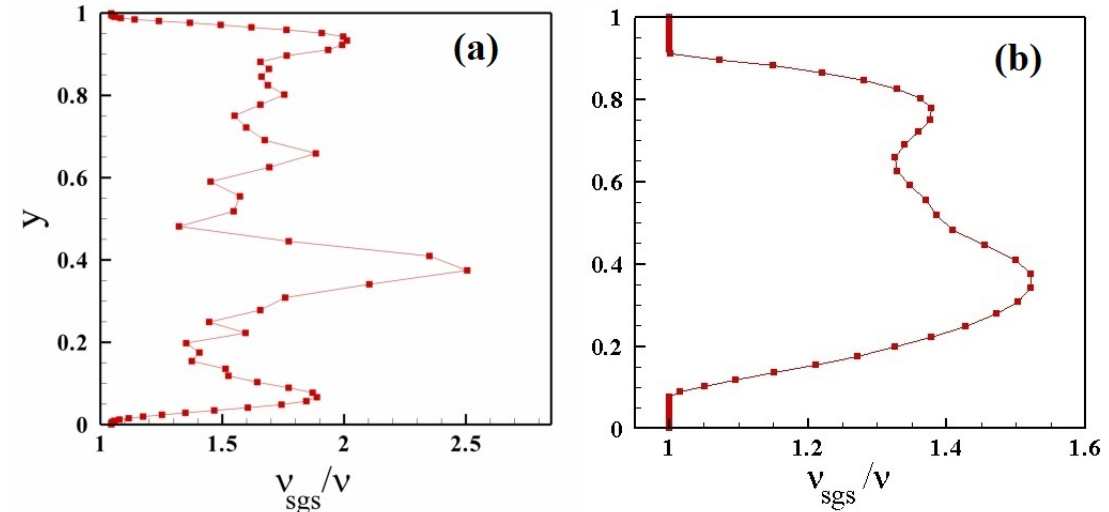


FIGURE 3.6: Instantaneous eddy viscosity $\langle \nu \rangle_A / \nu$ at (a) $Ra = 10^8$ and (b) $Ra = 6.3 \times 10^5$.

total turbulent Prandtl Number Pr_t with consideration of its sgs part. In Lagrangian averaging we compute dynamically both sub-grid eddy diffusivities of momentum and buoyancy, $\langle \nu_{sgs} \rangle$ and $\langle \kappa_{sgs} \rangle$ respectively, in which the sub-grid Prandtl number is defined as $Pr_{sgs} = \nu_{sgs} / \kappa_{sgs}$. We compute the resolved part of momentum and density fluxes as:

$$\nu_{res} = \frac{\sqrt{\langle u'v' \rangle^2 + \langle w'v' \rangle^2}}{\sqrt{(\frac{\partial \langle u \rangle}{\partial y})^2 + (\frac{\partial \langle w \rangle}{\partial y})^2}} \quad (3.8)$$

$$\kappa_{res} = \frac{\langle \rho'v' \rangle}{\frac{\partial \langle \rho \rangle}{\partial y}}. \quad (3.9)$$

Therefore the total value can be defined as:

$$Pr_t = \frac{\nu_{res} + \nu_{sgs}}{\kappa_{res} + \kappa_{sgs}} \quad (3.10)$$

Reynolds [1975] examined more than 30 different ways of predicting the turbulent Prandtl number, ranging from empirical to formal analyses, the latter based on the Reynolds stress equation. The formal analyses are available only for the case of weak decaying turbulence. The empirical formulations vary from those containing several adjustable constants such as the position within the flow, to the simplest expression of the turbulent Prandtl number as a function of the molecular one only, e.g the formula due to Graber Gräber [1970]:

$$Pr_t^{-1} = 0.91 + 0.13 Pr^{0.545}; \quad 0.7 < Pr < 100.$$

Graber's formula is valid for a specific range of Pr and it gives a constant value of Pr_t for the flow under investigation. There is a need to extend the range and study the local distribution of Pr_t . The turbulent Prandtl number is an extremely difficult quantity to measure experimentally. The alternative approach is to deduce its value from experimental measurements of bulk quantities, such as Nusselt number, which are more easily measured.

Another model of predicting Pr_t uses the Reynolds analogy. The main assumption is that heat flux in a turbulent system is analogous to momentum flux, which suggests that its ratio must be constant for all horizontal positions. In the recent years there are numerous studies based on Pr_t for different types of flow. For example, data from numerical simulations and experiments suggest values of Pr_t in the range of 0.5 – 1.0 for neutrally stratified flow ([Kays \[1994\]](#))

In the case of horizontal homogeneity(s) we have calculated Pr_{sgs} directly by post processing data of our simulations and show its vertical profile as a function of Ra in figure [\(3.7\)](#). We observed that the variation of Pr_{sgs} with respect to Ra number has its maximum value very close to the wall and then decreases. The interval of the variation is from 0.8 to 1.1 in this case. For $y/H < 0.2$ the values of sgs Prandtl number increase and decrease rapidly. In this region the energy dissipation is much greater than in convective layer above and where the eddy structure is dominated by shear rather than being convectively driven. From a mathematical point of view, sub-grid fluctuations are able to transport momentum more efficiently than heat. In the convective core $y/H > 0.2$ the behavior of the dynamic eddy viscosity and thermal diffusivity (ν_{sgs}/κ_{sgs}) is constant for all Ra number. Although both dynamic eddy viscosity and thermal diffusivity are varying independently along y , the ratio $Pr_{sgs} = \nu_{sgs}/\kappa_{sgs}$ is almost constant ($Pr_{sgs} \sim 1$ is observed here). Our studies show that dynamical computation of Pr_{sgs} gives better results than the utilization of the Reynolds analogy, in which the value to Pr_{sgs} must kept constant for all positions.

Figure [3.6](#) shows instantaneous eddy viscosity normalized by the molecular one for DSM case ν_{sgs} is zero close to the walls, although it increases to positive values closer to the core region. As discussed before, the reason for this behaviour is that the dynamic coefficient C_s is set to zero in the code if negative eddy viscosity occurs momentarily and thus is not indicative of the time-averaged values which reflect the correct flow properties.

3.2.4 Flow field

In order to identify specific flow regions and characteristic structures, a preliminary approach to the study of turbulent Rayleigh-Bénard convection consists of analyzing the temperature and velocity fields obtained by DNS and LES. Figures [\(3.8\)](#) and [\(3.9\)](#) show

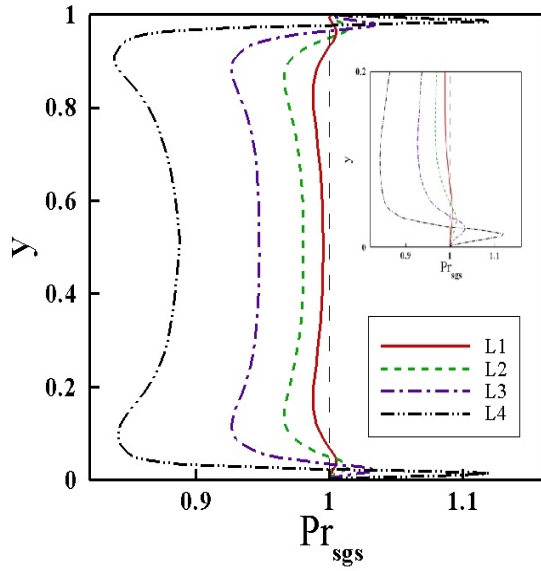


FIGURE 3.7: Profiles of the subgrid Prandtl number as a function of Ra along vertical direction. The insert figure shows close-up near the boundary layer.

instantaneous velocity fields (arrows) superimposed on the instantaneous surface density field (colour-coded area) for different Ra numbers. As can be seen in the vertical xy -slices plotted in figure (3.8), a recurrent coherent structure is observed, consisting of a localized portion of fluid having a density (temperature) contrast with the background. This structure—called a *thermal plume*—plays a fundamental role in turbulent convection as it carries a large fraction of the heat into the core of fluid layer.

Hot and cold plumes detach respectively from the bottom and upper plate, moving toward the core of the cell driven by buoyancy forces, which are triggered by a density contrast with the ambient. Considering only the lower half of the volume, as heated fluid rises, it pushes aside the cooler fluid above it. As can be clearly seen in the vertical slices, the rising fluid produces a stalk, while the deflected fluid produces a cap on top. As the pushing and deflection continue, the edge of the cap may further fold over, creating mushroom-like structure Zhou and Xia [2010]. The same behavior affects cooled descending plumes.

Many studies (Zhou et al. [2007], Sun and Xia [2005], Huang et al. [2013]) have shown two different morphologies for the plume: the *sheet-like plume*, which is observed close to the walls, and *mushroom-like plume* which is observed in the core.

Figure 3.8 (a) shows a 3D view of the instantaneous density field close to the top and bottom walls at $Ra = 1 \times 10^7$. A fine network of thin plumes is visible. The sheet-like structures are formed by impingement of cold plumes onto the bottom plate, as the hot fluid in the boundary layer is pushed away. As expected, sheet-like plumes become thinner as the Ra increases due to the smaller thermal diffusivity. As expected, the

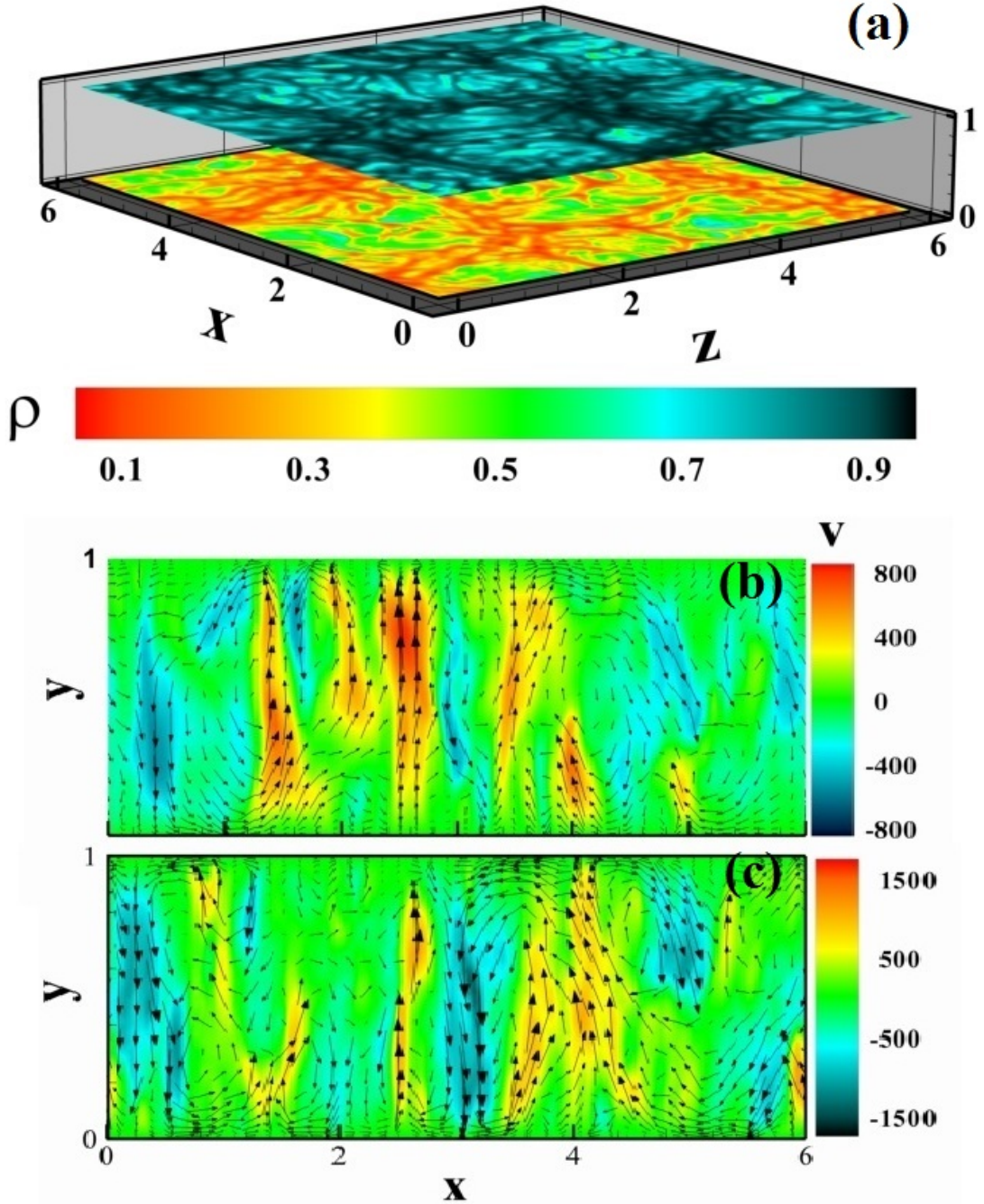


FIGURE 3.8: (a) 3D view of local instantaneous density $\rho/\Delta\rho_0$ distribution over top and bottom plate at $Ra = 10^7$ and (b) a vertical slice through the centre of instantaneous vertical velocity $v\nu/H$ at $Ra = 2.5 \times 10^6$ and (c) at $Ra = 10^7$.

largest vertical velocity magnitude is found at the mid height of the cell ([Sun and Xia \[2005\]](#)). With the flow field shown in figure 3.8 one can trace the average motion of a typical thermal plume by tracing its path into the core region. For example, when a warm plume reaches its maximum speed, its propagation is impeded because of thermal diffusion and turbulent mixing and thus is decelerated in the upper half region of the

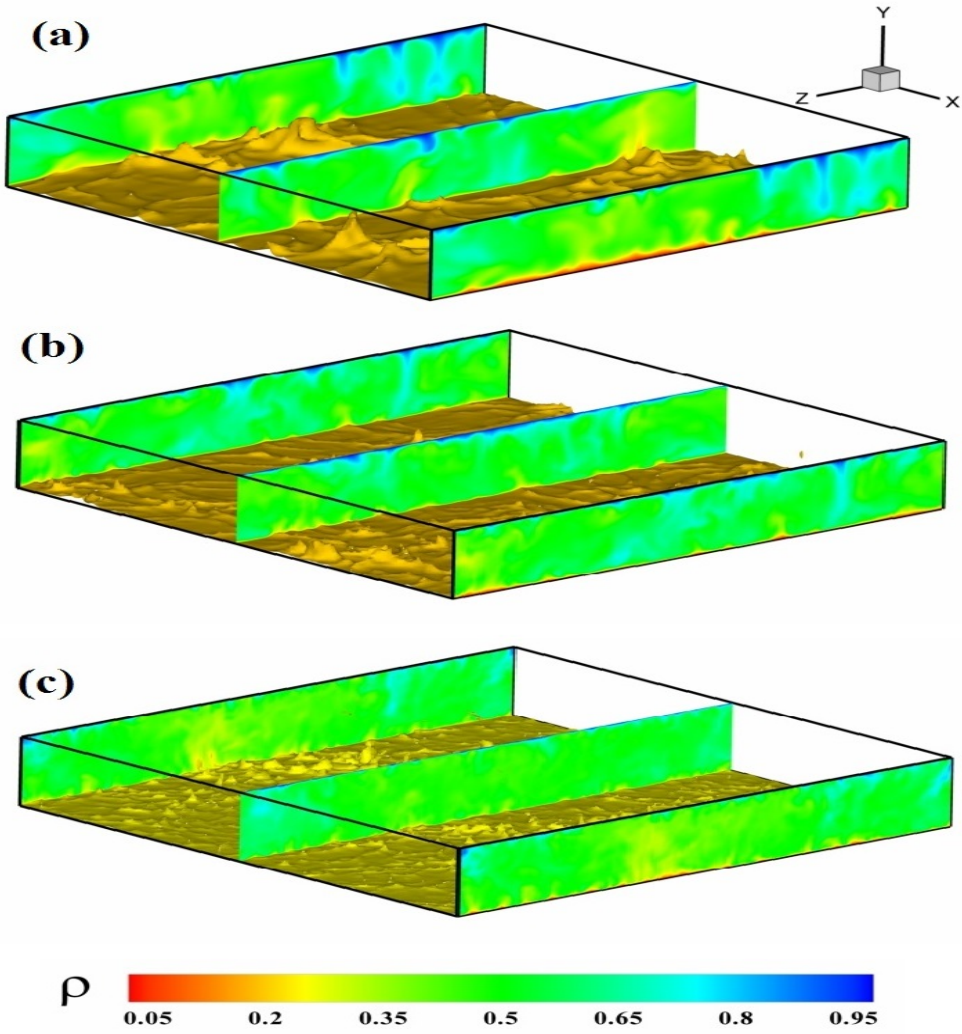


FIGURE 3.9: Snapshot of turbulent Rayleigh-Bénard convection at $Pr = 1$. Plumes are clearly visible through the vertical walls at (a) $Ra = 2.5 \times 10^6$, (b) $Ra = 10^7$ and (c) $Ra = 10^8$, whereas the yellow surfaces reveal the isosurface of density ($\rho = 0.2$)

cell. The velocity in the upper half region of the cell has a large horizontal component, which sweeps the warm plume toward the middle of the cell, and due to heat exchange with the top wall it finishes its life cycle. In this way the warm plume drives the mean flow mainly in the first half of its lifetime. Cold plumes falling from the top wall have a similar process. All clusters of plumes reinforce a large scale circulation encompassing the entire cell. Qualitatively, plume impingement at the top and bottom walls generates horizontal pressure gradients that drive a mean flow. The net transport of thermal energy toward the region with ascending/descending flow causes spatial temperature gradient; these spatial temperature differences induce spatial gradients in the buoyancy which completes the feedback loop (Reeuwijk et al. [2008]).

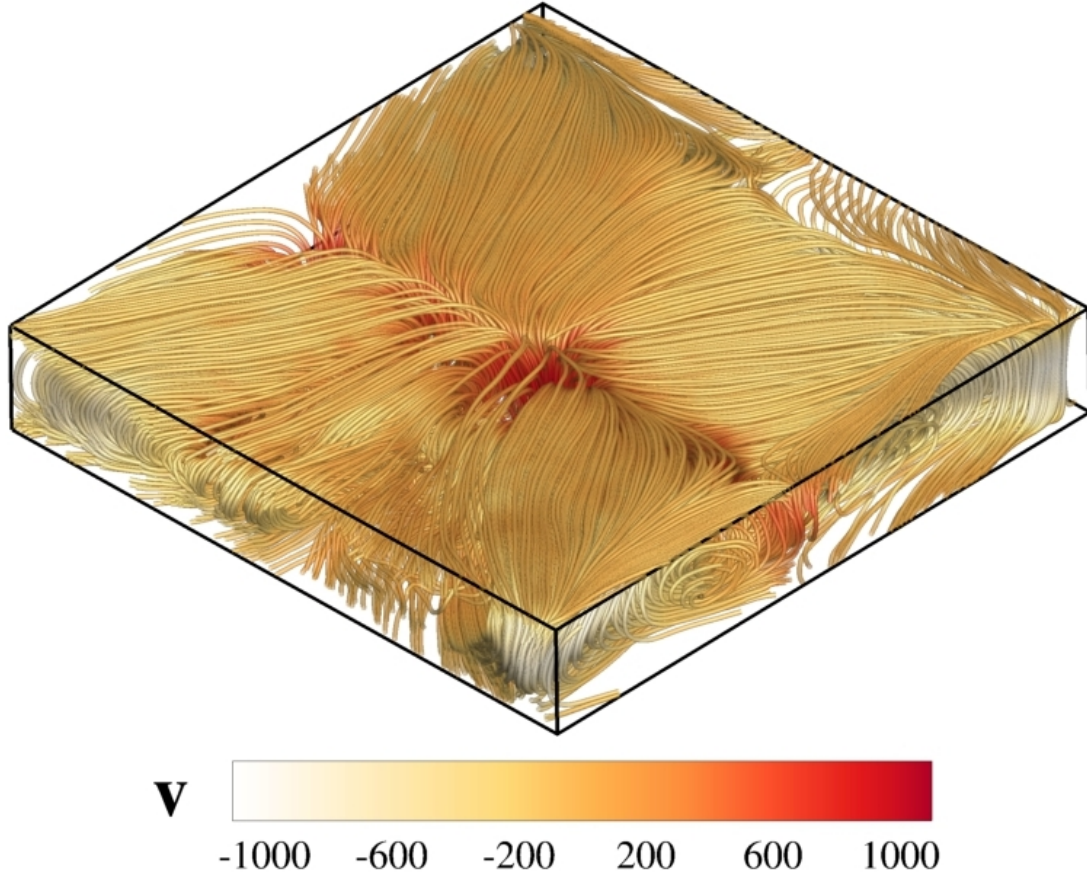


FIGURE 3.10: Time average streamlines of vertical velocity obtained at $Ra = 10^8$, $\text{Pr}=1$ and $\Gamma = 1$

Figure 3.9 illustrates iso-surfaces of instantaneous density over the bottom plate and vertical walls as a function of Ra . We observe that with increasing Ra that flow structures become smaller, and more specifically plumes become thinner. Zhou and Xia [2010] demonstrate the dependence of increasing heat flux on the number of plumes. They found the number densities for both sheet/rod and mushroom like plumes have power law dependences on Ra with scaling exponents of ~ 0.3 which is close to $Nu(Ra)$ scaling exponent. They also report that with increasing Ra number the plume geometry changes from more-elongated to less-elongated, something we also observed in our study. Figure 3.10 shows time-averaged vertical velocity fluctuations at $Ra = 10^8$. Streamlines are colored with respect to their magnitude. Overall, when the flow reaches steady state, thermal plumes generate two large structures within the cell. Indeed the number of "rolls" depends on the domain size (Reeuwijk et al. [2008]).

Chapter 4

Turbulent wind in a cubic confinement

In this chapter we present results from Large Eddy Simulation (LES) for three dimensional RBC in a cubic cell of aspect ratio 1 and for Prandtl number $\text{Pr}=0.7$ and Rayleigh number (Ra) up to 10^{10} using coarse grid mesh. In the first part, we identify the time periods in which the orientation of large scale circulation is constant in order to perform a statistical analysis of the LSC plane. Thermal and viscous boundary layers develop close to horizontal plates with the wind always aligned in one or the other diagonal directions. The special focus is on the spatial distribution of LSC and its influence on first and second order statistics. We also present results of the scaling of the root-mean-square fluctuations of density and velocity measured in the cell centre which is in good agreement with earlier laboratory experiments which found a significant influence of confining geometry on turbulent RBC. Results of this part of the dissertation are published at [Foroozani et al. \[2014\]](#)

The second issue we will study here, is the changing orientation of LSC over long time periods with well-resolved LES and Ra up to 10^{11} . We observed random switching of orientation of the mean wind from one diagonal to the other one.

4.1 Introduction

In this part of study we are focusing on the wall effect on Raleigh-Bénard convection in which all walls considered to be smooth hydrodynamically. As explained before the domain is usually parametrised by an aspect ratio, for example in case of cylindrical cell aspect ratio Γ is defined the ratio of diameter over height $\Gamma = D/H$, while for rectangular or square cross section is one horizontal distance over vertical one. The geometry used here is a enclosed cubic cell with aspect ratio one, and filled with air ($Pr = 0.7$) and for varying Ra in the range of $10^6 < Ra < 10^{10}$ with coarse grid resolution.

We performed LES to resolve large scales and parametrised sub-grid scales using a dynamic eddy viscosity model which appears through the terms τ_{ij} and λ_j in the momentum and density equations. It should be noted that in regards to the geometry effect we are forced to use this parameterization method.

4.2 Methodology

As already stated, the numerical methodology for this complex domain is LES while the sub-grid scales of momentum and heat are parametrised through Lagrangian Dynamic Model. We recall the 3D spatially filtered Boussinesque approximation of the unsteady Navier-Stokes equations in Cartesian frame of reference:

$$\frac{\partial \bar{u}_j}{\partial x_j} = 0, \quad (4.1)$$

$$\frac{\partial \bar{u}_i}{\partial t} + \frac{\partial \bar{u}_j \bar{u}_i}{\partial x_j} = -\frac{1}{\rho_0} \frac{\partial \bar{P}}{\partial x_i} + \nu \frac{\partial^2 \bar{u}_i}{\partial x_j \partial x_j} - \frac{\bar{\rho}}{\rho_0} g \delta_{i2} - \frac{\partial \tau_{ij}}{\partial x_j}, \quad (4.2)$$

$$\frac{\partial \bar{\rho}}{\partial t} + \frac{\partial \bar{u}_j \bar{\rho}}{\partial x_j} = k \frac{\partial^2 \bar{\rho}}{\partial x_j \partial x_j} - \frac{\partial \lambda_j}{\partial x_j}. \quad (4.3)$$

Here, x_1, x_2 and x_3 denote the three spatial coordinates with x_2 or (y) as the vertical upward direction against gravity; u_i is the Cartesian velocity components in x_i direction; P is the pressure; δ_{ij} is the Kronecker symbol. Here also we assumed that the density ρ depends linearly on temperature as $\rho = \rho_0[1 - \alpha(T - T_0)]$, where ρ_0 where ρ_0 is the density at the reference temperature T_0 . In physical space the top-hat-filter in which filter width is set to the size of the grid ($\Delta = \Delta_x \Delta_y \Delta_z)^{1/3}$ applied to the governing equations.

Since the governing equations are solved in non-dimensional form using the normalizations $U_f = \sqrt{\alpha g \Delta \rho H}$; the height H ; free fall time $t_f = H/U_f$ and $\Delta \rho$, all results presented in the following are also non-dimensional, unless otherwise stated.

4.2.1 Computational set up

The geometry is a cube bounded by smooth solid walls at all boundaries, i.e. no-slip condition is applied to all six walls. The vertical lateral walls are perfectly adiabatic [$(\partial \bar{\rho} / \partial \mathbf{n}) = 0$, where \mathbf{n} is the normal vector] and the top and bottom walls are smooth isothermal with a fixed temperature difference ΔT and a given density difference $\Delta \rho$. The Prandtl number Pr under investigation is 0.7 in all simulations, representing the properties of the air under ambient conditions.

We start our simulations with two different type of grid meshes. As mentioned before, we use a *hyperbolic tangent function* to create stretching, in which grid spacing is adjustable by a coefficient in each spacial direction. We use more stretching close to walls, therefore the grid spacing becomes coarser through the cell center. Simulations are first started with a coarser grid and then interpolated to finer ones in order to have a well-resolved simulation on reaching the fully turbulent state.

It is noted that a "proper" mesh resolution should be used in order to obtain accurate results. In a perfect DNS model the local mesh size should be smaller than the local Kolmogorov $\eta_k(\mathbf{x}, t)$ and Bachelor $\eta_B(\mathbf{x}, t)$ scales (see e.g [Monin and Yaglom \[1975\]](#)), and the resolution in the BLs should be also sufficient. It indeed has been well established that the Nusselt number is very sensitive to the grid resolution used in the BLs (see [Stevens et al. \[2010\]](#)). When DNS is under-resolved, the measured Nusselt number is generally too high ([Kerr \[1996\]](#), [Stevens et al. \[2010\]](#)). The standard way to empirically check whether the mesh resolution is sufficient is to try a finer mesh and find where the Nusselt numbers cease to vary significantly. In this way, the minimal number of grid points that is needed in the BL is obtained by trial error. [Grötzbach \[1983\]](#) varied the number of grid points in the BL between 1 and 5 in simulations up to $Ra = 3 \times 10^5$ with $Pr = 0.71$ and found that three grid points in the BLs should be sufficient to resolve boundary layers properly. [Verzicco and Camussi \[2003\]](#) tested this issue at $Ra = 2 \times 10^7$ and $Pr = 0.7$, and stated that at least five grid points should be placed in the BLs in order to have a fully developed simulations. [Stevens et al. \[2010\]](#) tested the grid resolution for $Ra = 2 \times 10^6$ - 2×10^{11} and $Pr = 0.7$. They found that for $Ra = 2 \times 10^9$ the minimum number of nodes in the BLs should be about 10 and this number increases for increasing Ra number. Overall, together with the earlier series of results, it is clear that indeed there is an increase in required grid points in the BL with increasing Rayleigh number. More over the Nusselt number obtained in the simulations not only depend on

grid resolution in the BLs at the top and bottom plates, but also on the grid resolution in the *bulk* and at the side walls where the thermal plumes pass along. Therefore we design our meshes such that grid spacing is varied, increasing toward the bulk from all six walls.

In our simulation we follow the criterion proposed by [Shishkina et al. \[2010\]](#) which is also in agreement with [Verzicco and Camussi \[2003\]](#). Their results is based on the Prandtl-Blasius-type (BP) consideration. The assumption of a laminar boundary layer will break down if the critical shear Reynolds number ($Re_\lambda = 1.72\sqrt{Ux/\nu}$; where x is the distance, U is the fluid velocity outside the boundary layer, and ν is the kinematic viscosity) in the BLs becomes larger than approximately 420 [[Grossmann and Lohse, 2002](#)]). Most experiments and DNS currently available are in regimes where the boundary layers are expected to be still laminar. [Shishkina et al. \[2010\]](#) explore the consequences of BP theory for the required numerical grid resolution of the BLs in DNS. They stated that the number of required nodes within each boundary layer depends on Nu and Pr and grows with the Rayleigh number not slower than $\sim Ra^{0.15}$. Their estimation is in excellent agreement with empirical results where based on the convergence of the Nusselt number in numerical Simulations. Their results show the minimum number of nodes within the thermal and viscous boundary layers, N_θ and N_u , respectively for the case of $Pr \approx 0.7$:

$$\left. \begin{aligned} N_\theta &\approx 0.35Ra^{0.15}, & 10^6 \leq Ra \leq 10^{10} \\ N_u &\approx 0.13Ra^{0.15}, & 10^6 \leq Ra \leq 10^{10}. \end{aligned} \right\} \quad (4.4)$$

According to equation (4.4) for $Pr \approx 0.7$, the minimum number of nodes that should be placed in the thermal and kinetic BLs is $N \approx 2.3$ for $Ra = 3 \times 10^5$, $N \approx 4.4$ for $Ra = 2 \times 10^7$ and $N \approx 8.7$ for $Ra = 2 \times 10^9$. They empirically found values at the respective Ra with $Pr \approx 0.7$ are 3 for $Ra = 3 \times 10^5$, 5 for $Ra = 2 \times 10^7$ and 10 for $Ra = 2 \times 10^9$.

In our simulations, we employ a sufficient number of grid points to resolve boundary layers close to the walls. First for the low Ra number we use $32 \times 64 \times 32$ grid cells in x, y and z direction, respectively, and increase resolution to $64 \times 96 \times 64$ for higher Ra number. The simulation parameters are summarized in table (4.1).

| Ra | $N_x \times N_y \times N_z$ | N_θ | Nu | Nu_{ref} |
|--------------------|-----------------------------|------------|-------|------------|
| 1×10^6 | $32 \times 64 \times 32$ | 14 | 8.31 | 8.32 |
| 3×10^6 | $32 \times 64 \times 32$ | 11 | 11.4 | 11.5 |
| 1×10^7 | $32 \times 64 \times 32$ | 10 | 16.4 | 16.3 |
| 3×10^7 | $32 \times 64 \times 32$ | 8 | 22.4 | 22.0 |
| 1×10^8 | $32 \times 64 \times 32$ | 6 | 31.6 | 31.3 |
| 1×10^9 | $64 \times 96 \times 64$ | 5 | 63.4 | — |
| 1×10^{10} | $64 \times 96 \times 64$ | 5 | 116.2 | — |

TABLE 4.1: Computational parameters and heat transport data for cubic cavities and for $Pr = 0.7$ and varying Ra . The number of grid points in the i -direction is given by N_i . N_θ denotes the number of points in the thermal boundary layer; included for comparison are the DNS data on heat transport Kaczorowski *et. al.* (2013) for the same values of Ra .

4.3 Results and discussion

4.3.1 Local heat flux and mean wind

In order to verify the global properties obtained from the first series of simulations, we compare the global Nusselt number Nu , with earlier numerical and experimental results. We compute the global Nusselt number by:

$$Nu(y) = \frac{\kappa \partial_y \langle \rho \rangle_{A,t} - \langle u_y \rho \rangle_{A,t}}{\kappa \Delta \rho H^{-1}}, \quad (4.5)$$

where $\langle \dots \rangle_{A,t}$ denotes averaging over horizontal planes and time. The two contributions in the numerator of (4.5) are due to the diffusive and turbulent heat fluxes. Note that in this specific flow the Nusselt number is constant along the vertical, and equal to that at the top or bottom walls. We compute the global Nu over bottom ($y = 0$) and top ($y = H$) plate with $Nu_w^{av} = (1/2)(Nu_{bot} + Nu_{top})$, [Armenio and Sarkar, 2002] which consists of a diffusive contribution only,

$$Nu_{bot} = \frac{H}{\Delta \rho} \frac{\sum_{ik} \frac{\partial \rho_{ik}}{\partial x_j} dS_{ik}}{\sum_{ik} dS_{ik}} \quad (4.6)$$

where dS_{ik} is the area element of each grid cell on the $x - z$ plates. We verify the accuracy of the basic quantities obtained in our simulations. We compare our results with those of Kaczorowski and Xia [2013] (see table 4.1) and Wagner et al. [2012] who used resolved DNS in a cube and cylindrical cell, respectively, with $\Gamma = 1$ and $Pr = 0.7$. In terms of its scaling with Ra we obtained $Nu = 0.15Ra^{0.29}$, in good agreement with $Nu = 0.19Ra^{0.28 \pm 0.1}$, the experimental result in the cubic cell of Qiu and Xia [1998] using water as the working fluid. We expect the total heat transport to be independent

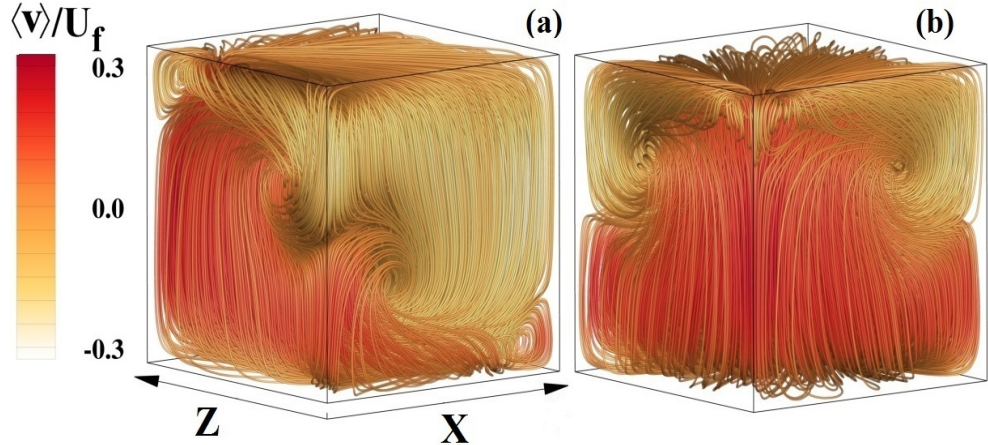


FIGURE 4.1: Streamlines within the full convection cell, time-averaged for more than $5296 t_f$. Greyscale denotes the intensity of the vertical mean velocity, normalized by the free-fall velocity scale U_f . Figure (a) shows the diagonal containing the mean wind and (b) shows the opposite diagonal, containing the strong, counter-rotating cells.

$$Ra = 10^6, Pr = 0.7, \Gamma = 1$$

of the geometric shape of the cell as long as both aspect ratios are equal. Overall, the Nusselt number obtained from our simulations is in excellent agreement with the DNS data, being only 1.8% or so higher. The slightly higher Nu for higher values of Ra can be attributed to insufficient thermal dissipation close to the sidewall, so that hot plumes can travel further from the bottom (top) plate than in simulations (see [Amati et al. \[2005\]](#)).

Even though the global $Nu(Ra)$ scaling in cubic and cylindrical cells shows similar behaviour, it is yet an open point if further effects exist that may influence the flow and thus the statistical properties of the confined convection. For example, thermal plumes might get locked in some spatial configuration due to slight temperature inhomogeneities or corner effects at the plates which might affect the overall thermal dissipation. In the next subsection the flow structure in the cube is further analysed.

4.3.2 Flow structure

As shown by [Wagner et al. \[2012\]](#), the structure of the global flow in cylindrical samples with aspect ratio one is not influenced significantly by modest increases in Ra above $Ra = 10^6$. Figure (4.1) illustrates the time-averaged streamlines for $Ra = 10^6$. The flow exhibits a mean wind moving along one diagonal (figure. 4.1-a) with two small recirculation regions in the corners: one is at the top-left corner where the mean wind coming from below impinges the upper surface of the cavity and the other is at the lower-right corner where the descending mean wind impinges the bottom surface. In the opposite diagonal (figure 4.1-b) two strong counter-rotating vortex structures are shown

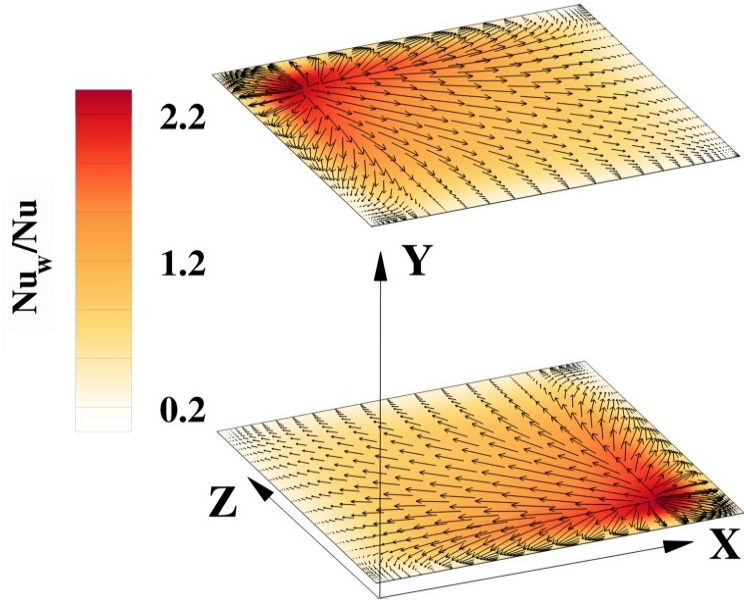


FIGURE 4.2: Contour plots of local heat flux Nu_w at the top and bottom plates, time-averaged over $5296 t_f$. colour scale gives the magnitude of the local heat flux in units of the global Nusselt number. Velocity vectors show the diagonal direction of the LSC for clarity. $Ra = 10^6$, $Pr = 0.7$, $\Gamma = 1$

converging at the mid-plane. Such counter-rotating flows have also been observed in other simulations (see, e.g., [Kaczorowski and Xia \[2013\]](#)). This complex flow structure has significant effects on the resulting turbulent fields.

The mean wind (LSC) depicted in figure (4.1) influences the spatial distribution of local heat flux within the thermal boundary layers. We calculate local non-dimensional vertical heat flux at the bottom and top plates by equation (4.6). In figure (4.2), the spatial distribution of the *heat flux inhomogeneity* on the top and bottom plates, Nu_w/Nu , is presented along with velocity vectors at the first grid points from the wall. The mean wind, oriented along one diagonal plane of the cube, governs the spatial distribution of the heat flux at the wall, which is strongly inhomogeneous over horizontal planes in steady-state. The heat flux at the corner, where the flow impinges on the wall, is much larger than that at the center and on opposite corners. Figure (4.1) also shows that the mean flow exhibits symmetry with respect to the diagonal plane containing the LSC.

4.3.3 Analysis of density and velocity fluctuations

The statistics of density and velocity fluctuations in the cell center are our next focus. This quantity clearly prove the geometry effect in turbulent confinement. We compare the results of this part with [Daya and Ecke \[2001\]](#)—henceforth DE01. We re-call the

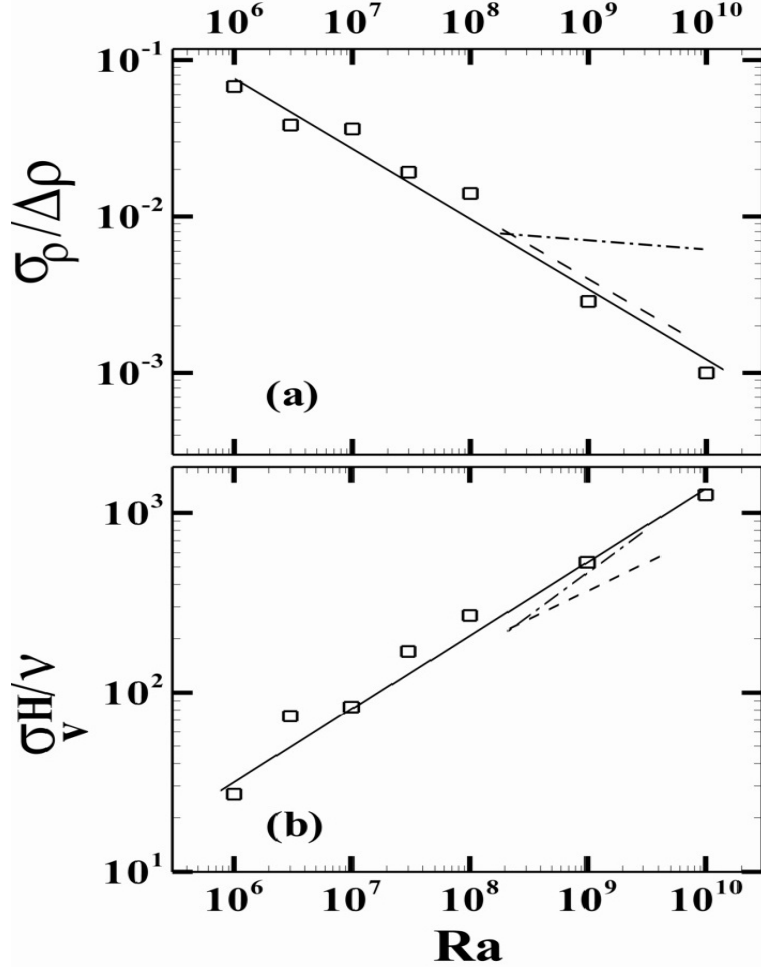


FIGURE 4.3: Normalized fluctuations in (a) density, given by $\sigma_\rho / \Delta\rho$ and (b) vertical velocity, given by $\sigma_v H / \nu$, measured at the cell center. The solid lines are the power law fits to the present data: $\sigma_\rho / \Delta\rho = 49.03 Ra^{-0.46}$ (top) and $\sigma_v H / \nu = 0.31 Ra^{0.39}$ (bottom). Dashed and dash-dotted lines are power law fits, respectively, for the near-cubic cell and cylindrical cell of DE01 for comparison.

root-mean-square (r.m.s) of the resolved density fluctuations equation:

$$\sigma_\rho(\mathbf{x}) = [\langle \rho(\mathbf{x})\rho(\mathbf{x}) \rangle_t - \langle \rho(\mathbf{x}) \rangle_t \langle \rho(\mathbf{x}) \rangle_t]^{1/2} \quad (4.7)$$

and that of resolved vertical velocity fluctuations as:

$$\sigma_v(\mathbf{x}) = [\langle v(\mathbf{x})v(\mathbf{x}) \rangle_t - \langle v(\mathbf{x}) \rangle_t \langle v(\mathbf{x}) \rangle_t]^{1/2}. \quad (4.8)$$

It should be stressed that we check that the contribution of the *SGS* part of each quantity, and it is observed to be negligible in comparison to the resolved part unless otherwise stated.

The normalized density and velocity fluctuations measured at the cell center are shown in figure (4.3) as functions of Ra . The measured fluctuations of density, $\sigma_\rho / \Delta\rho$, are

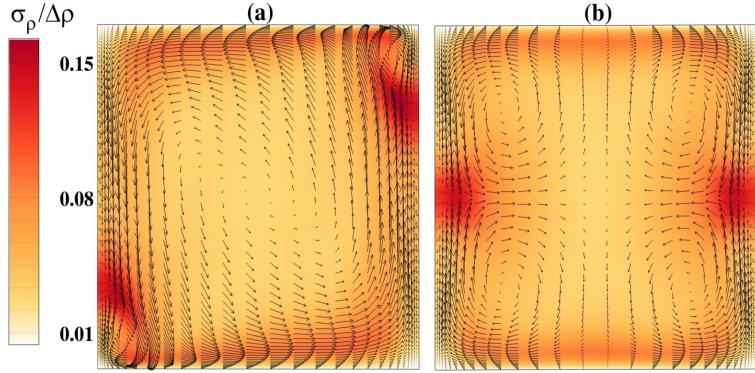


FIGURE 4.4: Time-averaged values of the r.m.s density fluctuations σ_ρ . Greyscale denotes the magnitude of the density fluctuations in units of $\Delta\rho$. Averaging has been performed over $5296 t_f$. Figure (a) shows the vertical diagonal plane containing the large scale circulation and (b) the orthogonal plane to it containing the counter-rotating cells. We have included the velocity vectors for clarity. $Ra = 10^6$, $Pr = 0.7$, $\Gamma = 1$.

well described at the cell center by the power law $\sigma_\rho/\Delta\rho = 49.03Ra^{-0.46}$ (solid line). The scaling behaviour is in excellent agreement with DE01 for a near-cubic cell with $\Gamma = 0.7$, $Pr = 5.46$. Indeed, those authors found a power exponent of -0.48 ± 0.03 (the dashed line in Fig. 4.3a) while, for cylindrical cells under the same experimental conditions, they measured the considerably smaller exponent of -0.1 ± 0.02 (the dash-dotted line). In figure (4.3)-(b) we show the r.m.s velocity fluctuations in our cubic cell and fit it by $\sigma_v H/\nu = 0.31Ra^{0.39}$. This result is also in excellent agreement with DE01 in which the measured exponent was 0.36 ± 0.05 (dashed line). By way of contrast, their result for the cylindrical cell, shown again by a dashed-dotted line, demonstrates the large difference resulting from the change in cross-sectional geometry. The data in figure (4.3) were taken at the cell center. It thus appears reasonable to state that the strong variation between the results for near-cubic or cubic containers, on the one hand, and those for cylindrical containers, on the other, may be tied to “fixed” inhomogeneities of the fluctuations field in the case of the former.

The time-averaged mapping of density fluctuations shown in figure 4.4 reveals fixed inhomogeneities in the vertical planes corresponding to the two diagonals. At the mid-height level, the higher levels of r.m.s density fluctuations correspond to the diagonal opposite that of the LSC where we observe strong counter-rotating vortex structures (see Fig. 4.1-(b) which mix hot and cold plumes at their mid-height convergence. Thus it is no surprise that the largest gradient in density fluctuations occurs at these positions. These counter-rotating flows provide a steady source for the time-averaged horizontal gradient in rms density fluctuations in the central horizontal plane, which provides a physical mechanism for the observed difference in scaling of fluctuations at the cell center between square or cylindrical cross-sections in steady state and under long-time averaging.

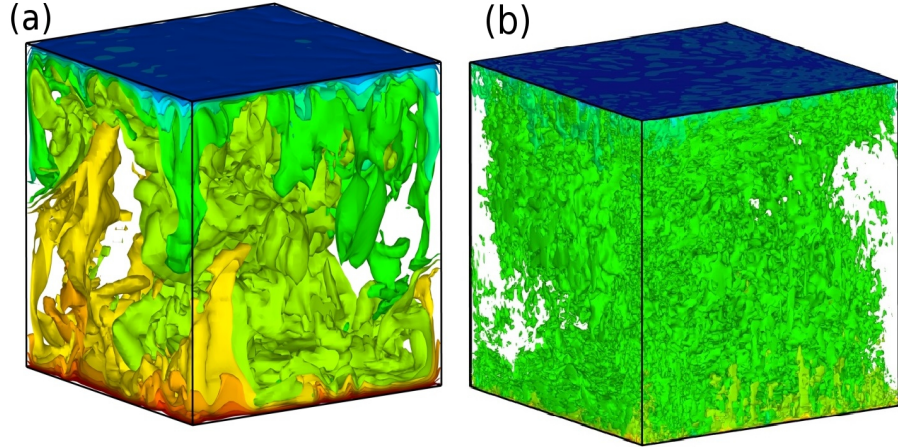


FIGURE 4.5: instantaneous density iso-surfaces for (a) $Ra = 10^8$, and (b) $Ra = 10^{11}$; $Pr = 0.7$, $\Gamma = 1$. Colour range from blue to red for $0.05 < \rho < 0.95$.

In conclusion for this part of study, we have performed numerical simulations of turbulent Rayleigh-Bénard convection in a fluid confined within a cubic enclosure and with molecular Prandtl number 0.7. Data sampling was started only after the flow was fully turbulent and had attained steady state conditions. We observed a stable pattern of LSC for all Ra investigated. Extending the range of Ra accessed by DE01, we have confirmed the scaling seen by those authors for both density (temperature) and velocity fluctuations at the cell center and provide insights on physical mechanisms for the observed (and unexpected) scaling properties. We point out that Pr and Γ are slightly different in the experiment as compared to the simulation, which serves to reinforce the conjecture that cross-sectional geometry (shape) rather than aspect ratio or Prandtl number is the most significant factor in determining the scaling exponent of r.m.s fluctuations at the cell center. The time-averaged, spatial distribution of velocity and its fluctuations provides a key to understanding the differences in scaling observed in cylindrical cells- which in principle have rotational symmetry- to cubic or near-cubic cells which do not.

4.3.4 Wind in turbulent convection and its reversal

As an example of instantaneous flow density iso-surface obtained for $Ra = 10^8$ and $Ra = 10^{11}$ are shown in figure (4.5). Even though the mean flow is similar at these two Ra , the shape of iso-surfaces changes dramatically with increasing Ra . In other worlds, the flow structures decreases rapidly with increasing Ra . More over number of plumes that detach from top and bottom plate increases with Ra . The second part of our focus is on the dynamics of the mean wind and flow structures over a long time period. We extended our previous results for Ra number up to 10^{11} with well resolved LES. As pointed out, one of the the main challenging parts of thermal convection studies

| Ra | $N_x \times N_y \times N_z$ | Δ_{min}/H | Δ_{max}/H | N_θ | Nu |
|-----------|-----------------------------|----------------------|----------------------|------------|--------|
| 10^6 | $64 \times 96 \times 64$ | 1.7×10^{-3} | 1.6×10^{-2} | 12 | 8.29 |
| 10^8 | $64 \times 96 \times 64$ | 7.4×10^{-4} | 2.2×10^{-2} | 6 | 30.85 |
| 10^9 | $128 \times 256 \times 128$ | 3.9×10^{-4} | 7.4×10^{-3} | 8 | 62.25 |
| 10^{10} | $128 \times 256 \times 128$ | 3.2×10^{-4} | 7.8×10^{-3} | 6 | 112.34 |
| 10^{11} | $128 \times 256 \times 128$ | 2.1×10^{-4} | 8.8×10^{-3} | 5 | 230.16 |

TABLE 4.2: Computational parameters of the simulations, all the computations are at $Pr = 0.7$. N_x, N_y and N_z are, respectively the number of grid points in the i direction. Δ_{min} is the minimum grid spacing and Δ_{max} is the maximum grid spacing along vertical direction; N_θ is the number of nodes set within thermal boundary layer.

Nu is the computed Nusselt number compare with [Kaczorowski and Xia \[2013\]](#)

is to achieve *ultimate or asymptotic regime* (high Ra number) in which heat transfer and strength of turbulence become independent of the molecular fluid properties, such as kinematic viscosity and thermal diffusivity. Another interesting feature in confined flows is orientation or reversal of the mean wind. This wind was first observed by [Krishnamurti and Howard \[1981\]](#) through flow visualization studies. Since then, there have been extensive studies of LSC in closed geometry, in which most of the laboratory ([Niemela and Sreenivasan \[2003\]](#), [Niemela et al. \[2001\]](#), [Niemela and Sreenivasan \[2002\]](#), [Sreenivasan et al. \[2002\]](#), [Sun and Xia \[2005\]](#)) and numerical ([Lakkaraju et al. \[2012\]](#), [Wagner et al. \[2012\]](#), [Mishra et al. \[2011\]](#)) studies are in cylindrical container to analysis LSC. But there are only a small number of studies on the dynamic of the LCS in a cubic confinement. It is well known, as we presented above, that the wind in cubic confinement has a diagonal orientation [[Wagner et al., 2014](#), [Zocchi et al., 1990](#), [Qiu and Xia, 1998](#)]. [Breuer and Hansen \[2009\]](#) studied RBC for finite Prandtl number in a *two dimensional* (2D) box and observed reversals of the LSC for very high Ra ($Ra = 10^9$).

Here, we want to resolve the boundary layer and bulk with finer grid resolution. We start with interpolating previous flow fields to finer grids as listed in table (4.2). The grids are stretched from Δ_{min}/H close to the bottom wall to Δ_{max} at the bulk (see table 4.2). At $Ra = 10^9, 10^{10}, 10^{11}$ we used $128 \times 256 \times 128$ grid cells, which dramatically increased the cost of our simulations; in particular they were run for $431t_f$ times only to obtain a reliable value of the Nusselt number. Following our criterion, the grid density near the plates has been enhanced to keep a sufficient number of the nodes in the thermal BL, where the vertical density gradients are very high (see the column N_θ in table (4.2)). Our Nusselt number with the finer grid also shed light on the importance of grid resolution either within λ_θ . The strength of the plumes decreases slowly when the plumes travel further away from the plates, and therefore the grid spacing from the plates to the bulk has to be increased gradually to prevent the plumes from becoming under-resolved just above the thermal plume [Stevens et al. \[2010\]](#).

Probes were placed at different positions in the cell. When the simulations reach steady state we record time series of vertical velocity at each of the these probe positions for $Ra = 10^6$ and 10^8 . For all Ra numbers we evenly distributed 48 probes at $/H = 0.25, 0.5$ and 0.75 distance from the bottom wall. Each horizontal plane contains 13 probes. Figure (4.6) shows a time series of vertical velocity at $Ra = 10^6$ and at mid-height ($y/H = 0.5$) for probes 1 and 3. Probe 1 is placed at $x = z = 0.23$ and probe 3 is placed at $x = z = 0.77$. Both probes 1 and 3 are further placed along diagonal direction. In addition, there are two probes placed along another diagonal: we call them probe 2 and probe 4. Probe 2 is placed at $x = 0.77, y = 0.5, z = 0.23$ and probe 4 is at $x = 0.23, y = 0.5, z = 0.77$. Figure (4.7) shows time series of vertical velocity recorded by probes 1 and 3 (top panel) and probes 2 and 4 (bottom panel) at $Ra = 10^6$. It clearly shows that the vertical velocity at four probes are anti-correlated. These observations indicate the presence of a large scale convection structure. When the mid-height probes in a given diagonal both show a value near zero with high variability, it suggests that the flow in that diagonal is dominated by counter-rotating cells. As shown the local mean value of vertical velocity changes sign occasionally and this feature is called a “reversal” of the LSC in the literature for cylindrical cells (Niemela et al. [2001], Mishra et al. [2011]). Figure (4.7) shows time series of the probes at $Ra = 10^8$. we find the mean wind at $Ra = 10^8$ has greater time interval to be stable at its diagonal position, while at low Ra it switches more often. Contour plot in figure (4.9) shows time averaged density on the diagonal plane of (a) LSC and (b) orthogonal to it at $Ra = 10^6$. Note that for all time averaged results presented here, we found optimal time interval of flow, where the flow is stationary at a position. Through the work (except for the Nu analysis) the fields are averaged over a described time periods without reorientation. With the flow field shown (in figure (4.9), (4.1) one can trace the average motion of a typical thermal plume from boundary layer to the core region, which provides the most and quantitative evidence to demonstrate the LSC flow structure in the $\Gamma = 1$ cubical cell. A similar flow structure also found in rectangular shape convection box (Xia et al. [2003]).

4.3.5 Time averaged velocity field

In order to develop the model, we now examine the flow field with respect to its time intervals. For all Ra we analyses the velocity vector map time averaged over a short period of time ($500t_f - 1500t_f$) “during which the large scale motion remains in one direction”. We provide a series of time-averaged snapshots for $Ra = 10^8$ The mean flow depends on the time-window considered for the averaging. In order to study short-term convective dynamics, we neglect long-term variations, applying a time-average on sub-intervals of time, when necessary. Within the range of $10^6 < Ra < 10^{11}$, we observed

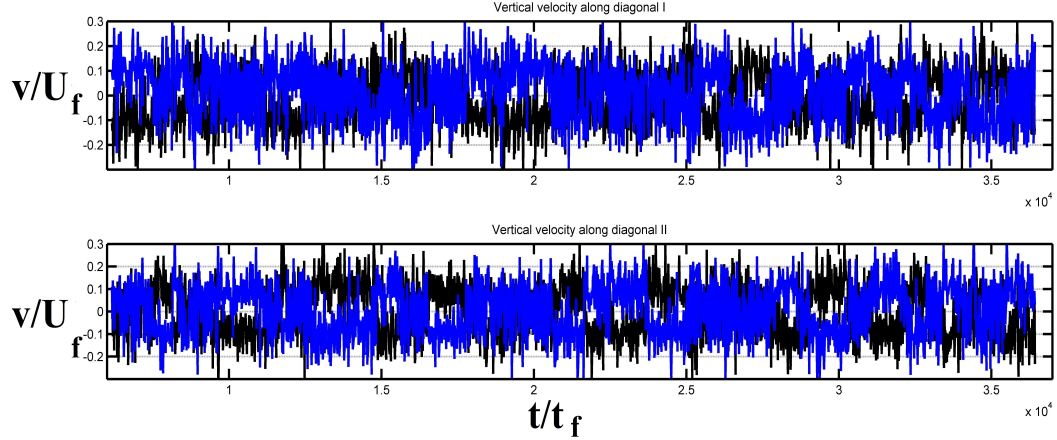


FIGURE 4.6: For $Ra = 10^6$ on a $64 \times 96 \times 64$ grid of $\Gamma = 1$, time series of the vertical velocity measured by the probes at $y=0.5$ (mid-plane) (Top panel) probe 1 is placed $x = z = 0.23$ and probe 3 at $x = z = 0.77$. Time is measured in the units of the free fall time H/t_f (Bottom panel) probe 2 at $x = 0.77, z = 0.23$ and probe 4 at $x = 0.77, z = 0.23$. Time is measured in the units of the free fall time H/t_f

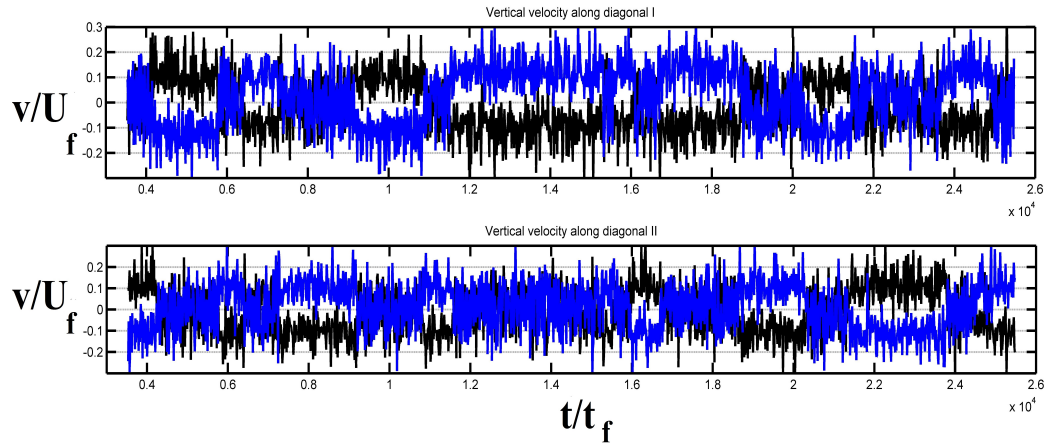


FIGURE 4.7: For $Ra = 10^8$ on a $64 \times 96 \times 64$ grid of $\Gamma = 1$, time series of the vertical velocity measured by the probes at $y=0.5$ (mid-plane) (Top panel) probe 1 is placed $x = z = 0.23$ and probe 3 at $x = z = 0.77$. Time is measured in the units of the free fall time H/t_f (Bottom panel) probe 2 at $x = 0.77, z = 0.23$ and probe 4 at $x = 0.77, z = 0.23$. Time is measured in the units of the free fall time H/t_f

stable pattern of mean wind in the cube cell. [Sreenivasan et al. \[2002\]](#) found when the flow is very turbulent ($Ra > 10^{14}$ for $Pr \sim 1$) structured large scale circulation eventually disappear. It is however, conjectured that the strongly unsteady eddies allow the boundary layer formation.

We refer to the large scale circulation as any kind of instantaneous, steady or stationary large eddy having a size of the same order of the cell depth, and swirling mainly in vertical direction and develop such that to occupy maximum space within the enclosure. When a large scale circulation shows steady or stationary features, it is also referred to as pattern. Figure (4.8) shows the diagonal direction of the LCS. Time averaged is taken over a $1062t_f$

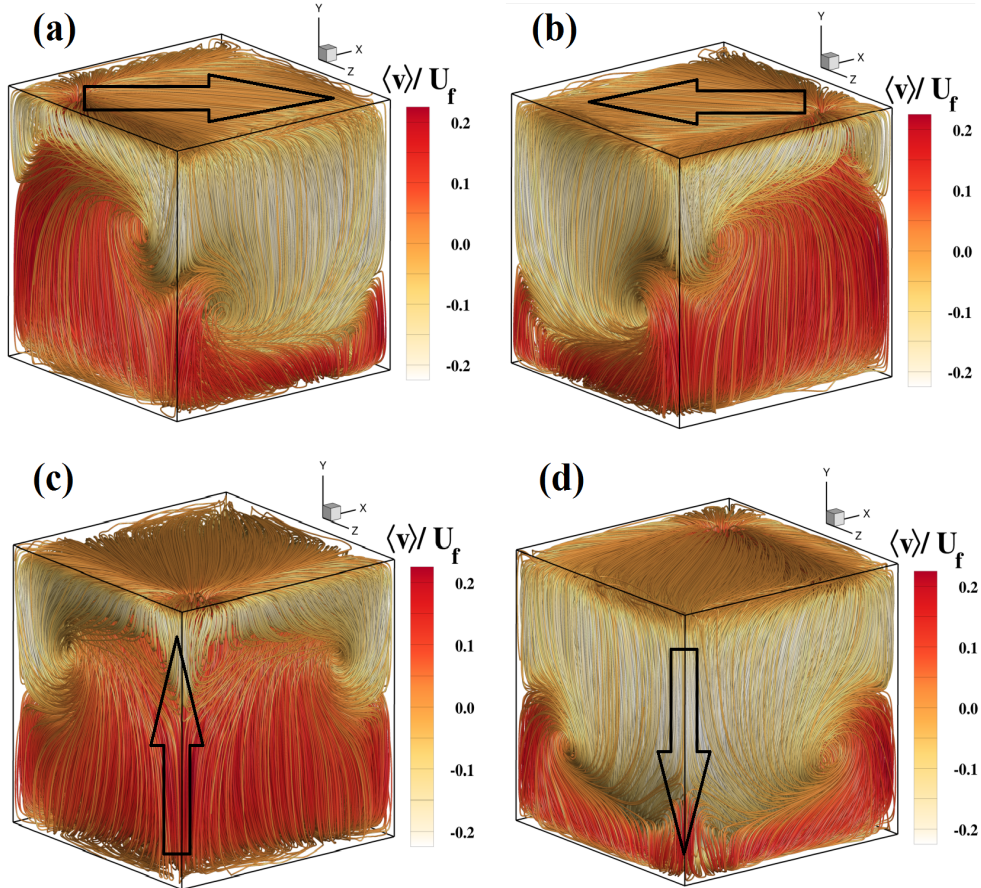


FIGURE 4.8: Time average of vertical velocity streamlines . Gray scale denotes the intensity of the vertical mean velocity normalized by the free fall velocity scale U_f ; $Ra = 10^8$; $Pr = 1$; $\Gamma = 1$. Series of data represents switching of the mean wind.

time units during which the large scale circulation remains clockwise. Counter-clockwise LSC is time averaged taken over $500t_f$. It should be stressed that change of the wind direction presented here are not in order. We observed mean wind switches between the corners stochastically over a longer period of time. This is contrary of the situation in the plane of the LSC, in which the vertical velocity in the side wall region is locked in one direction most of the time. More over the reversals of the flow direction at the two opposite positions take place at approximately the same time, suggesting that the velocity field in the plane perpendicular to that of the LSC is still correlated in space.

In these figures, red colour indicates upward (positive) motion and yellow indicates downward (negative) motion. By following the time series of vertical velocity we observed four stable pattern in cubic confinement whose $\Gamma = 1$.

The time-averaged density distribution in both diagonal planes is provided in figure (4.9), where the formation of LSC (figure 4.9)-(a) and secondary flow structures (4.9)-(b) can

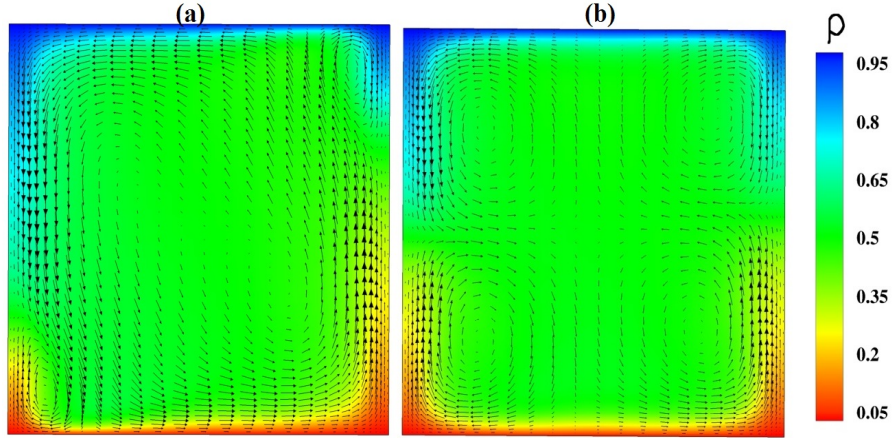


FIGURE 4.9: Time averaged density distribution and 3D velocity vectors in the diagonal planes of the cube. The LSC observed in (a) plane and secondary flow structures in plane (b) at $Ra = 10^6$ on grid $64 \times 96 \times 64$ and $\Gamma = 1$, $Pr = 0.7$. We have also included the velocity vectors for clarity.

be observed at $Ra = 10^6$. Because of the time-averaging effect, two mean fields with opposite sense of flow direction yields a four-roll pattern similar to the one illustrated in figure (4.9)-(b).

A time-evolution analysis of flow structures is quite complex owing to the strong 3D features of the flow snapshots. Thus, in addition to 3D visualization of instantaneous and mean fields, we have monitored the local shear at the side wall. An interesting feature of the LSC is its footprint on the vertical walls, indicated by the wall shear stress. We compute absolute wall shear stress over horizontal plates by:

$$\tau_{w,H}^{total} = \sqrt{\langle \frac{\partial u}{\partial y} \rangle_t^2 + \langle \frac{\partial w}{\partial y} \rangle_t^2}. \quad (4.9)$$

This is displayed by colours (colour range from blue to red for $2 < \tau_w < 42$ at $Ra = 10^8$) and its components due to vertical motion. Figure (4.10) shows the contour plot of wall shear stress at $Ra = 10^8$, it reveals that the mean motion is oriented in one of the diagonal directions of the cell showing a plate filling behavior ([Grossmann and Lohse \[2003\]](#)) with complex flow structures in the vicinity of the side walls. Similar to distribution of local heat flux, the maximum value of wall shear stress is observed at the positions of detaching or impinging of thermal plumes from the boundary. These position indicate that the mean wind pass along and has maximum velocity gradient.

Figure (4.11) present time averages of vertical velocity and its wall shear stress (colour ranges from blue to red for $20 < \tau_w < 160$) at $Ra = 10^{11}$. The time average is over $431t_f$ (free fall velocity times). At much higher Ra number we also observed diagonal orientation of LSC, although the secondary rolls in LSC plane become smaller than

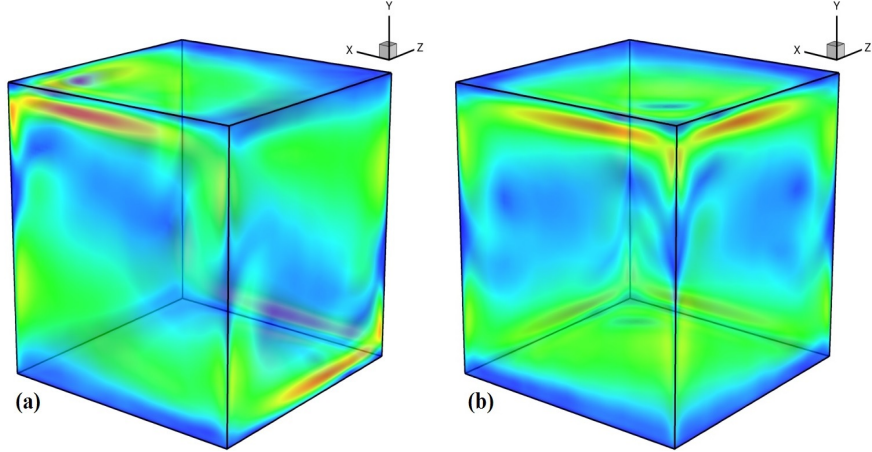


FIGURE 4.10: Time average wall shear stress; colour range from blue to red for $2 < \tau_w < 42$ at $Ra = 10^8$; on the walls (a) is plotted for 4.8-d and (b) is plotted for 4.8-a. Note the coordinate directions.

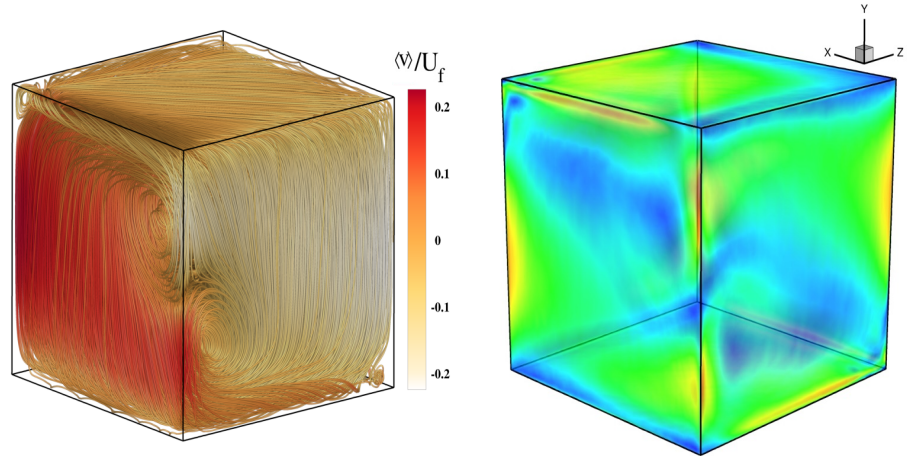


FIGURE 4.11: Time average of vertical velocity streamlines . Gray scale denotes the intensity of the vertical mean velocity normalized by the free fall velocity scale U_f ; $Ra = 10^{11}$; $Pr = 1$; $\Gamma = 1$ and its wall shear stress ranges from blue to red for $20 < \tau_w < 160$

low Ra . By measuring the change of the flow's effective path-length with Ra , Niemela and Sreenivasan [2003] for ($\Gamma = 1$ in cylindrical cell) suggested that the mean flow will change its shape from ellipse-like to squarish-like as Ra increases. We have observed the same behavior for cubic cell. At high Ra number the shape of LSC changes to a more rectangular form and occupying more space within the cell which also explains the effect on the size of secondary rolls. It is important to note that 3D structure of the flow field is a time-averaged result, which ignored the time variation of the flow field in the closed cell. While the long time average is a powerful tool to filter out random noise, it may also average out some interesting dynamics in the flow field. Therefore, further study the dynamics in turbulent convection, one needs to examine the time dependence of the

velocity field. In regards to the long-time averaged mapping of r.m.s density fluctuations shows fixed inhomogeneities that maintain its own structure when the flow switches from one corner to the other with still the largest fluctuations level at the mid-height.

Chapter 5

Dependence of heat transport properties on surface roughness with different shapes—a preliminary study

The objective of this part is to approximate the enhanced heat transport in thermal convection with two different geometric roughness shapes on the heated (bottom) and cooled (top) horizontal plates. This is a preliminary study which is on-going, but a substantial amount of work has already been done in preparing the code that advances the state-of-the-art and this is discussed here. Some of the conclusions should be tempered with the fact that this is a preliminary work-in-progress. In substance, we study geometric effect of roughness elements on thermal convention having smooth or "discontinuous" connections between elements (i.e., sharp corners for the case of pyramids). It is well known that roughness enhances heat transport in turbulent Rayleigh-Bénard convection, with preferential release of thermal plumes at the sharp roughness element tip. These assumptions motivated us to perform two different 3D roughness shapes—one with a relatively smooth surface—in which both has almost same contact area within highly controlled conditions by means of LES methodology. To our knowledge, this is the first numerical study of non-smooth wall thermal convection in which roughness has 3-dimensionality (e.g. pyramids instead of grooves).

5.1 Introduction

Rayleigh-Bénard convection, a closed system containing working fluid heated from below and cooled from the top, studied in previous chapters extensively with smooth plates. One of the major issues in the study of turbulent convection is to understand how heat transported across the convection cell by turbulent flows. In general it is known that the characteristic roughness of solid-fluid interfaces have a significant effect on turbulent shear flows, such as the isothermal flow in pipes [Tennekes and Lumley \[1970\]](#). In RBC, As heat transfer is limited by diffusion in the thin BL at the top and bottom plates, investigation of the heat transport properties of the individual plates is also of some interest, in addition to fluid dynamical effects resulting from the recirculating shear flow (mean wind) over the solid-fluid surfaces. Of course, these latter effects only take place when the thermal boundary layers are comparable or smaller than the thermal boundary layer thickness.

Virtually all surfaces of geophysical or meteorological interest are rough in some sense. The characteristic height of the roughness elements in nature ranges from a few microns in the case of snow, to several centimeters in open rural terrains, and to tens of meters over forest and cities. The thickness of atmosphere boundary layer is $\delta \approx 500m$, so that the ratio of boundary layer over roughness height is large in open rural areas, but not necessarily so over cities or forests. [Jiménez \[2004\]](#) found that viscous boundary layer λ_v behaves as a rough surface when the roughness height is the order of $\lambda_u/50$. Moreover in thermal convection, the additional scale should also be considered in our study as we explained in chapter 3 and 4. In our study we worked with low Prandtl numbers ($1 \leq Pr$), therefore λ_θ and λ_u are of the same order of magnitude and the condition of $\lambda_u/\delta \geq 50$ does not apply either in the experimental study or in the present work.

A number of experimental and numerical studies have shown that an effective way of enhancing the heat flux is to use rough surfaces instead of smooth ones [\[Amin, 1991, 1993, Shen et al., 1996, Du and Tong, 2000\]](#).

Perhaps [Shen et al. \[1996\]](#) were the first to make study of non-smooth RBC. Using plates regularly spaced pyramids, they found that once the height of the pyramids δ becomes comparable with the thickness of thermal boundary layer λ_θ , there would be enhanced heat transport by the surface roughness. Using a cell with higher pyramids than that in [Shen et al. \[1996\]](#), [Du and Tong \[2000\]](#) made a visualization study of plume emissions from the tip of the pyramids with thermochromatic liquid crystal particles. Based on the measurement of temperature statistics the fluid and temperature fields visualization, they concluded that the enhancement of heat transport is due to the enhanced plume emission frequencies from the tip of pyramids. [Shen et al. \[1996\]](#) reported that rough plates cause an increase of the pre-factor A in the scaling law $Nu \sim ARa^\beta$ (about 20%)

if the thermal boundary layer thickness becomes smaller than the roughness height. This was also observed by [Du and Tong, 2000]. Roche et al. [2001] observed an increase of the exponent β under these conditions with rough surfaces up to a value of 0.51, which they postulated was an indication of the Kraichnan ultimate regime (Kraichnan [1962]). Whether this is due to a transition to higher A or a real change in exponent β is difficult to assess. In an experimental study by Qiu et al. [2005], a growth of the exponent β up to 0.35 was found for $Ra \geq 10^8$ even for regular roughness elements. The differences in the results are usually explained by the different Ra regimes and different roughness shapes (for example, Ciliberto and Laroche [1999] used spheres, Shen et al. [1996] and Du and Tong [2000] used pyramids and Roche et al. [2001] used V-shape grooves).

Earlier numerical simulations by [Amin, 1991, 1993] showed that by introducing a wall roughness, one can decrease or increase Nu up to 50%, the former occurring when only the vertical walls are heated but the roughness is placed on the horizontal boundaries, whereas if the rough horizontal plates are heated or cooled and adiabatic vertical walls are smooth, the mean heat flux increases. In their numerical investigations of thermal convection over grooved plates Stringano et al. [2006] found an increasing of Nu number with a steeper power law, i.e with an increase of β from 0.31 to 0.37, for $Ra > 10^8$ where the thermal boundary layer thickness becomes smaller than the height of the groove. These authors used cylindrical cell of $\Gamma = 1/2$ at fixed Prandtl number of 0.7. They design the grooved with a tip angle of 90° and with height $\delta = 0.25H$ over top and bottom plates. With the cell of diameter-over-height $\Gamma = 1/2$ the upper and lower plates are paved by N=5 axisymmetric grooves. Moreover their results showed that the secondary structure (eddies) trapped between the grooves would lift up the boundary layers. They suggests that the eddies between grooves help to detach the plume from the tip.

Wei et al. [2014] experimentally studied RBC with five different cells of smooth and rough walls with different heights of pyramids ($\delta = 3mm, \delta = 8mm$). Their results reveal some asymmetries in the communication between flows over rough and smooth plates, and also on the type of thermal boundary condition (fixed temperature or heat flux).

To the best of our knowledge most of the numerical studies have 2D roughness elements, while a number of experimental studies employ 3D shapes [Du and Tong, 2000, Wei et al., 2014]. Therefore, a comprehensive analysis and advancement of the theory of the heat transfer in convection cells with rough walls is still required. In the present work we study numerically the impact on the mean heat transport of smooth and sharp elements distributed on top and bottom isothermal plate where the lateral walls are smooth.

| Case: | Ra | $N_x \times N_y \times N_z$ | Δ_{min}/H | Δ_{max}/H | Nu |
|---------------|-----------------|-----------------------------|------------------------|-----------------------|-------|
| Pyramid | 1×10^8 | $128 \times 128 \times 128$ | 3.125×10^{-3} | 1.36×10^{-2} | 30.05 |
| Sine-function | 1×10^8 | $128 \times 128 \times 128$ | 3.621×10^{-5} | 1.37×10^{-2} | 30.35 |

TABLE 5.1: Simulation details of two different roughness geometries. The number of grid points $N_x \times N_y \times N_z$ in i -direction $N_i(i = x, y, z)$; Δ_{min}/H is the minimum grid spacing and Δ_{max}/H is the maximum grid spacing along vertical direction; Nu is the normalized heat flux.

5.2 Numerical set-up

In this part of study, we simulate the flow developing in a cubic confinement by inserting rough elements with two different geometries over top and bottom plates, vertical walls are perfectly smooth.

We recall spatially filtered NS equations under Boussinesq approximation to solve flow field:

$$\frac{\partial \bar{u}_j}{\partial x_j} = 0, \quad (5.1)$$

$$\frac{\partial \bar{u}_i}{\partial t} + \frac{\partial \bar{u}_j \bar{u}_i}{\partial x_j} = -\frac{1}{\rho_0} \frac{\partial \bar{P}}{\partial x_i} + \nu \frac{\partial^2 \bar{u}_i}{\partial x_j \partial x_j} - \frac{\bar{\rho}}{\rho_0} g \delta_{i2} - \frac{\partial \tau_{ij}}{\partial x_j}, \quad (5.2)$$

$$\frac{\partial \bar{\rho}}{\partial t} + \frac{\partial \bar{u}_j \bar{\rho}}{\partial x_j} = k \frac{\partial^2 \bar{\rho}}{\partial x_j \partial x_j} - \frac{\partial \lambda_j}{\partial x_j}. \quad (5.3)$$

Where x_1, x_2, x_3 denote the three spatial coordinates with x_2 as the vertical (upward) direction, u_i is the velocity component in the x_i direction, P is pressure and δ_{ij} is the Kroneker symbol. In the model it is assumed that density ρ depends linearly on temperature as $\rho = \rho_0[1 - \alpha(T - T_0)]$, where ρ_0 is the density at the reference temperature T_0 . The overbar symbol denotes the filtering operation which is performed here in the physical space using a top-hat filter function.

The above equations have been written in a Cartesian coordinate and discretized on a non staggered mesh by central second order accurate finite-difference approximation (details of numerical method and solver is explained in chapter 2).

For the present study we used well resolved LES with equally space grids in $x-z$ directions stretched by using Vinokur [1980] in vertical direction. For the present problem we used our previous $Nu(Ra)$ scaling which obtained over flat-plate flow, in order to compute an average thermal boundary layer by the relation $\bar{\lambda}_\theta = H/(2Nu)$, one can obtain $\bar{\lambda}_\theta/H \approx 1.61 \times 10^{-2}$ for $Ra = 10^8$.

The geometry used here is a cubic confinement with square cross section of $\Gamma = 1$. The vertical walls are perfectly adiabatic and top and bottom plates are isothermal. We apply density gradient $\Delta\rho/\rho_0 = 1$ in vertical direction. The constant Prandtl, Pr , number under investigation is 0.7, representing the properties of the widely used media air at ambient conditions. We study thermal convection by the roughness of heated/cooled horizontal plates. The roughness is introduced by a set of 3D pyramid and sinusoidal heated/cooled shapes located at the corresponding plates.

- (i) For pyramid geometry with height $\delta = 0.025H$ has been used since it is close to [Du and Tong \[2000\]](#) and equal to the study of [Stringano et al. \[2006\]](#). Pyramid spacing is $2a = 5\delta = 0.125H$ (see figure 5.1) with grid density along x, y and z direction ($128 \times 128 \times 128$). Here we also used the same criteria to stretch grid cells within the boundary layers [[Verzicco and Camussi, 2003](#)] in order to sufficiently resolve the boundary layers. In the horizontal direction the grid spacing is equidistant, $a = 8\Delta_{x-z} = 0.0625H$, in which Δ_{x-z} is alter $x-z$ grid space, and in vertical direction we have stretching within the boundary layers. Therefore Δ_{min}/H is the minimum grid spacing close to rough walls and towards the bulk the grid spacing become coarser. Consequently Δ_{max}/H is maximum grid spacing at cell center. Therefore by these settings, we found the slant angle of pyramid be $\beta = 21.8^\circ$ and the tip angle is $\alpha = 136.6^\circ$ (see figure 5.1). The total number of axisymmetric pyramids spread over upper and lower plates are $N = 64$ (see 5.2-(a)).
- (ii) For sinusoidal geometry we used function given by:

$$y(x, z) = \delta \sin^2(a\pi x) \sin^2(a\pi z). \quad (5.4)$$

Note that we are using only positive peak of sine-wave.

The amplitude δ of sinusoidal function is much smaller than its wavelength $4a$. Therefore, above function would create continues asperities surfaces between peaks in which hemisphere can not. We apply the same condition for grid spacing in this case, and $N = 64$ sine elements spread over top and bottom plates (see 5.2-(b)).

In every direct numerical simulation, in order to perform a proper DNS, all the scales down to the smallest must be captured by an adequate grid resolution. In turbulent thermal convection these are the Kolmogorov (η_k) and the Batchelor scales (η_T), in the bulk, and the viscous (λ_u) and thermal boundary layer (λ_θ) thickness close to the solid boundaries need to be resolved which requires a large number of computational nodes. [Stringano et al. \[2006\]](#) studied thermal convection over grooved surfaces by means of DNS,

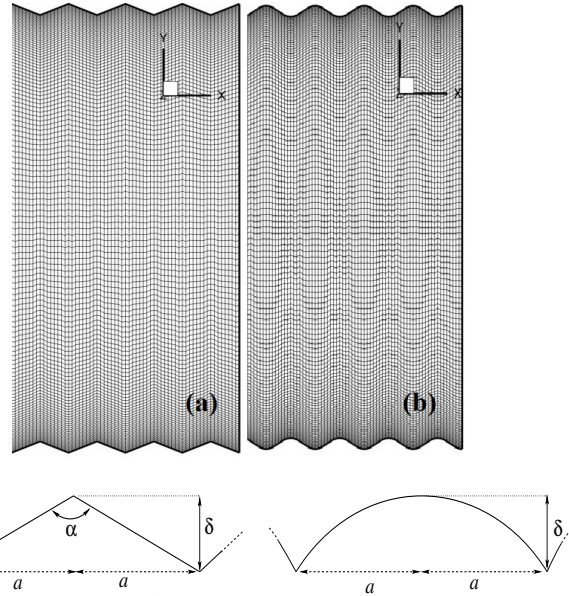


FIGURE 5.1: Sketch of grids distribution in vertical direction ($x-y$) view of (a) pyramid and (b) sinusoidal geometries with details of roughness elements.

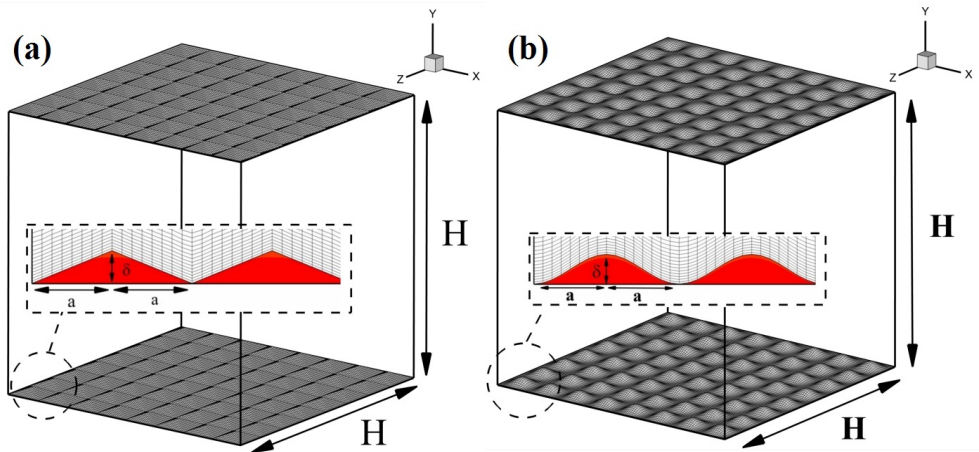


FIGURE 5.2: Perspective sketch of convection cells with (a) pyramids and (b) sinusoidal elements distributed over upper and lower plates. All vertical walls are smooth

for $\Gamma = 1/2$ and $Ra = 2 \times 10^8$, as an example for this case, they used $97 \times 151 \times 209$ and $129 \times 201 \times 301$ nodes in the azimuthal, radial and vertical directions, obtaining, respectively, $Nu = 45.88 \pm 0.05$ and $Nu = 45.57 \pm 3.35$. They used 100 large-eddy-turnover time for each simulation to obtain converged statistics. Due to the increase of simulation cost by means of DNS, they could achieve Ra up to 2×10^{11} .

It is worth mentioning that the numerical simulations data sampling started once the flow was fully turbulent and had become statistically steady. Moreover individual runs were performed for both cases over $1518t_f$. In this part we present the primary results of our simulation.

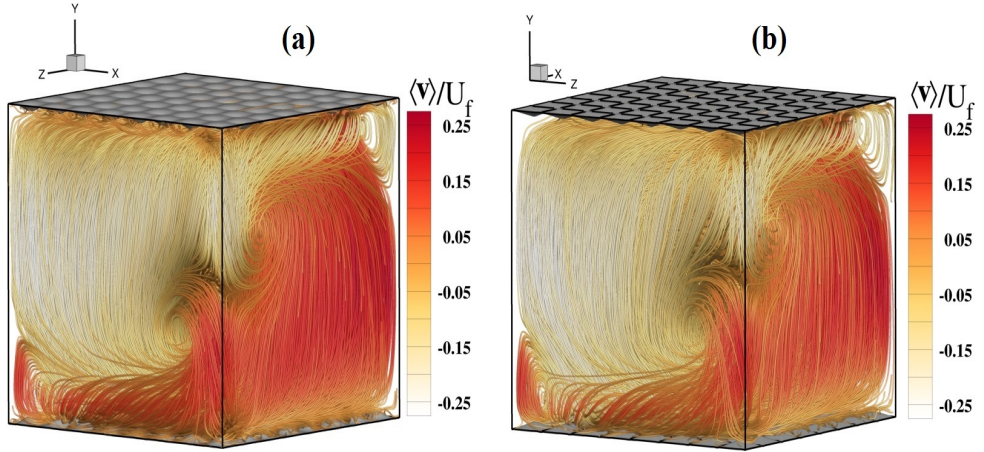


FIGURE 5.3: Visualization of 3D large scale mean flow that is obtained by time averaging over $1518t_f$ at $Ra = 10^8$, $Pr = 0.7$ for (a) sinusoidal and (b) pyramid roughness. Both cells shows diagonal direction of mean wind. Gray scale denotes the intensity of the vertical mean velocity, normalized by the free fall scale U_f

5.3 Results and discussion

5.3.1 Flow visualization

In this study, we chose constant $Ra = 10^8$ for both cases of roughness elements under investigation. The increase of Ra is one of our main aims for the on-going and future studies.

We know that in cubic confinement, the LSC prefers to align with corners but it switches between the corners stochastically (see chapter 4). Perhaps not unsurprisingly we observed diagonal orientation of the mean wind also with the present of obstacles. It is worth mentioning that the height of elements has a significant influence on the large scale circulation: ([Shishkina and Wagner \[2011\]](#)) studied analytically rectangular heated/cooled obstacles located at horizontal plates and found that roughness height can influence the characteristics of the bulk flow, due largely to the nature and strength of the secondary eddies between obstacles. Their study was based on two-dimensional Prandtl-Blasius boundary layer equations and therefore is valid for moderate Ra numbers and regular wall roughness.

We point out that time-averaged velocities for the extra secondary eddies between obstacles are generally larger for the higher roughness elements and larger distance between them but anyway are much smaller than that of the LSC.

Figure (5.3) shows time-averaged streamline of vertical velocity, normalized by free fall velocity U_f , for sinusoidal and pyramid geometries. For these roughness heights there is no obvious dependence of the mean flow or secondary eddies on the shape of the elements.

Figure (5.4) shows a time series of only a small time window of the whole simulation and

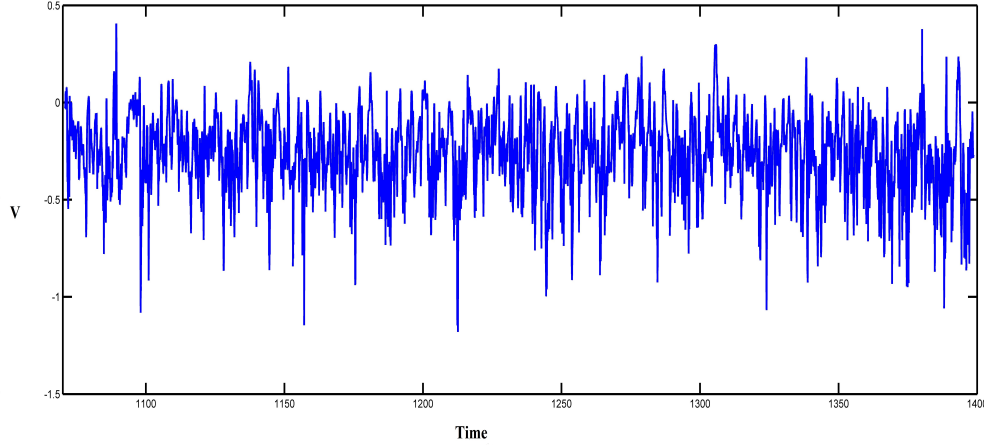


FIGURE 5.4: The time series of vertical velocity measured by probe at $y = 0.5$ (mid-plane) and $x = z = 0.2$ for pyramid cell

for a probe placed at the mid height and close to the cell corner, for pyramid roughness $x = z = 0.24$ (outside viscous boundary layer region). We have not observed switching of the LSC yet under these rough conditions. It should be stressed that we used a time interval for which the flow is stable and statistically stationary at one diagonal corner to compute time averaging of the vertical velocity. Observations of a four-roll pattern for both one diagonal plane and the other that is orthogonal to it result from averaging of two mean fields with *opposite* sense of flow direction (See figure 5.8b)

We compute the global heat flux normalized by the cross section ($S = H^2$) at height y [Stringano et al., 2006]:

$$\int_{wall} \nabla \rho \cdot \mathbf{n} dS = (\sqrt{RaPr} \bar{v} \bar{\rho} - \frac{\partial \bar{\rho}}{\partial y}) S, \quad (5.5)$$

where S_w is the wet surface of the roughness elements. We find $Nu = 30.05$ for *pyramid* and $Nu = 30.35$ for *sinusoidal* elements. At this $Ra = 10^8$ number we have not seen any discernible difference in the heat flux from that of smooth plates. Of course, the roughness height is less than a factor of two above the estimated thermal boundary height. Other factors are that we have pyramids rather than grooves so that the continuous sharp edges facilitating plume production are for us really finite points. One other factor is that, for us, the slant angle is relatively small. For example in the study of Stringano et al. [2006], the slant angle is 90° that would create a steeper slope.

The wet surface of the plate (both cells) is S_w , computed as follows:

Pyramid; The wet area is given by: $S_w = \sum_{n=1}^{64} 2a\sqrt{4\delta + 4a^2} = 1.07S$.

Sinusoidal; The wet area is computed by smooth function $y = f(x, z)$ in which (x, z) vary in some region D of the xz -plane. In the vector form, we may write $\vec{r} =$

$\langle x, z, f \rangle$. This is the parametrization of the graph of f : as the point (x, z) varies in D , the dependent vector \vec{r} describes the surface of the graph. At each point P of the graph we have two velocity vectors tangent to the graph:

$$\vec{r}_x = \langle 1, 0, f_x \rangle \quad \text{and} \quad \vec{r}_y = \langle 0, 1, f_z \rangle \quad (5.6)$$

where $f_x = \frac{\partial f}{\partial x}$. These vectors are neither zero nor parallel and determine an infinitesimal parallelogram with side lengths

$$\|\vec{r}_x\|dx = \sqrt{1 + f_x^2}dx \quad \text{and} \quad \|\vec{r}_z\|dz = \sqrt{1 + f_z^2}dz \quad (5.7)$$

lying in the plane tangent to the graph at P. The flat parallelograms approximate small portions of the curved surface. The area of the parallelogram is

$$\|\vec{r}_x \times \vec{r}_z\|dxdz = \|\langle -f_x, -f_z, 1 \rangle\|dxdy = \sqrt{1 + f_x^2 + f_z^2}dxdz. \quad (5.8)$$

Note that the vector $\|\vec{r}_x \times \vec{r}_z\|$ simply tells us how the area of the infinitesimal rectangle $dx \times dz$ scales under f . adding up the little pieces (integrating over D), one can argue that the total surface area of the graph is

$$A = \int \int_D \|\vec{r}_x \times \vec{r}_z\|dxdz = \sqrt{1 + f_x^2 + f_z^2}dxdz \quad (5.9)$$

substituting equation (5.2) into (5.3.1) one can obtain:

$$S_w = \int \int_D \sqrt{1 + (\pi\delta/2a\cos\pi x\sin\pi y)^2 + (\pi\delta/2a\sin\pi x\cos\pi z)^2}dxdz = 1.093S \quad (5.10)$$

5.3.2 Near-wall dynamics

An interesting point of our study is the effect of roughness shape which brings into play both the influence of the "tip" region and the secondary rolls between roughness elements. To best of our knowledge, 3 dimensional roughness geometry in RBC has been confined to laboratory experiments. [Wei et al. \[2014\]](#) have made a systematic study of turbulent RB convection with smooth and rough plates, Five cells used in their studied. They used 3D pyramids as roughness shape and found the enhancement of heat flux. [Salort et al. \[2013\]](#) used square-studs roughness, and found that global heat transfer enhancement arises when the thickness of boundary layer matches the height of the roughness.

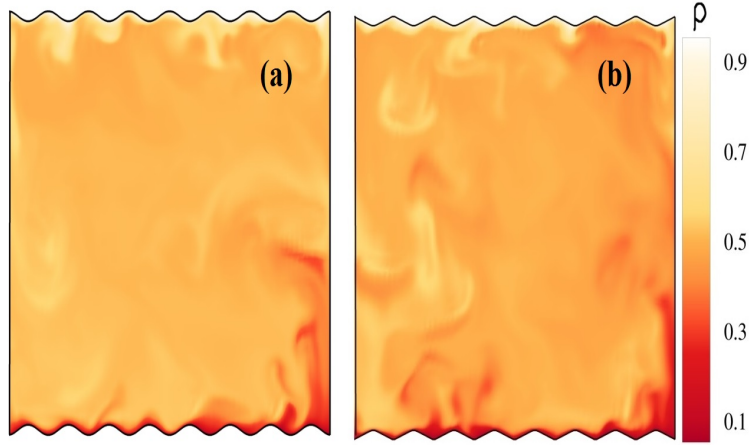


FIGURE 5.5: Instantaneous density field in a vertical section; (a) sinusoidal plate (b) pyramid plate. Gray scale denotes the the magnitude of density, $Ra = 10^8$, $Pr = 0.7$, $\Gamma = 1$.

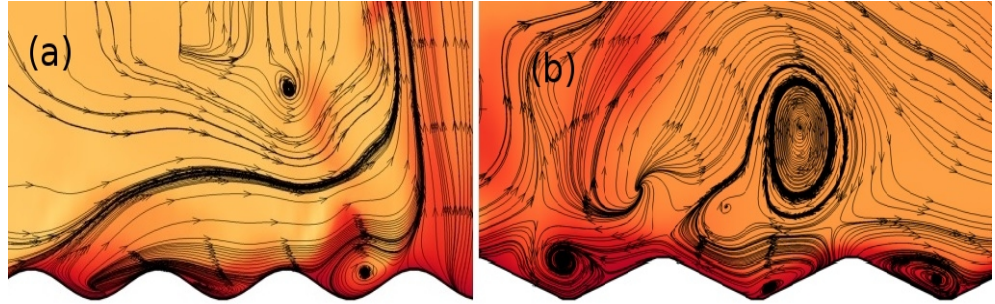


FIGURE 5.6: Close up of the flow field near the bottom rough surfaces of figure (5.5);(a) sinusoidal and (b) pyramid elements. Several stream tracers are depicted in black arrowed lines, $Ra = 10^8$, $Pr = 0.7$, $\Gamma = 1$.

Figure (5.5) and (5.6) showing typical plume emissions and its close-up from the tip of roughness elements. The detached thermal plume from the boundary layer is sheared to the down stream by the mean flow. Du and Tong [2000] observed that the emission dynamics of the thermal plumes in the smooth cell is totally different from that in the rough cell. In the smooth cell, the thermal plume erupts by its own buoyancy force, which accelerates the fluid in the central stem of the plume. The sudden acceleration of the fluid produces a vortex ring around the stem, which gives the characteristic mushroom shape of the thermal plume. Our visualization also agree with this study.

Figure (5.7) shows the local distribution of absolute wall shear stress on bottom surface for both cases in which pyramids has sharper tips with respect to the sinusoidal shape which is smooth:

$$\tau_w = \sqrt{\langle \frac{\partial u}{\partial y} \rangle_t^2 + \langle \frac{\partial w}{\partial y} \rangle_t^2}. \quad (5.11)$$

The time average of local shear stress has its maximum magnitude along the LSC

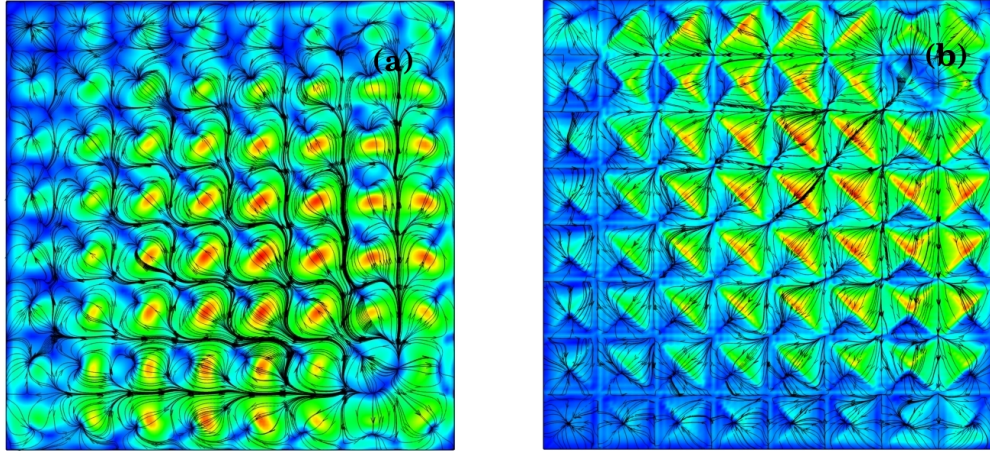


FIGURE 5.7: Absolute (colour) τ_w and contributions of velocity movement (streamlines) of the time averaged wall shear stress on the bottom plate; (a) sinusoidal and (b) pyramid geometries at $Ra = 10^8$, $Pr = 0.7$, $\Gamma = 1$

direction. The maximum magnitude of wall shear in that direction is located at the top of the roughness element for both pyramids and sinusoidal elements. One also sees from figure (5.7) the plumes released from the roughness elements are dragged horizontally before the mean wind is bent to follow the side wall. There are slight differences in the distribution of sheer stress between the two types of roughness.

5.3.3 Local density fluctuations

In figure (5.8), we plot the time averaged rms density fluctuations σ_ρ computed along LSC footprint on the diagonal plane and orthogonal to it, normalized by $\Delta\rho$.

As we have seen previously the maximum value of density fluctuations in the smooth cell, is at its mid height which mix hot and cold plume at their mid height convergence (see 4.4). In contrast in the roughness cell, as argued already, the wall density gradient is the most intense at the tips while it attains the minimum value in the throats. Overall from the flow visualization we observed that thermal plumes preferentially emitted near the tip of the rough elements are sheared horizontally in the downstream direction by the mean flow and some of them are even mixed into the roughness region by secondary eddies trapped between the roughness gaps. As a result, more thermal plumes are found in the horizontal plane with a vertical height comparable to the tip height δ , and a fewer plumes are detached in the horizontal plane far above the tip.

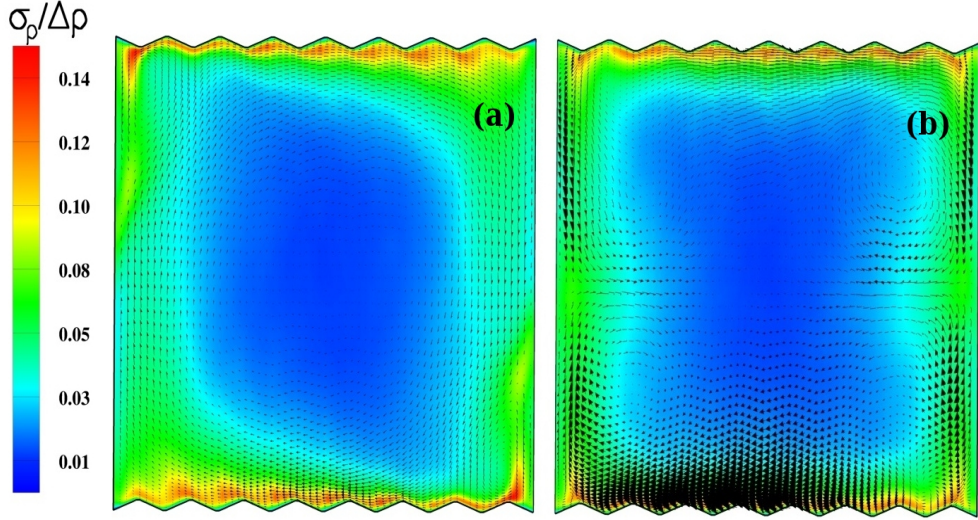


FIGURE 5.8: Time averaged (colour) values of the rms density fluctuations $\sigma_\rho/\Delta\rho$ of pyramid roughness geometry in the plane of (a)The LSC and (b) orthogonal to it. We have included 3D velocity vectors for clarity, $Ra = 10^8$, $Pr = 0.7$, $\Gamma = 1$.

5.3.4 Coherent structures near the wall

In the previous chapters, the dynamics of the “coherent structures” has been considered. An open problem remains in the identification of these structures that is not always unique. In fact, a first step towards a better understanding of the physics of turbulent motions should pass by an unambiguous way to identify the flow structures.

As far as thermal plumes are concerned the solution is quite simple, since they can be easily identified using the iso-contours of temperature or vertical velocity component.

For the identification of the vortices the matter is more complex and is still under discussion. The method used in this work is the one introduced by Chong et al. [1990], based on the signs of the eigenvalues of the velocity gradient. In this approach vortices are defined as regions where the rotation prevails over the local strain, allowing for a spiralling motion of the particles. The existence of a vortical structure is related to the local kinematic field. Hence, in order to characterize the relative motion in a given part of the field, the velocity gradient tensor is studied. In fact the equation for the relative motion vector ($r = x - x_0$) is the following:

$$\frac{dr_i}{dt} = \frac{\partial u_i}{\partial x_j} r_j = A_{ij} r_j. \quad (5.12)$$

At each point a linearised problem can be considered and hence the trajectory of the relative motion is determined by the eigenvalues λ_1, λ_2 and λ_3 of the velocity gradient which are the solution of the characteristic equation:

$$\lambda^3 + P\lambda^2 + Q\lambda + R = 0. \quad (5.13)$$

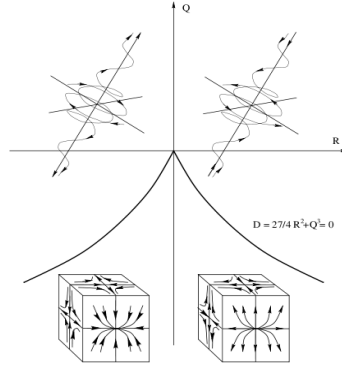


FIGURE 5.9: Perspective sketch of the cell and close up of pyramid element

The coefficients of this polynomial equation are the invariants of the velocity gradient which are equal to

$$P = -A_{ii} \quad Q = -\frac{1}{2}A_{ij}A_{ji} \quad R = -\frac{1}{3}A_{ij}A_{jk}A_{ki} \quad (5.14)$$

where the first invariant P is identically equal to zero for incompressible flows. It can be shown that the nature of the roots is determined by the sign of the discriminant:

$$D = \frac{27}{4}R^2 + Q^3 \quad (5.15)$$

If the discriminant is positive the tensor A_{ij} admits two complex conjugate eigenvalues and a real one, whereas if $D < 0$ there are three real eigenvalues. This means that since there is spiralling motion when there are complex conjugate eigenvalues the condition for the existence of vortices is $D > 0$. Because of incompressibility the sum of the three eigenvalues must be equal to zero, hence there is at least an eigenvalue of each sign. The division between positive and negative is determined by the sign of $R = -\lambda_1\lambda_2\lambda_3$, so if $R > 0$ there is one direction of contraction and two of expansion, if $R < 0$ there is one direction of expansion and summary of the possible situations is shown in figure (5.9). The second invariant can be split in two terms:

$$Q = \frac{1}{2}(\Omega_{ij}\Omega_{ij} - S_{ij}S_{ij}) \quad (5.16)$$

this expression underlines the fact that the local flow pattern depends on the balancing between vorticity and strain. Hence regions where the vorticity prevails on the strain component of the velocity gradient, positive values of Q , correspond to positive values of the discriminant. Zones characterized by a high vorticity present spiralling motion. In this view, we will identify as vortices regions of the turbulent boundary layer where the discriminant is positive. An important feature of this method is that both Q and R ,

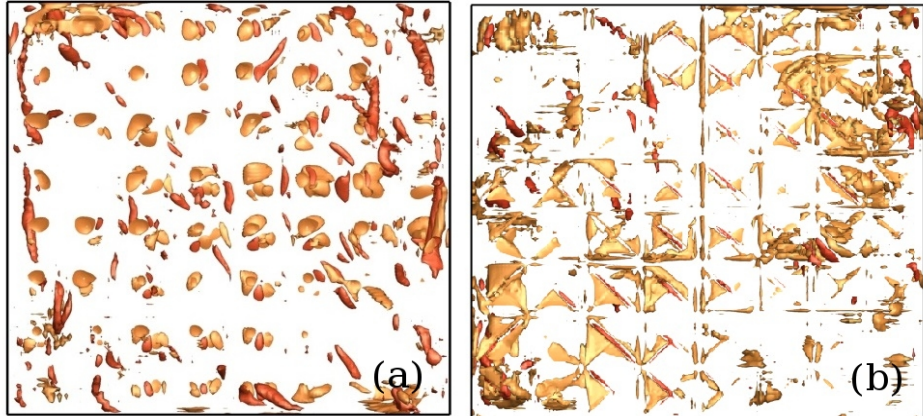


FIGURE 5.10: Visualization of turbulent structure in the bottom plane of, iso-surface of Q ; (a) sinusoidal and (b) pyramid geometries $Ra = 10^8$, $Pr = 0.7$, $\Gamma = 1$.

and consequently the discriminant, are invariant under non-uniform translations and are independent of the orientation of the coordinate transformation. Figure (5.9) shows the visualization of the instantaneous turbulent structures on bottom walls of sinusoidal and pyramid roughness. The turbulent structures confined in the region close to the thermal boundary with relatively little structure toward the centerline.

Chapter 6

Concluding remarks

A numerical study of turbulent Rayleigh-Bénard convection is the main purpose of this thesis. We have mainly studied convection with cubic confinement, although we also used periodic boundary conditions in order to validate our code with previous DNS studies. For the case where cubic geometry with adiabatic side-walls was used, we investigated the use of both smooth and rough heated walls. Our results for heat transfer for smooth heated walls are in agreement with DNS over the same range of Ra .

The code specifically performs Large Eddy Simulations (LES) in order to decrease time of computation in contrast with DNS. The main result was shown in chapter 4 and was a study of convection in a cubic box with adiabatic smooth side walls. Our numerical experiment was able to repeat the laboratory experiment of Daya and Ecke (2001) in which a significantly different statistical scaling was observed for rms fluctuations of temperature (density) and velocity at the cell center between cells having circular or square cross-sectional shape. We have confirmed that result which we note had appeared in Physical Review Letters over a decade ago and has, to the best of our knowledge, never been repeated, despite its surprising and unexplained observations. We have extended that experiment to both higher and lower Ra and have been able to map out the spatial distribution of rms fluctuations. That has revealed fixed inhomogeneities with respect to cylindrical cells that may help to explain the first-order differences in scaling between the two geometries.

In that study, we also observed, as have others, that the self organisation of the flow known as LSC has a diagonal direction in cubic confinement. We observed that with increasing Rayleigh number the shape of LSC changes to a more square form, as was inferred from measurements by [Niemela and Sreenivasan \[2003\]](#). Furthermore we have observed and quantified the strong counter rotating cells in the diagonal opposite that of the LSC. These are the cells which lead to a maximum of the density fluctuation at

the cell mid-plane and could help explain the different scaling at the cell center. We note that these flow features, having been observed in both experiment and in DNS, also provide additional validation of the LES code that we are using.

We also have observed preliminarily switching of the LSC from one diagonal to the other. This is a new result that has not to our knowledge yet appeared in the scientific literature.

We have also made a preliminary study of turbulent convection in the presence of rough surfaces. This is really at the starting phase and presents an attempt to model 3-dimensional roughness elements. This required re-thinking how to apply the grid mesh and we now have established that. Our aim is to compare initially two different shapes, one a pyramid with sharp discontinuities at the tip and between elements and the other a sinusoidally generated shape which does not have sharp edges.

All work presented here is on-going. For the case of cubic enclosures with smooth walls, we are presently pushing Ra to higher values. With our LES code validated this may prove more cost-effective than going with DNS. The reason we need to increase Ra is that the scaling of rms fluctuations presumably must be tied to the LSC and at high enough Ra we may see a diminution of its strength. Therefore we might expect to see the rms fluctuation scaling approach that of cylindrical cells at the same Ra . In the case of rough surfaces clearly we need a range of Ra in order to assess also the impact on heat transfer scaling.

Finally, it should be noted that the LES code used for this study had never been validated against other results for thermal convection and that also was one of the major achievements of this thesis.

Bibliography

- G. Ahlers, S. Grossmann, and D. Lohse. Heat transfer and large scale dynamics in turbulent rayleigh-bénard convection. *Reviews of Modern Physics*, 81:503, 2009.
- G. Amati, K. Koal, F. Massaioli, K. R. Sreenivasan, and R. Verzicco. Turbulent thermal convection at high rayleigh numbers for a boussinesq fluid of constant prandtl number. *Phys. Fluids*, 17:121701, 2005.
- M. R. Amin. The effect of the adiabatic wall roughness elements on natural convection heat transfer in vertical enclosures. *Intl J. Heat Mass Transfer*, 34:2691, 1991.
- M. R. Amin. Natural convection heat transfer and fluid flow in an enclosure convection heat transfers. *Intl J. Heat Mass Transfer*, 36 (10):2707, 1993.
- R. Anderson and C. Meneveau. Effects of the similarity model in finite difference les of isotropic turbulence using a lagrangian dynamic mixed model. *Flow Turbul*, 62(3):201, 1999.
- V. Armenio and U. Piomelli. A lagrangian mixed subgrid-scale model in generalized coordinates. *Flow Turbulence Combust*, 65:51, 2000.
- V. Armenio and S. Sarkar. An investigation of stably stratified turbulent channel flow using large eddy simulation. *J. Fluid. Mech*, 459:1, 2002.
- R. Benzi, R. Tripiccione, F. Massaioli, S. Succi, and S. Ciliberto. Scaling behaviour of the velocity and temperature correction-functions in 3d convection turbulence. *Europhys. Lett*, 25:341, 1994.
- R. Benzi, F. Toschi, and R. Tripiccione. On the heat transfer in rayleigh-bénard convection. *Journal of statistical physics*, 93(3-4):901, 1998.
- M. Breuer and U. Hansen. Turbulent convection in the zero reynolds number limit. *EPL*, 86:24004, 2009.
- E. Brown and G. Ahlers. A dynamical model of the large scale circulation in turbulent rayleigh-bénard convection: azimuthal asymmetries. *Phys. Fluids*, 20:105105, 2008.

- D. Carati, S. Ghosal, and P. Moin. On the representation of backscatter in dynamic localization models. *Phys. Fluids*, 7:606, 1995.
- B. Castaing, G. Gunaratne, L. P. Kadanoff, A. Libchaber, and F. Heslot. Scaling of hard thermal turbulence in rayleigh-bénard convection. *J. Fluid. Mech*, 204(1):1, 1989.
- F. Chillà and J. Schumacher. New perspectives in turbulent rayleigh-bénard convection. *Eur. Phys. J. E*, page 1, 2012.
- E. S. Ching, H. Guo, X. D. Shang, P. Tong, and K. Q. Xia. Extraction of plumes in turbulent thermal convection. *Phys. Rev. Lett*, 93:124501, 2004.
- M. S. Chong, A. E. Perry, and B. J. Cantwell. A general classification of three dimensional flow fields. *Physics of fluid*, 2:408, 1990.
- S. Ciliberto and C. Laroche. Random roughness of boundary increases the turbulent scaling exponent. *Phys. Rev. Lett*, 82:3998, 1999.
- Z. A. Daya and R. E. Ecke. Does turbulent convection feel the shape of the container? *Phys. Rev. Letters*, 87:184501, 2001.
- B. Y. Du and P. Tong. Turbulent thermal convection in a cell with ordered rough boundaries. *J. Fluid. Mech*, 407:57, 2000.
- A. Ebert, C. Resagk, and A. Thess. Experimental study of temperature distribution and local heat flux for turbulent rayleigh-bénard convection of air in a long rectangular enclosure. *International Journal of Heat and Mass Transfer*, 51(17):4238, 2008.
- N. Foroozani, J. J. Niemela, V. Armenio, and K. R. Sreenivasan. Influence of container shape on scaling of turbulent fluctuations in convection. *Phy. Rev. E*, 90:063003, 2014.
- M. Germano, U. Piomelli, P. Moin, and w. H. Cabot. A dynamic subgrid scale eddy viscosity model. *Phys. Fluids*, A 3:1760, 1991.
- H. Gräber. Heat transfer in smooth tuber between parallel plates, in annuli and tube bundles with exponential heat flux distributions in forced laminar or turbulent flow. *J. Heat Mass transfer*, 13:1645, 1970.
- D. Gray and A. Giorgini. xperiments on the onset of longitudinal vortices in horizontal blasius flow heated from below. *Joural of Heat transfer*, 100:71, 1976.
- S. Grossmann and D. Lohse. Scaling in thermal convection: a unifying theory. *J. Fluid. Mech*, 407:27, 2000.
- S. Grossmann and D. Lohse. Prandtl and rayleigh number dependence of the reynolds number in turbulent thermal convection. *Phys. Rev. E*, 66:016305, 2002.

- S. Grossmann and D. Lohse. On geometry effects in rayleigh-bénard convection. *J. Fluid. Mech.*, 486:105, 2003.
- S. Grossmann and D. Lohse. Fluctuations in turbulent rayleigh-bénard convection: The role of the plumes. *Physics of Fluids*, 16:4462, 2004.
- G. Grötzbach. Spatial resolution for direct numerical simulation of rayleigh-bénard convection. *J. Comput. Phys.*, 49:241, 1983.
- S. D. Huang, M. Kaczorowski, R. Ni, and K. Q. Xia. Confinement-influenced heat transport enhancement in turbulent thermal convection. *Phy. Rev. Lett.*, 111:104501, 2013.
- J. Jiménez. Turbulent flow over rough walls. *Annu. Rev. Fluid Mech.*, 36:137, 2004.
- M. Kaczorowski and K. Q. Xia. Turbulent flow in the bulk of rayleigh-bénard convection: small scale properties in a cubic cell. *J. Fluid. Mech.*, 722:569, 2013.
- W. M. Kays. Turbulent prandtl number - where are we? *J. heat transfer*, 116:284, 1994.
- S. Kenjeres and K. Hanjalic. Numerical insight into flow structure in ultraturbulent convection. *Phys. Rev. E*, 66:036307, 2002.
- R. Kerr. Rayleigh number scaling in numerical convection. *J. Fluid. Mech.*, 310:139, 1996.
- R. Kerr and J. R. Herring. Prandtl number dependence of nusselt number in direct numerical simulation. *J. Fluid. Mech.*, 419:325, 2000.
- S. J. Kimmel and Domaradzki. Large eddy simulations of rayleigh-bénard convection using subgrid scale estimation model. *Phys. Fluids*, 12:169, 2000.
- R. H. Kraichnan. Turbulent thermal convection at arbitrary pr number. *Phys. Fluids*, 5:1374, 1962.
- R. Krishnamurti and L. N. Howard. Large scale flow generation in turbulent convection. *Proc. Natl Acad Sci. USA*, 78:1981, 1981.
- P. K. Kundu and I. M. Cohen. Fluid mechanics. *Academic press, London*, second edition, 2002.
- J. P. R. Kunnen, H. J. H. Clercx, B. J. Geurts, L. A. Bokhoven, R. A. D. Akkermans, and R. Verzicco. A numerical and experimental investigation of structure function scaling in turbulent rayleigh-bénard convection. *Phys. Rev. E*, 77:016302, 2008.

- R. Kunnen, B. J. Geurts, and H. J. H. Clercx. Turbulence statistics and energy budget in rotating rayleigh-bénard convection. *European Journal of Mechanics B/fluids*, 28: 578, 2009.
- R. Lakkaraju, M. Stevens, R. Verzicco, S. Grossman, A. Prosperetti, C. Sun, and D. Lohse. Spatial distribution of heat flux and fluctuations in turbulent rayleigh-bénard convection. *Phys. Rev. E*, 86:056315, 2012.
- R. Lakkaraju, R. J. A. M. Stevens, R. Verzicco, S. Grossmann, A. Prosperetti, C. Sun, and D. Lohse. Spatial distribution of heat flux fluctuations in turbulent rayleigh-bénard convection. *Physical Review E*, 86:056315, 2012.
- L. D. Landau and E. M. Lifshitz. Fluid mechanics. *Oxford: Pergamon*, 1959.
- D. K. Lilly. A proposed modification of the germano subgrid scale closure method. *Phys. Fluids*, A4:633, 1992.
- C. Meneveau, T. S. Lund, and W. H. Cabot. A lagrangian dynamic subgrid-scale model of turbulence. *J. Fluid. Mech*, 319:353, 1996.
- P. K. Mishra, A. K. De, M. K. Verma, and V. Eswaran. Dynamics of reorientations and reversals of large-scale flow in rayleigh-bénard convection. *J. Fluid. Mech*, 668:480, 2011.
- A. S. Monin and A. M. Yaglom. Statistical fluid mechanics. *Cambridge, Ma:MIT*, 1975.
- J. J. Niemela and K. R. Sreenivasan. Thermal fluctuations and their ordering in turbulent convection. *Physica A*, 315:203, 2002.
- J. J. Niemela and K. R. Sreenivasan. Rayleigh number evolution of large scale coherent motion in turbulent convection. *Europhys Lett*, 62:829, 2003.
- J. J. Niemela, L. Skrbek, K. R. Sreenivasan, and R. J. Donnelly. Turbulent convection at very high rayleigh numbers. *Nature*, 404:837, 2000.
- J. J. Niemela, L. Skrbek, K. R. Sreenivasan, and R. J. Donnelly. The wind in confined thermal convection. *J. Fluid. Mech*, 449:169, 2001.
- A. Petronio, F. Roman, C. Nasello, and V. Armenio. Large eddy simulation model for wind driven sea circulation in coastal areas. *Processes Geophys.*, 20:1095, 2013.
- B. A. Putheveettil and J. H. Arakeri. Plume structure in high-rayleigh-number convection. *J. Fluid. Mech*, 526:217, 2005.
- X. L. Qiu and K. Xia. Viscous boundary layer at the side wall of convection cell. *Phys. Rev. E*, 58:1998, 1998.

- X. L. Qiu, X. L. Shang, P. Tong, and K. Q. Xia. Origin of the temperature oscillation in turbulent thermal convection. *Phys. Fluids*, 16:412, 2004.
- X. L. Qiu, K. Q. Xia, and P. Tong. Experimental study of velocity boundary layer near a rough conducting surface in turbulent natural convection. *J. Turbul.*, 30:1, 2005.
- M. Reeuwijk, H. J. J. Jonker, and K. Hanjalić. Wind and boundary layers in rayleigh-bénard convection. i. analysis and modeling. *Phys. Rev. E*, 77:036311, 2008.
- A. J. Reynolds. The prediction of turbulent prandtl and schmidt numbers. *J. Heat Mass transfer*, 18:1055, 1975.
- P. E. Roche, B. Chabaud, and B. Hebral. Observation of the 1/2 power law in rayleigh-bénard convection. *Phys. Rev. E*, 63:045303, 2001.
- F. Roman, V. Armenio, and J. Fröhlich. A simple wall layer model for large eddy simulation with immersed boundary method. *Physics of Fluids*, 21(10):101701, 2009.
- F. Roman, G. Stipcich, V. Armenio, R. Inghilesi, and S. Corsini. Large eddy simulation of mixing in coastal areas. *International Journal of Heat and Fluid Flow*, 31(3):327, 2010.
- P. Sagaut. Large-eddy simulation for incompressible flows - an introduction first edition. *Springer-verlag*, 2001.
- J. Salort, O. Liot, E. Rusaouen, F. Seychelles, J.-C. Tisserand, M. Creyssels, B. Casting, and F. Chillà. Thermal boundary layer near roughness in turbulent rayleigh-bénard convection: flow structure and multi-stability. *PAC*, page 1, 2013.
- X. D. Shang, X. L. Qiu, P. Tong, and K. Q. Xia. Measured local heat transport in turbulent rayleigh-bénard convection. *Phys. Rev. Lett*, 90:074501, 2003.
- X. D. Shang, P. Tong, and K. Q. Xia. Scaling of the local convective heat flux in turbulent rayleigh-bénard convection. *Phys. Rev. Lett*, 100:244503, 2008.
- Y. Shen, K. Q. Xia, and P. Tong. Turbulent convection over rough surfaces. *Phys. Rev. Lett*, 76:908, 1996.
- O. Shishkina and C. Wagner. Local heat fluxes in turbulent rayleigh-bénard convection. *Phys. Fluids*, 19:085107, 2007.
- O. Shishkina and C. Wagner. Analysis of sheetlike themal plumes in turbulent rayleigh-bénard convection. *J. Fluid. Mech*, 599:383, 2008.
- O. Shishkina and C. Wagner. Modelling of the influence of wall roughness on heat transfer in thermal convection. *J. Fluid. Mech*, 686:568, 2011.

- O. Shishkina, R. Stevens, S. Grossmann, and D. Lohse. Boundary layer structure in turbulent thermal convection and its consequences for the required numerical resolution. *New Journal of Physics*, 12:075022, 2010.
- J. Smagorinsky. General circulation experiments with the primitive equations. i. the basic experiment. *Mon. Weath. Rev.*, 91:99, 1963.
- K. R. Sreenivasan, A. Bershadskii, and J. J. Niemela. Mean wind and its reversal in thermal convection. *Phys. Rev. E*, 65:056306, 2002.
- R. J. A. M. Stevens, R. Verzicco, and D. Lohse. Radial boundary layer structure and nusselt number in rayleigh-bénard convection. *J. Fluid. Mech.*, 643:495, 2010.
- R. Stoll and F. Porte-Agel. Dynamic subgrid-scale models for momentum and scalar fluxes in large-eddy simulations of neutrally stratified atmospheric boundary layers over heterogeneous terrain. *Water Resource. Res.*, 42:W01409, 2006.
- G. Stringano and R. Verzicco. Mean flow structure in thermal convection in a cylindrical cell of aspect-ratio one half. *J. Fluid. Mech.*, 458:1, 2006.
- G. Stringano, G. Pascazio, and R. Verzicco. Turbulent thermal convection over grooved plates. *J. Fluid. Mech.*, 557:307, 2006.
- K. Sugiyama, R. Ni, J. Stevens, T. Chan, S. Zhou, H. Xi, C. Sun, S. Grossmann, K. Xia, and D. Lohse. Flow reversals in thermally driven turbulence. *Phys. Rev. E*, 105:034503, 2010.
- C. Sun and K. Q. Xia. Three dimensional flow structures and dynamic of turbulent convection in a cylindrical cell. *Phys. Rev. E*, 72:026302, 2005.
- C. Sun, Y. H. Cheung, and K. Q. Xia. Experimental studies of the viscous boundary laye properties in turbulent rayleigh-bénard convection. *J. Fluid. Mech.*, 605:79, 2008.
- H. Tennekes and J. L. Lumley. A First Course in Turbulence. (MIT Press), 1970.
- R. Verzicco and R. Camussi. Prandtl number effects in convective turbulence. *J. Fluid. Mech.*, 383:55, 1999.
- R. Verzicco and R. Camussi. Numerical experiments on strongly turbulent thermal convection in a slender cylindrical cell. *J. Fluid. Mech.*, 477:19, 2003.
- R. Verzicco and K. R. Sreenivasan. A comparison of turbulent thermal convection between conditions of constant temperature and constant heat flux. *J. Fluid. Mech.*, 595:203, 2008.

- M. Vinokur. On one dimensional stretching functions for finite-difference calculations. *University of Santa Clara, NASA Contractor Report 3313*, 1980.
- S. Wagner, O. Shishkina, and C. Wagner. Boundary layers and wind in cylindrical rayleigh-bénard cells. *J. Fluid. Mech.*, 697:336, 2012.
- S. Wagner, O. Shishkina, and C. Wagner. Influence of geometry on rayleigh-bénard convection. *New Results in Numerical and Experimental Fluid Mechanics IX*, 124:313, 2014.
- P. Wei, T. S. Chan, R. Ni, X. Z. Zhao, and K. Q. Xia. Heat transport properties of plates with smooth and rough surfaces in turbulent thermal convection. *J. Fluid. Mech.*, 740:28, 2014.
- K. Q. Xia, C. Sun, and S. Q. Zhou. Particle image velocimetry measurement of the velocity field in turbulent thermal convection. *Phys. Rev. E*, 68:066303, 2003.
- J. Zang, R. L. Street, and J. R. Koseff. A non-staggered grid, fractional step method for time dependent incompressible navier stokes equations in curvilinear coordinates. *Journal of Computational Physics*, 114:18, 1994.
- Q. Zhou and K. Q. Xia. Physical and geometrical properties of thermal plumes in turbulent rayleigh-bénard convection. *New Journal of Physics*, 12:075006, 2010.
- Q. Zhou, C. Sun, and K. Q. Xia. Morphological evolution of thermal plumes in turbulent rayleigh-bénard convection. *Phys. Rev. Lett.*, 98:074501, 2007.
- G. Zocchi, E. Moses, and A. Libchaber. Coherent structures in turbulent convection, an experimental study. *Physica A*, 166:387, 1990.